Grant agreement no. 312818
SPA.2012.2.2-01 : Key technologies enabling observations in and from space

- Collaborative project -

WP 2 – Interferometer Satellite Technology Development

D2.7

Final Report on Telescope and Satellite Readness for FIR Interferometer

Due date of deliverable: month 36
Actual submission date:
Start date of project: January 1st 2013   Duration: 36 months

Lead beneficiary for this deliverable: AGI srl
Last editor: V. A. Iafolla, Assist in Gravitation and Instrumentation (AGI srl)

Contributors:
V. Iafolla (AGI), W. Holland (STFC), E. Pascale (Cardif), G. Savini (UCL), S. Vives (CNRS-LAM), D. Walker (UCL/Glyndwr), M. Jones (Glyndwr)

HISTORY TABLE

Version	Date	Released by	Comments
Draft00	27/07/15	VI	Original skeleton
Draft01	17/11/15	VI	First Issue
01	14/01/16	VI	Final Version

TABLE OF CONTENTS

APPLICABLE DOCUMENTS

D1.1) Science requirements.
D1.2) Instrument performance requirements preliminary document.
D1.3) Satellite position requirements and preliminary stability assessment
D2.1) Candidate key technologies trade-off study.
D2.2) Technical report on tolerances and implications in the use of carbon composites for light-weight deployable telescope.
D2.3) Accelerometer prototype for spacecraft control loop.
D2.4) Prototype of cryogenic-tested polished CFC mirror.
D2.5) Nano-satellite technology validation test-bench.
D2.6) Test bench validation report and technology analysis.

ACKNOWLEDGEMENTS

DISCLAIMER

The content of this deliverable does not reflect the official opinion of the European Union. Responsibility for the information and views expressed in the deliverable therein lies entirely with the author(s).

ACRONYMOUS

AOCS Attitude and Orbit Control System
APE Actual Pointing Error
Arcmin Arc minute. 1 arcmin = 1/60 degrees
Arcsec Arc second. 1 arcsecond = 1/60 arcmin = 1/3600 degrees
BC Beam Combiner
CoM Centere of mass
DoF Degree of Freedom
FD/FDS Flight Dynamics/Flight Dynamics System
FFT Fast Fourrier Transforms
FIR Far Infra-Red
FIRI Far InfraRed Interferometer
FSU Fringe Sensor Unit
FTS Fourier Transform Spectrometer
G/S Ground Station
H/W Hardware
HGA High Gain Antenna
HK HouseKeeping data
IFOV Interferometric Field Of View
ILS Instrument Line Shape
IR Infrared
ISL Inter-satellite link
ISO Infrared Space Observatory
ITD Inter-Telescope Distance
L2 Second Lagrangian Equilibrium Point (Sun-Earth System)

MGA Medium Gain Antenna
MM Mass Memory
NEP Noise Equivalent Power
NER Noise Equivalent Radiance
OBC On-Board Computer
OBT On-Board Time
ODL Optical Delay Line
OPD Optical Path Difference
PLM Payload Module
RMS Root Mean Square
RW Reaction wheel
S/C Spacecraft
S/W Software
SA Solar Array
SADM Solar Array Drive Mechanism
SNR Signal to Noise Ratio
SRP Solar radiation pressure
SSEA Sun-Spacecraft-Earth Angle
TBC To Be Confirmed
TBD To Be Defined
TC Telecommand
TM Telemetry
WFE Wave Front Error

1 INTRODUCTION

This document represents the deliverable DEL_2.7 "Final Report on telescope and satellite technology readiness for FIR interferometer" due at end of the FISICA study. In particular it makes a critical review and a synthesis of the studies and experimental activities concerning the Work Package 2, as described in the FISICA DOW. The tasks of this WP was connected to an overall technology development study of the key satellite and telescope aspects relevant to a Far-Infrared Interferometer and investigated the following particular aspects, retained as critical:

- Light-weight cryogenic materials and their employment through deployable systems.
- Investigation of the technical challenges in implementing closed loop accelerometer feedback for satellite position control to satisfy positional accuracy requirements.
- Identify and validate a key metrology technique for FIRI using a nano-satellite test bench

The reports on the results of the studies before described, which list is here after indicated, has been taken as deliverables of the FISICA study and used as the base to write the present 'Final Report'

D2.1) Candidate key technologies trade-off study. This study assessed the available technologies employed in accurate relative positioning of two or more satellites. [month 13]

D2.2) Technical report on tolerances and implications in the use of carbon composites for light-weight deployable telescope. Report describing the current state-of-the-art of CFC mirrors and the current knowledge of thermal implications of their usage at cryogenic temperatures for light-weight deployable mirrors. [month 25]

D2.3) Accelerometer prototype for spacecraft control loop. Has been studied and implemented an high sensitive accelerometer to be used in a control loop of the satellite dynamic; the study has been closely linked to the satellites environmental conditions, particularly to the dynamical noise, both in the band, in which the satellite must be controlled, and out of this (for avoid its saturation and aliasing effects). [month 25]

D2.4) Prototype of cryogenic-tested polished CFC mirror. A prototype of a polished CFC mirror subject to cryogenic testing to verify current polishing performances of these materials as light weight mirrors and the implications of thermal cycling. [month 36]

D2.5) Nano-satellite technology validation test-bench. A nano-satellite test-bench has been developed to house and test one or more of the FIRI technologies. The test bench allowed defining the concept and development of ground support equipment. [month 36]

D2.6) Test bench validation report and technology analysis. This report contains the tests result performed with the test bench validating and expected performance of a given technology (the accelerometers) with actual data. [month 36]

D2.7) Final Report on telescope and satellite technology readiness for FIR interferometer. Final report on the WP2 activities detailing the current state-of-the-art and progress achieved in the satelllite-related technology (light-weight mirrors, position control) readiness for employment in a far-infrared space interferometer [month 36]

The conclusions of these studies are reported at the end of every specific section.

2 STUDY WORK DESCRIPTION

Ihis documents are reported the synthesis of the tasks connected to the work performed in the framework of the WP_2.

Task 2.0 "Scientific Coordination of the Interferometer Satellite Technology Development".
This task has been devoted to the scientific coordination of the activities of the WP-2; Valerio Iafolla of AGI srl was the coordinator.

Task 2.1 "Low-mass cryogenic deployable telescope mirror study".
This task has been performed by Glyndwr University under the coordination of Prof. David Walker (whose position is 50-50 joint UCL/Glyndwr). The work has been conducted under the collaboration between UCL, the Glyndwr Composites Centre, and the National Facility for Ultra Precision Surfaces. Establishment of this has been led by UCL under RCUK Basic Technology funding. The used Facility is hosted by Optic Technium which (itself now operated by Glyndwr) is located in the N. Wales Opto-Electronics Cluster.

The tasks make use of expertise in large and small optics fabrication, opto/mechanical design, and advanced mirror substrates. Particular important has been the expertise of the Glyndwr Composites Centre, who worked particular closely with the N. Wales Airbus factory. The Task also draws on a parallel (recently approved) project to develop a light-weight CFC optical imaging system for military use.

The work in manufacturing and polishing, and research in light-weight carbon materials, has explored the suitability of classical and non-tube carbon fibre composites for performance, environmental conditions, reliability and risk. Alternative materials are also be explored. Additional studies have been performed through the analysis of the expected cryogenic performance of deployment, actuation and bearing technologies.

Task 2.2 "Satellite positioning tolerancing based on accelerometer control loop"
This task lead by Dr. Iafolla (also coordinating the WP) examined the technical challenges in implementing closed loop accelerometer feedback for satellite position control to satisfy positional accuracy requirements.

The activities have been performed in close connection with the one concerning the task 2.3 (after described). Metrology and position accuracy measurements required close interaction between the two tasks and effects such as vibration noise affecting the observation was kept in account.

During this task, the requirements on the accelerometer accuracy when detecting non gravitational perturbations has been assessed and appropriate algorithms using the accelerometers to regulate thrusters has been developed. The exit of the study allowed implementing a prototype of accelerator with the appropriate requirements for a FIR mission. The implemented accelerometer demonstrated to have the appropriate sensitivity, frequency band and thermal stability. Experimental tests on the accelerometer has been performed and documented. Person/months required: 13 (AGI)

Task 2.3 "Validation of key technologies with nano-satellite"
Coordinator of this task has been Dr. Sebastien Vives (at the Laboratoire d'Astrophysique de Marseille, France). Space-born testing of key technologies, offered by a nano-satellite mission, is an important ingredient to improve the FIRI Technology Readiness Level (TRL). In this task, the possibilities for technological validation offered by a nano-satellite-born test bench will be considered and a selection of FIRI key technologies benefiting from such

validation has been identified. The technology validation test-bench and its associated support equipment has been developed (optics, mechanics and electronics). In parallel, the nano-satellite concept has been studied and implemented. Person/months required: 43 (CNRS-LAM)

2.1 STUDY CONTEXT – DRIVERS AND REQUIREMENTS

To continue in the way started with Herschel Space Observatory in the astrophysics study in the far-IR region $(30 - 300\mu m)$ it is necessary to conceive observation with more angular resolution, so to obtain informations about the could Universe (earliest stages in the formation of galaxies, stars and planets). The FIRI concept is based on the prosteptive to perform astrophysical observation in space so to avoiding the Earth atmosphere opacity, so to providing informations at sub-arcsecond scales in the far-IR.

Here after are reported the main results connected to the DEL_1.1 and DEL_1.2, representing the start points for the present study.

List of the main primary scince.
 a) Operate in the far-infrared region of the spectrum, addressing a number of key scientific objectives, hitherto unanswered;
 b) Will have the sensitivity and resolving power to measure a number of key ionic, atomic and molecular lines over a range of astrophysical phenomena;
 c) Has sufficient angular resolution to be able to probe the previously unexplored inner regions e.g. nuclei of galaxies and star-forming cores.

Table of the Scientific Objectives.
The following table, extract from the DEL_1.2, reports the main scientific objectives with the necessary requirements for their obtainement.

Table_2.3-1 *List of the main scientific objectives and main requirements for their obtainiment.*

Theme	Science Case	Required field-of-view (arcmin)	Required angular resolution (arcsec)	Required spectral resolution	Sensitivity required (estimated line flux)
Star formation: Protostars	Resolve 100AU: detection of the first hydrostatic cores	$0.5 - 1$	0.25" @ 400pc 0.40" @ 250pc 0.66" @ 150pc	~3000	H_2O: 2.1×10^{-20} W/m^2 H_2O: 5.4×10^{-20} H_2O: 1.5×10^{-19}
Star formation: Protoplanetary disks/Formation of planetary systems	Resolve the outer structure $(10 - 100AU)$ of protoplanetary disks	$1 - 2$	0.20" (30AU @ 140pc) 0.75" (100AU @ 140pc)	~5000	A: [OI]63μm: 2.4×10^{-16} [OI]145μm: 1.2×10^{-17} B: [OI]63μm: 3.7×10^{-16} [OI]145μm: 3.1×10^{-17}
Star formation: Binary and multiple systems	Resolve binary and multiple protostellar objects	0.5	0.25" @ 400pc	~3000	[OI]63μm: 9×10^{-19} H_2O: $8 \times 10^{-19} - 4 \times 10^{-18}$ CO: $2 \times 10^{-19} - 4 \times 10^{-18}$ HDO: 4×10^{-18}
Star formation: Massive star formation	Answer to the question if massive clumps form only one massive star or stellar clusters	$1 - 2+$	0.25" @3kpc	~3000	^{12}CO(10-9): 5×10^{-18} ^{13}CO(10-9): 8×10^{-19} C^{18}O(10-9): 1×10^{-19}
The Galactic	Map the central	$1 - 2+$	0.25" @ 8kpc	~3000	[OI]63μm: 2.4×10^{-17}

Center	thousands AU around the SgrA* Black Hole in extinction free continuum and lines				CO(14-13)@186μm: 1.9×10^{-19} CO(24-23)@108μm: 2.0×10^{-20}
AGN in the local Universe	Resolving the torus and the emission-line regions in the circumnuclear environment of local AGN	0.5 – 1	0.10" @ 50Mpc	1500 – 3000	[OIV]26μm: 1×10^{-19}, 1×10^{-18}, 3×10^{-18} (min, ave, max) [NeV]24μm: 3×10^{-20}, 2.8×10^{-19}, 9×10^{-19} [OI]63μm: 6×10^{-19}, 2.6×10^{-18}, 7.6×10^{-18}
Galaxy formation and Evolution	Resolving starburst complexes and Narrow Line Regions along galaxy evolution	1 – 2	0.10" starburst (0.02" NLR)	1500 – 3000	Line fluxes are typically in the range $10^{-21} – 10^{-19}$

List of the main Requirements assumed for the FISICA study.

In the following is reported a list of the main requirements assumed for the study and extracted from the DEL_1.2 and at which it is possible to refer to get more informations.

Table 2.3-2 *List of the main Requirements assumed for the FISICA study*

Requirement Number	Description
R2.1.1	The continuous spectral coverage for the instrument will be from 25 to 400μm.
R2.1.2	Over the spectral range there will be 4 discrete bands, each of which will be optimised with its own camera.
R2.1.3	Band 1 will be centered at 37.5μm and have low and high wavelength cut-offs at 25 and 50μm, respectively.
R2.1.4	Band 2 will be centered at 75μm and have low and high wavelength cut-offs at 50 and 100μm, respectively
R2.1.5	Band 3 will be centered at 150μm and have low and high wavelength cut-offs at 100 and 200μm, respectively.
R2.1.6	Band 4 will be centered at 300μm and have low and high wavelength cut-offs at 200 and 400μm, respectively.
R2.2.1	The minimum angular resolution achievable will be 0.1 arcsec at a wavelength of 40μm.
R2.2.2	The baseline will be variable from a few metres up to a maximum inter-telescope distance of 100m.
R2.3.1	In "spectroscopy mode" the resolving power required will be in the range 1000 – 5000.
R2.3.2	In "SED mode" the resolving power required will be around 100.
R2.3.3	For "spectrophotometry mode" a spectral resolving power of ~5 is needed
R2.4.1	The requirement for the line sensitivity is 10^{-19} W/m^2 (1σ in 1hr), with a goal of ~10^{-20} W/m^2 (1σ in 1hr, or 5σ in 24 hrs).
R2.4.2	The point-source sensitivity is required to measure flux density levels of 30μJy (1σ in 1hr, or 5σ in 24 hrs) with a goal of <10μJy (1σ in 1hr, or 5σ in 24 hrs).
R2.5.1	The field-of-view of the instrument will be 1 arcmin in diameter with a goal of 2 arcmins.
R3.1.1	The primary mirrors of the telescope will be 2m in diameter.
R3.2.1	The instrument cryostat window and cold optics will not exceed 200mm in diameter.
R3.3.1	The surface accuracy of the optical components within the telescope should be 140nm RMS or better.

R3.3.2	The instrument is to have diffraction-limited performance at the shortest wavelengths (25μm).
R3.3.2	The instrument is to have diffraction-limited performance at the shortest wavelengths (25μm).
R3.3.4	Field distortion across the detector arrays is required to be < 3%.
R3.4.1	The temperature of the mirrors in the telescope will be 4.5K or less.
R3.4.2	The emissivity of each telescope mirror will be < 3% at all wavelengths.
R3.4.3	Diffuse stray light will contribute less than 5% to the overall background power levels.
R3.4.4	A point source within the field-of-view will contribute < 2% of the light that appears as a ghost image.
R3.5.1	The absolute pointing error will have a requirement of <2 arcsec RMS and a goal of <1 arcsec.
R3.5.2	A tracking accuracy of <1 arcsec RMS will be maintained over a 24 hr period (typical observing period) with a goal of <0.5 arcsec.
R4.1.1	The cryostat window must be made of a highly transmissive material with a requirement of >90% transmission at all wavelengths.
R4.1.2	The opto-mechanical design should allow for the provision of optical baffles at the cryostat window
R4.1.3	To minimise stray light and heat loads the cryostat should have nested radiation shields, nominally at 4, 2 and 1K.
R4.1.4	The internal cryostat mirrors should be cooled to <3K, with a goal of <2K to avoid excess power loading on the arrays.
R4.1.5	The detector arrays need to operate at temperatures of < 100mK.
R4.1.6	The cryostat should be modular, with a goal of allowing access to the arrays in < 4 hrs once the instrument warm-up has been completed and the cryostat positioned for disassembly.
R4.2.1	The sampling accuracy required for the linear translation stage for the delay line is 0.1% at the shortest wavelength.
R4.2.2	The surface accuracy of the delay line and re-imaging mirrors should be 140nm RMS or better.
R4.2.3	The emissivity of the mirror surfaces within the cryostat should be < 3%.
R4.3.1	Bandpass filters have a requirement of >80% transmission and <1% out-of-band power.
R4.3.2	Provision is needed to vary the gap between the bandpass filter and the array by up to 3λ.
R4.3.3	IR blocking and low-pass filters on radiation shields will each have > 95% transmission for wavelengths longer than the cut-off.
R4.3.4	High efficiency dichroics with > 95% transmission and reflectance at an appropriate cut-off wavelength are required for each spectral band.
R4.4.1	The beam combiner will have ≥ 49% transmission and reflection over the spectral band.
R4.4.2	The beam combiner will have ≤ 1% emissivity over the spectral band.
R4.5.1	For bare arrays a cold stop will define the detector field-of-view.
R4.5.2	The optical design will determine the optimum diameter and location of the cold stop.
R4.5.3	The cold stop design must allow changeable apertures to be inserted.
R4.6.1	The choice of detector technology will be down-selected from an assessment of the available options at the time.
R4.6.2	The pixel spacing in the focal plane at all wavelengths will be $0.5F\lambda$.
R4.6.3	The pixel geometry/count for band 1 will be of order 48×48 (2304) with a goal of 96×96 (9216).
R4.6.4	The pixel geometry/count for band 2 will be of order 24×24 (576) with a goal of 48×48 (2304).
R4.6.5	The pixel geometry/count for band 3 will be of order 12×12 (144) with a goal of 24×24 (576).
R4.6.6	The pixel geometry/count for band 4 will be of order 6×6 (36) with a goal of 12×12 (144).
R4.6.7	The requirement NEP for a B1 detector is $< 7.7 \times 10^{-19}$ W/$\sqrt{Hz}$
R4.6.8	The requirement NEP for a B2 detector is $< 5.6 \times 10^{-19}$ W/$\sqrt{Hz}$.
R4.6.9	The requirement NEP for a B3 detector is $< 4.7 \times 10^{-19}$ W/$\sqrt{Hz}$.
R4.6.10	The requirement NEP for a B4 detector is $< 9.1 \times 10^{-19}$ W/$\sqrt{Hz}$.
R4.6.11	The pixel yield for each detector array will be ≥ 90%.
R4.6.12	The detector array must not have adjacent bad columns or rows, as well as no dead clusters of greater than 4×4 pixels.
R4.6.13	The optical coupling efficiency for an individual $0.5F\lambda$ detector should be maximised with a goal

	of ≥15% for all spectral channels.
R4.6.14	The absorption efficiency for an individual detector should be ≥ 80% for all spectral channels.
R4.6.15	The detector time constant needs to be of order 0.2 msec.
R4.7.1	The data acquisition system must read out each detector signal at a rate of ~ 2 kHz.
R4.7.2	The data acquisition system must have at least 16 bits to digitise the signal
R4.7.3	Non-detector noise should cause no more than a 20% increase in the detector NEP.
R4.7.4	The distant pixel crosstalk is required to be < 0.3%.
R.5.2.1	The instrument will have the provision for one of more internal calibrators to assess the performance of the optics and detector arrays.
R.5.2.2	The instrument will be capable of rapidly carrying out routine, calibration observations of flux and line standards.
R.5.2.3	The instrument will carry out periodic measurements of a bright, point-like source to enable a full characterisation of the telescope beam shape.
R.5.3.1	The field of regard for the satellite should be a 40° band centered on the Ecliptic (TBC).
R.5.4.1	The time to slew to a target over a large angle (anywhere on the sky) should be < 10 mins.
R.5.4.2	The time to slew to a target over a small angle (within a cone angle of 45 degrees) should be < 2 mins.
R.5.4.3	After a slew a settling time of 0.5 minutes will be allowed, with a goal to reduce this time as far as practical.
R.5.5.1	The optical path difference of the two beams must be known to less than 5µm.
R.5.5.1	The mission lifetime should be maximised with a minimum requirement of 5 years.

3 GENERALITY OF A FIR SPACE-BASED INTERFEROMETER

3.1 BASICAL CONCEPT OF A DOUBLE FOURIER INTERFEROMETER

In this study, as for the past proposed FIR space telescope i.e. SPECS, SPIRIT and FIRI, is considered a single instrument giving the possibility to combine spatial and spectroscopic measurements at the same time; it make use of a Michelson stellar interferometer with a scanning optical delay line for Fourier transform spectroscopy, so to perform the double Fourier modulation (DFM) permitting to obtain the spatial image of the source for all its spectral components in the required wavelength range.

In this architecture, light from the two telescopes is combined at the pupil plane and the combined signal is detected by means of detector focal plane arrays. In particular, the two telescopes can move so to operate at many interferometric baselines distance, permitting to resolve several spatial structures with the necessary angular scales, so to produce high quality far-IR images. The maximum image resolution is determined by the maximum baseline length of the interferometer. In order to obtain very high sensitivity, otherwise limited by astrophysical background photon noise, the principal optical elements of the interferometers are cooled to (or below) 4 K and high sensitive detectors (at sub-K temperatures) are used, this in respect of the requirements: R4.1.3, R4.1.4, R4.1.5, R4.1.6.

As mentioned, to obtain simultaneously both the image of an area of sky and its emission spectrum, an interferometric technique, suggested originally by Mariotti and Ridgway (1988), that combines interferometry for images, with the spectrometric interferometry by means of Fourier transforms was considered.

Two telescopes placed at a distance B between them, pointed precisely at the same area of the sky, the collected light is recombined, after entering on one of the two beams a phase temporal delay. The combination of the two beams can be sent to a single-pixel detector and the signal acquisition, made in function of the delay, is the interferogram, whose Fourier Transform gives the frequency spectrum of the sources in the area of sky observed. The amplitude of each observed frequency or corresponding wavelength, is the amplitude of the harmonic component associated with sources of wavelength λ, separated by an angle equal to

$$\alpha = \frac{\lambda}{2B}$$

for sources aligned with the baseline of the interferometer B, in that specific elementary step of measurement (point of the plane u, v).

If a detailed image is desired with this technique, it is necessary for the u-v plane to be densely sampled by making measurements with the interferometer in all possible positions obtained by changing the distance between the two telescopes both in radial position ($Bmin\ to\ Bmax$) and orienting the baseline in all angular positions. If the telescopes have a diameter of $1m$, the maximum non-redundant uv-sampling is obtained by moving them (both radial and angular) with steps of the order of $0.5\ m$.

3.1.1 Spatial Interferometry

To obtain an image of a sky area is necessary to perform for every single point of the u, v plane the spectrographic interferometry. Every single point (u, v), acquired by the

interferometer, gives the spatial Fourier component for a fixed distance between the sources contained in the sky area in observation and in a direction parallel to the telescope baseline and for the various spectroscopic components.

The Van Cittert-Zernike theorem indicates the possibility to obtaining a good approximation of the distribution of the sources, even if the u, v plane has not been completely filled.

3.1.2 Spectrographic Interferometry

To perform the spectrographic interferometry, the combination of the two beams coming from the two telescopes, can be sent to a single-pixel detector and this acquisition, made as a function of the delay, is the interferogram, whose Fourier transform gives the spectral frequency of the source.
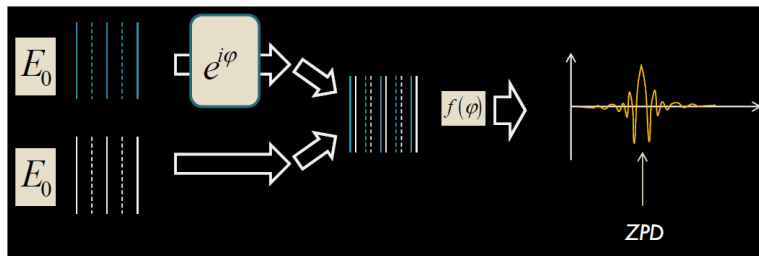
Assuming that the delay is introduced by varying the optical path of one of the two beams by means of an optical delay line that moves with constant speed v, making an acquisition of the signal intensity in function of time with an acquisition time equal to Δt, and then the spectral analysis of this signal, we will be able to see a maximum frequency determined by the acquisition time (Nyquist theorem), equal to:

$$f_{max} = 1/(2 \cdot \Delta t)$$

which corresponds to the minimum wavelength detectable (maximum spatial frequency), given by the relation:

$$\lambda_{min} = v/f_{max} = 2 \cdot \Delta t \cdot v$$

The max measurement period T, will correspond to the minimum detectable frequency, equal to

$$f_{min} = \frac{1}{T}$$

The maximum wavelength to which the instrument is sensitive will be equal to the maximum optical path difference which can be in turn expressed through the period T necessary to scan it (at speed v).

$$\lambda_{max} = \Lambda = v \cdot T$$

If we want a spectral resolution equal to R:

$$R = \frac{\lambda}{\Delta \lambda} = \frac{v \cdot T}{2 \cdot \Delta t \cdot v} = \frac{T}{2 \cdot \Delta t}$$

The resolution is determined by the ratio between the duration time of the scan and the double of the sampling time.

In summary:

• The maximum wavelength is given by the maximum optical path difference introduced (maximum distance made by the slide);

• The spatial frequency of the maximum or the minimum detectable wavelength is given by the Nyquist frequency and then by the spatial sampling (distance made by the slide between an acquisition and the other).

3.2 TECHNOLOGY STUDY AND TRADE OFF CONCERNING THE FIR INTERFEROMETER STRUCTURE (FREE-FLYER, TETHER, STRUCTURALLY CONNECTED)

In this section we give brief indications about the performed trade-off concerning the satellite structure (free-flyer, tether, structurally connected), to select the well studied FIR Interferometer mission concept denoted as Spiffy, after described. This section follows the previous work already described in DEL_1.3.

3.2.1 Formation Flying

While a prevalent idea considers formation flight to be too expensive and far too complicated, it is still surrounded by a certain excitement, as was clearly demonstrated during the recent Conference on Spacecraft Formation Flying Missions and Technologies (5th SFFMT) organized by DLR in Munich, May 2013. So far, none of the proposed free-flyer projects of the precision class required for far infrared interferometry (TPF, Darwin, Pegase, FIRI, …) have been selected by their respective agencies. It is clear, as pointed out by Rupp et al (2013), that the system architectures poses great challenges in the areas of on-board sensing and actuation, high-level mission management and planning, as well as distributed fault detection, isolation and recovery, extending well beyond the theoretical precision and fuel expenditure calculations often put forward in the project presentations. Previous mission failures and terminations decrease the level of confidence in multi-satellite systems. Examples include NASA's Demonstration of Autonomous Rendez-vous Technology (DART) mission in 2005, which ended in an unintentional collision with the target satellite, and the U.S. Air Force TechSat-21 formation flying experiment in 2005, which was terminated due to technical issues "far more challenging than originally thought" (Rupp et al 2013).

The early free-flying experience indicates clearly the necessity of precursor technology demonstration missions for autonomous rendez-vous, proximity operations and formation flying. The PRISMA mission launched in June 2010 realized an important step towards practical implementation, when a large variety of flight tasks and guidance algorithms were demonstrated. In particular, aspects of formation flights relative to a non-interferometric astronomy mission, NEAT, where a long-focal-length telescope objective is placed on a separate satellite from the detector satellite, were tested (Delpech et al 2013). With a separation of 12m and an accuracy target of 10cm, the requirements of such a mission are quite far from the performance required for an interferometric observatory. Still, reporting stability better than 4 cm (rms) during successive re-pointings between a set of celestial targets, the results obtained by this demonstration are promising, especially taking into account the stringent environmental and operational constraints of low orbit. Going to higher orbits and using finer equipment for both metrology and actuation should allow for considerable performance improvements (Delpech et al 2013). Still, it is clear that reaching navigation precision in the μm to mm range, for which the use of optical rather than radio-frequency navigation sensors will be necessary (Rupp et al 2013), will require considerable development efforts.

Particularly interesting in this context are the ESPRIT (Exploratory Submm-Interferometric Space Radio Telescope) mission. In this mission concept the far-infrared space interferometer consisting of 6 free-flying elements, each with a 3.5m telescope with heterodyne receivers in the range 0.5 to 6 THz. The aim of the mission is to accive in the THz range the angular and spectral resolution not yet

covered with the actually telescope, giving acces in a frequency range of prime importance for modern astrophysics - ALMA (Atacama Large Millimeter Array) has a sensitivity and angular resolution only to frequencies up to about 1 THz, while the HIFI instrument for ESA's Herschel Space Observatory has an angular resolution 10-30 arcsec at frequencies $>$ $2 \, THz$. The proposed mission will permit observations of regions with star and planet formation with adeguate high angular and frequency resolution in the full THz range.

In this mission concept are considered six satellites simultaneisly inserted in a L2 orbit with a single launcher. Each satellite is a telescope with subreflector that unfolds in space.

The six satellites will be positioned in space in a three dimensional configuration so to avoid problem of collision, seen figure_3.2.1-1 where it is possible to seen also the u, v coverage which points are obtained combining the down converted and digitized signals of the elements in a correlator.
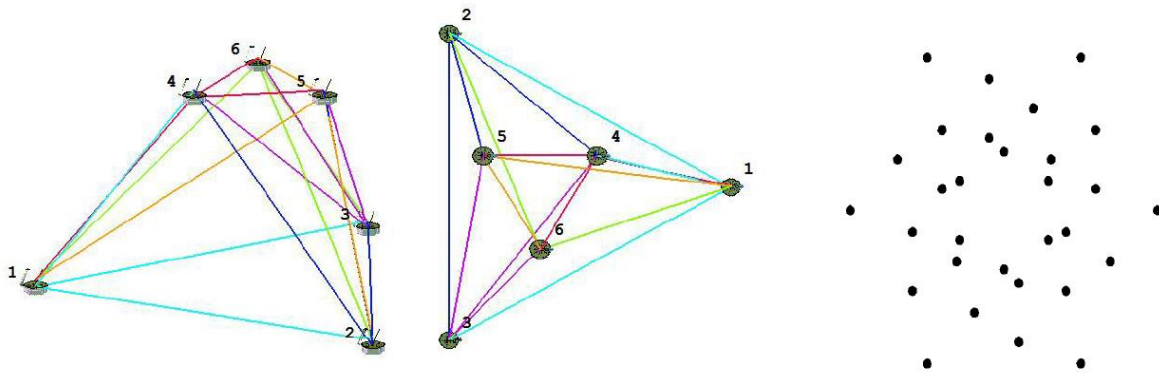
Figure_3.2.1-1. *Three-dimensional ESPRIT formation flight (left) and corresponding UV-plane coverage (right).*

The formation fligh is obtained using small ion thrusters like FEEPs (Field-Emission Electric Propulsion). Due to weight of the system and power constraints it will not be possible to move the satellites very quickly, giving also limits in the number of instantaneous configurations; it will take several days before the array has expanded from its smallest configuration to its full size of around 1 kilometer.

The heterodyne detection technique is used in order to achieve a very high spectral resolution. In the coherent (heterodyne) detection the high spectral resolution is easily achieved due to the facts that the output (IF) signal can be copied/split and amplified without adding noise, and spectral analysis can be done with digital correlators ovoiding the noise ususlly introduced by the optical delay lines.

The main advantages of the heterodyne technique are connected to the fact that the telescope and the optic operate at environmental temperature ($\approx 90K$) determining a lower system complexity with increased mission life time and saving launch mass, forthermore, for a heterodyne interferometer, the correlation is done after detection and amplification of the signal. This means that the signal can be "multiplied" in as many copies as needed. As a consequence, the number of antennas for a heterodyne space array is not limited by the signal itself but rather by other considerations such as launch mass. Since the signal has to be correlated before detection, only a limited number of antennas can be used because the available signal power needs to be divided for correlation. Thus, the proposed six-element free-flying interferometer can be configured in three dimensions, avoiding

collision danger. To limit the complexity of the metrology for measuring the distance between elements, the three dimensional configuration are obtained putting the elements in two planes with three mirrors in each plane as shown in Figure_3.2.1-1. As already stated each of the six elements houses its own correlator, permitting a common design for all the six elements.

In this mission concept an accuracy of $\sim 1-5 \ \mu m$ in the distance determination is required, the positions should be recorded continuously, also during movements of the satellites, using an optical system based on laser beams. This metrology information will be used in the global central geometrical model to provide the fringe stopping phases. The most stringent navigation requirements are for relative satellite movements to allow for fringe-stopping.

High angular resolution imposes stringent requirements on the pointing accuracy, proportional to the diffraction diameter this is roughly a factor of 10 more stringent than what is being provided today in ESA's space missions.

Concerning the central control and earth communications, this is very demanding because the positions of satellites should be (continuously) interpolated between known points using a dynamic model of the array element movements and information on velocity and acceleration of the satellite (aided by extrapolation of past movements) so to satisfy the metrological requirements.

The launch configuration for the elements is made small by folding the deployable boom secondary support structures into the cavities of the off-axis telescopes. Conceptual designs indicate that all six elements could be fitted into a cylinder $10-11 \ m$ high and four meter in diameter and could be launched on a single rocket.

Conclusions - Formation flight appears very promising but still, from the technological point it will require large development efforts to become practical at the level of precision required expecially for ITD at level of 100m as we considered in the FISICA study definition. We therefore do not consider this technology for the present study. Developments in this field should be closely followed, however, and it will certainly represent a promising, and even obligatory, technology for the distant prospects of kilometric and supra-kilometric interferometers.

3.2.2   Tethered formation

The early idea dealing with the use of tethers in the spacecraft formations flying are from the 1970s and 1980s. The studies are focused on the concept of the tethered configuration without considering the tether dynamics and control. Detailed analyses on the dynamics of tethers for formations spinning about their bore sight, on the retargeting of the spinning formation attitude and on the stabilization of the individual tethered units of the formation were conducted successively. Analysis that makes use of the knowledge acquired from a number of tether missions in Low Earth Orbit (LEO) led to the development of the SPECS study.

Dynamic analysis and control of tethered formations has been reported, indicating that further development and testing of tethers in space will be necessary as a first step toward the implementation of a Far Infrared Interferometer due to its severe requirements on angular resolution and image quality.

In principle, the interferometer rotation to cover the entire u-v plane can be achieved at constant angular momentum about the beam combiner with no propellant consumption. In practice, thruster fuel is used to keep the tangential velocities constant and to reposition the orbital plane to acquire new astronomical targets and to correct the attitudes of the spacecraft and beam combiner.

To avoid noise in the spectroscopic measurements, the satellite oscillations around the ideal relative positions should not have frequencies higher than the fringe tracker bandwidth, which depending on the specific design and conditions. This noise perturbs the spectroscopic measurements by means of a jitter effect; in particular the noise to consider is in the band $(3 \cdot 10^{-2} - 10 \text{ Hz})$ where the spectroscopic measurements are performed.

Compared to a free-flyer system the tethered one con rotate at a higher rate, showing better stability (gyroscope effects) so as to be less sensitive to external perturbation and improve the system pointing.

In principle an interferometer with tether connection from the point of view of its dynamic can be considered as a system with boom connection especially for what concern its operation. It can be operated maintaining a constant angular momentum during the coverage of the u-v plane, without consuming propellant, or at tangential velocity constant, managing the tangential thrusters, so to permit to the collectors to operate within the desirable range for image synthesis.

The retargeting of an interferometer with tether connection can be obtained using thrusters disposed in the telescope and able to give harmonically varying forces.

As an example: for a collector mass of $3200 kg$ at a distance of $500 m$ with tangential velocity equal to $2.15\ m/s$, an angle $\vartheta_p = 3°$ is obtained in three complete rotations of the system in $1 hour$, with the two thrusters, acting out-of plane and in plane, with a maximum value equal to $0.164\ N$.

Propellant total mass to cover the whole 95.5 radians of retarget angle in the course of a mission, at a tangential speed of $2.15\ m/s$ amounts to less than 1%, or about $27\ kg$ of fuel per collector equal to about the 6% over the mission lifetime.

Specific requirements concerning the use of the tethers are connected to its survival in the space environmental in L2 during the mission duration of 5 Years. In order to increase the probability to survive to micrometeoroids in L2, the tether has been designed not as a single line (single failure) but in a multi-line shape. In particular has been studied different combination of line: one line tether; 2-parallel line interconnected every 100 m; 4-parallel-line interconnections within each tether branch.

Conclusions - Preliminary analysis demonstrated the possibility to use the tether for the implementation of a FIR Interferometer as the one conceived for SPECS, where the ITD is of the order of $1 Km$, but further analysis and experimental activity are necessary regarding the followings topics:

- Damping of tether vibrations;
- Reconfiguration of the baseline;
- Retargeting;
- Positioning of the spacecrafts to better than 10 cm during observations;
- Measurement of accelerations transmitted by tethers to the satellites;

- Minimization or cancellation of torques transmitted by the tether to the spacecraft, through center of mass or attachment point control.
- Tether technology development in ground experiments and flight demonstration at short and long tether lengths.

In every case, as we can see in the following section the similarity between the satellites connection using tethers or structure are really very similar and the obtained concepts results for one configuration can be used for the other one.

3.2.3   Structurally connected telescopes

The most conservative approach to long-baseline interferometry in space is the structurally connected design. Here, deployable booms constitute a rail on which the two telescopes are wheeled in and out in order to cover a range of baseline dimensions. Light-weight booms will most likely be made in the form of a truss structure, benefiting from high stiffness and low weight. These can be devided into segments and packed into the fairing of a launch vehicle, as in the ESA-CDF study (ESA report 2006) and in the SPIRIT proposal (Leisawitz et al 2010), see Figure_3.2.3-1. The maximum baseline for this concept is 36m. The same approach on a smaller scale (8m baseline) is currently being built as a bolloon-borne experiment (Reinhart et al 2014), see **Figure_3.2.3-2**.
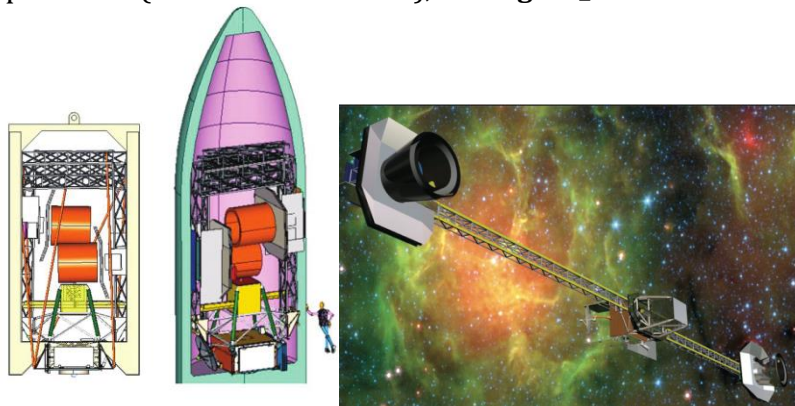
Figure_3.2.3-1. *Stowed (left) and deployed (right) truss structure for the SPIRIT proposal (Leisawitz et al 2010).*
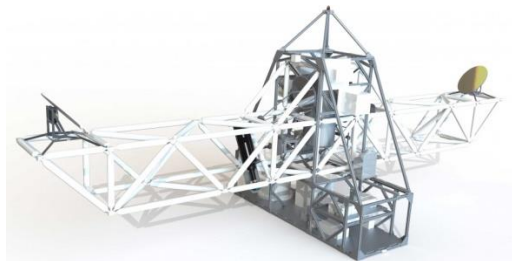
Figure_3.2.3-2. *The BETTII balloon-borne interferometer (Reinhart et al 2014).*

Truss-based constructions in space have been much developed, notably in the case of the international space station built around a truss of total length 109m [NASA ISS website], see **Figure_3.2.3-3**3. Ongoing developments of deployable truss structures with extremely compact launch configurations, such as the ADAM collapsible truss system from Able Engineering Inc. (Tibert 2002), provides hope for extension of the SPIRIT concept towards

the 100m baseline considered in the FISICA study. The ADAM system is deployed as shown in **Figure_3.2.3-4**_3.2.3-4 resulting in a space-proven and highly scalable structure, the longest example of which reached nearly 61 m. Another example, shown in **Figure_**3.2.3-5, is ROCCOR collapsible and roll-able truss using composite slit-tube booms as a repeating structural unit. This patent pending design offers high packaging efficiencies and outstanding deployed properties (bending and torsional stiffness and strength). The joints between longerons, battens and diagonals do not need to articulate allowing simplified connection methods (riveting, ultrasonic welding, bonding) leading to high manufacturing efficiency and reduced cost.

Figure_3.2.3-33. *The international space station, built around a 109m long truss.*
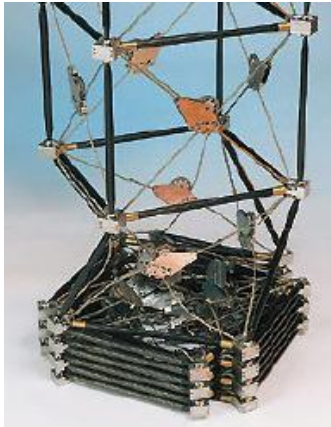
Figure_3.2.3-4. *The ADAM collapsible truss system from Able Engineering Inc. (Tibert 2002).*
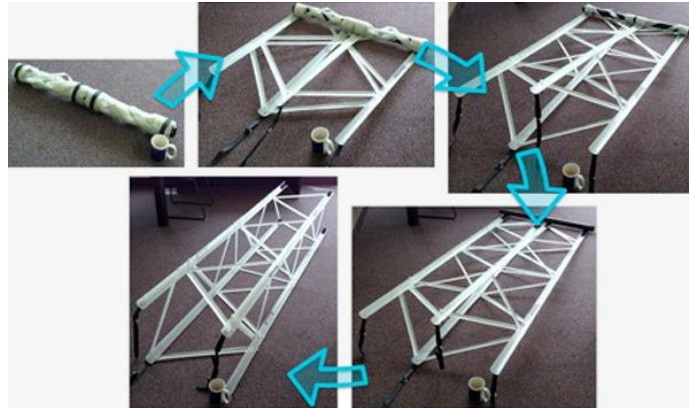
Figure_3.2.3-5. *The ROCCOR collapsible and roll-able truss [ROCCOR web site].*

3.2.4 Trade-off summary and conclusion

Following this review of current status for formation flight, tethers, and trusses, we conclude that for the current proposal of a 100m baseline structure, the most technologically advanced option is the stiff truss structure. Such structures are routinely used up to these dimensions and on-going developments promise hope for extremely compact launch configurations.

For longer baselines, possibly up to 1km, tethers are expected to provide an excellent alternative. Formation flight, still considered immature for the precisions required for interferometry, will probably be mandatory for supra-kilometric larger baselines.

3.3 SPIFFY CONCEPT

The requirement for angular resolution in the typical range 0.1 – 0.7 arcsec, and crucially achieving 0.1 arcsec at 40µm, dictates that the telescope will be an interferometer with variable baseline of up to 100m. The default design is currently for a 2 telescope system performing aperture synthesis interferometry. The requirements of the telescopes and optical configuration to relay the beam to the instrument hub beam combiner will now be considered.

In order to provide a realistic and timely contribution to the study of a space-based FIR interferometer, the present study has been concentrates on a moderate concept referred to as SPIFFY. In **Error! Reference source not found.** 3.3-1 and in the two following tables are reported the configuration and the principal parameters considered in the trade-off analysis performed in the FISICA study, concerning the medium ground between the minimal baseline and the over-ambitious kilometric baseline.
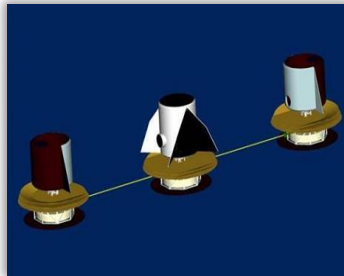
Figure_3.3-1. *SPIFFY configuration, a medium ground between the minimum baseline and ambitious formation flying baseline*

Table_3.3-1. *Main characteristics for the SPIFFY configuration*

Instrument Characteristics		
Primary diameter	2 m	ext
Baseline Range	0, 10-100m	ext
Optics Temperature	4K cryo-cooled	[1]
Configuration	Rigid Truss or Tether	[3]
Mission Lifetime	3-5Yrs	ext
Sky Coverage	+/- 20 deg. from ecliptic	[1,2]
Spectral Coverage (µm)	25-50,50-100,100-200,200-400	[1]
Detector Arrays (35/70/140/280µm)	2x(28x28/14x14/8x8/4x4)	[*]

Table_3.3-2. *Derived parameters for the SPIFFY configuration*

Angular resolution	0.1 (lambda/100um) arcsec	[1]
Field of View	1 arcminute	[1,3]
Spectral resolution	~3000-5000	[1]ext.
Point Source Sensitivity (5s in 24hrs) -) Spectral Line (10^{-19} W/m^2) -) Continuum (µJy)	(35 / 70 / 140 / 280) µm 0.7 / 0.4 / 0.3 / 0.3 3.5 / 5 / 7.5 / 12	Ext.
Typical Observation Time	1 day	[1]

(*) *Sensitivity ext. on primary scaling only. Detector numbers are scaled to maintain f.o.v. size*.

The SPIFFY concept originates from a merging of the ambitious concept for SPECS with a "scaled up" version of the SPIRIT concept and a logarithmic middle ground between the latter and the ESA FIRI cosmic vision proposal concept formation flying configuration. While this concept is listed in order to allow a middle ground between a rigid short

baseline boom interferometer and the ambitious formation flying, it does assume technical solutions which are less defined than either of the other concepts.

In the preliminary works with which the scientific requirements are translated into a requirements for the measurements, the following questions are taken into account:

- ➤ Is high-fidelity imaging required?
- ➤ Which are the highest priorities in wavelength coverage?
- ➤ What kind of spectral resolution throughout the available bands is of interest?
- ➤ Is there a Time-Transient nature to the observation?
- ➤ Is an instantaneous field of view of 1 square arcmin sufficient?
- ➤ Is the field of regard constraint a major limitation for the proposed science?

To these scientific requirements has been considered also several external constraints:

- Lift capacity to the desired orbit (Sun-Earth L2)
- Interferometers dimensions and weight.
- Affordability (Technology readness, cost)

Another point taken into consideration has been the public interest and the affordability in the next decades.

4 LOW-MASS CRYOGENIC DEPLOYABLE TELESCOPE MIRROR STUDY

4.1 INTRODUCTION

The requirement for a lightweight, stiff and dimensionally stable material for future space-astronomy and earth-observation missions is unquestionable. Large and precise mirrors with reduced mass are fundamental to support future scientific advances, within the envelopes imposed by project-cost and launch-vehicle capacity. Reducing mirror-mass for a defined overall mass also releases mass-budget for instrumentation. To this end, the development of a carbon fibre reinforced polymer mirror has been discussed in Deliverables 2.2 and 2.4.

Table_4.1-1 *FISICA Baseline Mirror Specifications*

	Case 1	Case 2
Mirror will be deployable (Segmented Primary)	No	Yes 7
Preferred size and shape of each mirror segment	NA	Hex
Deployed overall size of clear aperture	2m	6m
Deployed overall shape	Circular	Hex
Central perforation?	No	No
Nominal form	Parabolic	TBD
Areal density target (~1.10 areal density of Hubble)	<30kg/m2	<30kg/m2
Preferred interface to sub-system	3-point	TBD
Approximate focal length	1m	<2m
Surface form error specification	275nm	275nm
Surface texture ("roughness") specification	80nm	80nm
Mid spatial frequency specification	TBD	TBD
Maximum edge-misfigure	TBD	TBD
Maximum edge dead area (non-reflecting)	N/A	TBD
Surface coating	TBD	TBD

4.1.1 FIRI Requirements

A FIRI mission-concept requires a pair of circa 2m diameter primary mirrors, but with the additional requirement of being cooled to ~4K, in order to limit thermal background emissions in the infrared. CMA Inc are leaders in the field of CFRP mirrors and have produced numerous optical telescope primaries for terrestrial-based observations, but have not been so widely deployed for space telescopes. The Planck telescope, launched alongside the Herschel Space Observatory, used a CFRP sandwich structure, operating at 40K to observe the 0.3-10mm wavelength range. The CFRP face plates and the core were made from the same material, eliminating differential CTE effects in the sandwich.

4.2 CURRENT STATE OF THE ART

The current state-of-the-art manufacturing method for creating a CFRP mirror is to use a polished mandrel to replicate the mirror with the inverse form and similar texture, aspects of which have been patented by CMA Inc. This method has been used successfully, according to CMMA literature, for a number of optical primaries. This requires a mandrel to be produced that has precisely the opposite form to that of the mirror, and polished to the required texture. The addition of a resin-rich layer (approx. 0.25mm thick) on the surface of the CFRP mirror eliminates fibre print-through, and enables the mirror surface to take the polished surface of the mandrel. Low and mid spatial-frequency errors are also mitigated by this method. If a suitable release agent is used, the mirror separates from the mandrel with relative ease, following conventional curing either in a vacuum bagged arrangement in a convection oven, or an autoclave. The result is a smooth fibre-reinforced polymer mirror that achieves the required surface and form requirements, which can then be vacuum-coated with a metallic layer in the standard manner to deliver a specular finish. Numerous patents claim variations on the replication method, such as using honeycomb cores.

For most monolithic mirrors, large mandrels are required, which constitute tooling not used in the final mission. Mandrel cost can be significant, particularly if fabricated in a low-expansion ceramic such as Zerodur or ULE, and further increased by the typically extended optical polishing times. The other difficulty is that of measuring the convex aspheric surface, which requires significant investment in metrology infrastructure. Current methods can achieve sub-micron accuracy but metrology below that is a distinct challenge. Set against this tooling cost, is that multiple mirrors can be replicated off a single mandrel. For an interferometer, two flight mirrors are required. However, over the mission development, some or all of Breadboard, Engineering Model, Flight, and possibly Flight Spare mirrors-pairs may be needed. Mandrel cost then ceases to be a significant issue.

Repeatability of replication using the same mandrel is therefore important, and reputed to be consistent for over 60 replications. This may well be the case for form accuracy but for texture there are doubts that this is possible. Curing and fabrication CFRP components is a fairly arduous task and the mandrel would be vulnerable to damage. Additionally the use of release agent significantly effects the surface texture of the final mirror in comparison to the mandrel.

4.3 THERMAL DISTORTION

For the FISICA project a distinct challenge is the need for the mirror to be cooled to 4K during operation, to limit thermal background emission. When cooled to such a low temperature all materials change volume to a significant degree. Additionally, material properties such as ductility and hardness may also be altered. The lack of material data for carbon fibre reinforced polymers at low cryogenic temperatures has proved to be a difficulty from the outset of this project. There were two main issues reviewing the literature, firstly CFRP is a category of materials rather than one distinction composite, which creates confusion. There is huge diversity in carbon fibre reinforcements, from precursor material to fibre tow and stiffness. Additionally, the matrix material is even more

varied and can essentially be any plastic that will bond to carbon fibres. Therefore, without knowing the distinct constituents of the material, it is not possible to draw a conclusion regarding the suitability for cryogenic operation. Secondly, literature that does specifically state the material details, tends to be tested down to only ∼ 40K. The main driver for this is the NASA reusable launch vehicle programme, and specifically for the fuel tank.

It was therefore vital for FISICA to develop an experimental procedure to obtain some material properties at 4K. After discussions with the project collaborators, it was found that the University of Lethbridge had a suitable facility that could be adapted to measure coefficient of expansion for CFRP witness samples at ∼ 4K and during warm up to room temperature. Samples were created at Glyndr University to simulate the contraction in the fibre direction, lateral to the fibres, and also for quasi isotropic samples. Results from the test were as anticipated, in that the contraction in the fibre direction (0º) was significantly less than lateral to the fibres (90º). Using a Renishaw interferometer, it was possible to measure the contraction to an accuracy of 30 picometers.

Some questions remain as to the detailed suitability of this approach. To begin with, samples cannot be created with fibres in only one unique direction, as some fibres normal to the dominant fibre direction must be used to bind the layers together. Additionally, the measurement of contraction is made in only the lengthwise direction; no measurements are possible in the orthogonal direction, as would be needed to ascertain the Poisons ratio of the material. Mechanical testing at cryogenic temperatures would also be advantageous in order to find the Youngs, flexural and shear moduli of the material at 4K, as this would increase the accuracy of any computational modelling. For this limited study possible within the FISICA resources, ambient mechanical properties were used, which was not ideal.

Coefficient of thermal expansion data from the tests at Lethbridge were transferred into an FEA model at Glyndwr to predict the magnitude of deformation in the mirror form during cool down. It was found that predicted deformation was significant, in the region of xxxnm PV and that the material initially chosen, (a carbon fibre reinforced epoxy resin known as MTM44-1), in its original form, would not be suitable for a cryogenic CFRP mirror. The layup of the CFRP mirror was symmetric and balanced about the mid-plane in an attempt to create a quasi-isotropic layup. The cause of the deformation stems from un-equal CTE in the two in-plane directions. Low CTE in the fibre direction and high CTE lateral to the fibres causes a mismatch when subjected to a large change in temperature. Deformation is further exacerbated by the distances of each ply from the mid-plane, causing a forced couple that doesn't not balance out due to the curvature of the mirror.

One method of reducing the deformation is to develop the material properties of the resin in particular, to be more suitable to cryogenic operation. CFRP materials are known to be tailorable for near zero CTE, but this is over a relatively low temperature range from room temperature to ∼ 220K. When more extreme temperature ranges are required, the resin needs to be carefully chosen to minimise the expansion (or contraction) coefficient. The material chosen for the CFRP mirror application MTM44-1 because it is widely available, has low CTE for an epoxy resin prepreg, and, importantly, is also NASA qualified as regards its outgassing in space. The production and widespread use of carbon fibre reinforced polymers is dominated by the aviation industry, therefore there is no large capacity for alternate projects. Therefore directly engaging with material suppliers to tune the

composition is difficult unless there is a significant budget available (outside the scope of FISICA). Additionally, specialist materials, such as cyanate ester resins which have lower CTE values than epoxy resins, are not often produced, and so obtaining small quantities for studies such as FISICA is not possible.

An additional test performed in the Lethbridge cryostat cycled a quasi-isotropic CFRP sample 3 times to measure if the contraction was repeatable. Crucially it was found that the contraction increased with each cool down. Although the reason for this change is unknown, it is suspected that the CTE mismatch between the fibres and resin is causing high strain at the fibre/matrix interface inducing micro cracks. This issue as it stands today would prohibit ground testing of a flight-mirror at its operating temperature, as the form will not be re-established after warm-up for launch and then cool-down in orbit.

In general, mirror deformation can be manageable and potentially corrected by adaptive means (applying adjustable forces), provided the deformation is predictable and repeatable. Once again engagement with the material supplier is vital to reduce hysteresis. The introduction of an intermediate layer at the fibre/matrix interface has also been investigated elsewhere and could prove to reduce the strain at this boundary.

4.4 SAMPLE MANUFACTURE

Samples manufactured at Glyndwr

Some samples of CFRP mirrors were manufactured using the replication method at Glyndwr for this project. The texture of the final CFRP mirror was considerably inferior to the optical flat upon which it was cured. This results was not unexpected and further development in this area at Glyndwr is required. It is expected that material selection and refining of the fabrication process will reduce roughness of the replication optic to near to that of the optical flat.

Due to the nature of the replicated surface texture, the mirror sample was then ground and polished by hand. The trial used traditional hand polishing techniques and used a grit size of between 5-15µm. It was found that the polishing caused micro scratches on the surface of the mirror, most likely due to either the polishing pitch being too hard or the resin being too soft to withstand the grit. Once the micro scratches became more apparent, polishing was stopped and the surface texture measured using the white light interferometer. The results shows some improvement in texture as compared to the replicated surface but not enough to reach the FISICA requirement. The 3 dimensional view of the texture found many surface defects, mostly holes that were most likely caused either during cure or by trapped air during the replication procedure. It is therefore advised that further trials are conducted and that the top layer of resin is ground for a longer period before the finer polishing begins. Polishing consumable suppliers should also be consulted to optimise the polishing media, and sub-micron abrasives will almost certainly be required.

Form error is a key issue in fabrication of CFRP mirrors due to the volumetric shrinkage of thermoplastic matrix composites. This phenomena causes spring (change in radius of curvature) when making curved surfaces. For spherical or parabolic mirrors this effect can cause astigmatism. The mandrel used to cure CFRP samples reported in this document was made from Pyrex due to its moderately low thermal expansion, stable properties at cure temperature, and manageable cost. Additionally, Pyrex opens the possibility of using advanced curing methodologies such as microwave curing to reduce thermal gradients within the mirror substrate that further increase spring. A nominal 3m ROC was adopted

for ease of measurement and a 200mm diameter mandrel purchased. It was found that the Pyrex mandrel actually used had 3.01m RoC as measured on a coordinate measuring machine (CMM). Once cured, the CFRP sample of 180mm diameter cast on this mandrel was measured to have a RoC of 2.95m, and a form error of 70μm PV, with respect to the nearest-fit sphere, measured using an Extended Range Form Talysurf profilometer (one of the few that Taylor Hobson built). This result constitutes a baseline for future work. In particular, it is already within the capabilities of corrective post-polishing, in the unlikely event that further developments of the replication procedure do not substantially improve the errors.

4.4.1 Metrology issues and their resolution

The Extended Range Form Talysurf profilometer (300mm scan-length) became increasingly unreliable, and finally developed a serious fault that could not be rectified within the FISICA project schedule. The CMM was limited in precision to a few microns and was not suitable for measurements of distortions and surface-form at the sub-micron level. To recover from failure of the Form Talysurf, a new measurement probe was procured and used in conjunction with an existing 1.2m Zeiss air bearing turntable. The part was mounted off-centre on the turntable, the turntable rotated under computer control, and the probe used to measure along multiple arcuate scans. This provided a simple but precise profilometer, which had the additional advantage over the Form Talysurf that the probe selected was non-contact in operation – thereby avoiding potential damage from a stylus probe to the relatively soft resin layer on the replicated mirror surface. Measurements are reported under Deliverable 2.2 and the results show correlation with the CMM data for the radius of curvature. The probe calculated the maximum deviation of the form to be 70 μm PV. Note that this result has some residual error in it due to tilt within the air baring table which will in the future be calibrated. The demonstration of this new measurement method is very relevant to any future developments of the technology, as it is inherently capable of measuring very large mandrels and replicated mirrors (in its current embodiment up to 1m, and with modification, up to 2m diameter).

4.5 OVERALL STATUS OF CRYOGENIC CFRP MIRRORS

One issue that is clear from this study is that the low density of CFRP mirrors is unrivalled for this application. At present, the technology readiness level is low. As mentioned previously, form error and texture of the mirror after replication did not meet requirements, but present a basis for a future development programme, and are already within the scope of corrective polishing. Finite element analysis showed that dimensional stability of the specific composite samples manufactured and tested was significantly degraded during cooling to 4K. CFRP mirrors can be made extremely stable for short temperature excursions, but this technology has not yet been developed for space programmes. Ultimately, it is hysteresis on cool-down, rather than expansion coefficient that is the key area that requires addressing. This is because measured form and ROC errors of the mirror after cool-down can be inversely polished into the mandrel and the replication repeated, *providing* that hysteresis is low and repeatability high. Significant investment in this area is required to develop a sub-10kg areal density CFRP mirror, but this is entirely plausible, especially if post-polishing of the replica is conceded. Collaboration and concerted engagement with material suppliers, composite centres of

excellence and optical engineers could see this technology being used on large aperture telescopes in the future.

4.6 RECOMMENDATIONS

The following outlines the key steps that are recommended to be undertaken in order for the readiness level of this technology to be increased:

4.6.1 Engagement with material suppliers

The ability to tailor the properties of composite materials to suit an application is perhaps the key driver in the broader popularity of this technology. The constituent materials of a composite combine to create properties superior to those of the original base materials. The sheer number of combination of materials allows designers to select the best reinforcement and matrix materials for the application. Fibres provide tensile strength and carry the most load in extension, but it is the resin that provides flexural strength, protection of the fibres and the ability to transfer the loading to the fibres.

For temporal stability, the resin is the most important aspect of the composites. Carbon fibres have a very low and even negative CTE over large temperature ranges. Resins tend to have a much larger CTE and so expand (or in this case contract) to a much larger extent. It is at the interface of the fibre and matrix, where the two material combine to produce an overall CTE that is greater than the fibre but much lower than the resin alone. This interface area restricts the resin from moving, but the bond between fibre and polymer causes high strain rates.

Far infrared interferometry requires the mirrors to be cooled to 4K; a severe temperature differential with respect to fabrication at room temperature. It is key therefore that the resin selected for the application has a low CTE to begin with that will be further decreased by combining with the composite, and also by a balanced fibre layup during fabrication. Cyanate ester resins possess a low CTE but are expensive and not widely used by the major industry in composite materials, Aerospace. It is for this reason that cyanate ester based composites are difficult to purchase.

For CFRP mirror technology to progress it is vital to engage with material suppliers or for materials to be developed on a lower batch scale within institutions. MTM44-1 epoxy resin was used as a matrix for the FISICA study and, although it was space qualified by NASA for outgassing, gave inadequate performance for the final application. Material combinations do exist that would be highly promising for this application; however procurement was outside the materials budget available for this preliminary phase.

4.6.2 Development of fibre architecture

By their very nature, composite materials are anisotropic, resulting in an adverse effect on bulk expansion/contraction over environmental conditions that the material is exposed to. Although various strategies exist to mitigate these effects, for high precision applications such as telescope mirrors, the anisotropy is still a serious concern. Part of the anisotropy is caused by layers of 2-dimensional plies that are formed when creating the mirror. These layers are formed of unidirectional prepreg that exhibit very different properties in

orthogonal directions. Different ply orientations are carefully managed in an attempt to balance these effects, residual anisotropies in the 3D structure created remain.

Advanced production techniques for composites have begun to yield components that have properties that have similar magnitudes in both in- and out- of plane directions. Three dimensional braiding of fibres can substantially reduce the differential properties of a composite by binding the fibre in a repeatable manner. By reducing the volume fraction of resin to a minimum, the anisotropy of the laminate can be further improved.

Other advanced technologies such as random fibre path orientation, random chopped mat fibres also have potential, although repeatability in fabricating the final components is of concern.

4.6.3 Residual stress limiting manufacturing techniques

During cure by conventional means (convective heating), composite materials are exposed to a thermal gradient through the thickness of component. Resins tend to possess a very low thermal conductivity and diffusivity, meaning that such heat required to begin cure takes significant time to propagate through the bulk of the material. This gradient will cause curing to occur in certain areas before others, and induce residual internal stress and strain. During cure over a mandrel, these residual stresses will build and, upon release from the mandrel, will cause deformation. In industries where composites have a long history of usage, this effect is negated by under sizing mandrels and moulds to suit the spring back. However, for high precision parts, this is not possible. Additionally, these residual stresses and strains may release during operational life, either over time (in a similar mechanism to creep in metals) or after an external load is applied. In the case of composite optics for cryogenic operation, there is a clear concern that these residual stresses will be released during cool down, distorting the mirror past the deformation predicted by FEA.

For CFRP mirror technology to become more repeatable, curing method other than convective heating should be investigated. Technologies such as microwave curing could be the solution, allowing the components to cure from inside out. If the addition of convective heating is also applied, this would minimise the thermal distortion in the part.

4.6.4 Development of replication technique

It was found during this project that the replication techniques was not always accurate in creating a composite mirror representing the inverse of the mandrel surface. Literature has also shown that other workers have experienced difficulties in this regard. Further development of the precise replication procedure is required, including optimum environmental conditions, and the composition of the release agent and the uniformity of its application.

Providing that the replica has a resin-rich layer on the surface with no fibres, then the final surface form can be measured by interferometry or profilometry, and corrective polishing conducted using standard CNC techniques

4.6.5 Adaptive optics and support stucture for CFRP

The use of a thin meniscus CFRP mirror will require a concerted development programme. The areal density of such a mirror is ample justification or such a programme. However, the support structure required for such a technology also needs to be carefully considered, to

alleviate some of the thermal deformation issues as described above. The supporting structure must clearly cope with the contraction of the mirror material without mis-match introducing additional stress and strain. However, this can be turned to advantage. Using material selection and anticlastic design, it is possible that, as the mirror cools and distorts, so does the support structure but in an opposite direction, enabling the resultant force to be cancelled leaving a nominally undistorted mirror surface.

4.7 CONCLUSION

This short summary of technical advances in readiness level covers the development of a primary mirror fabricated from polymer matrix composites. It was shown that the performance of the composite during cooling is of concern, with large deformations in the mirror being predicted by FEA. It is expected, however, that an increase in the number of support points and optimised material selection could reduce this significantly. By engaging with material suppliers and manufacturers more suitable polymers could be used for this application. Budgetary constraints precluded a more extensive acquisition and characterisation of materials, especially any materials tailored for this application, or any advanced materials such as cyanate ester composites, given that these are manufactured only in large batch-sizes.

Another key concern raised in this project was the change in the temporal stability of CFRP samples if they were thermally cycled from room temperature to 4k. The additional contraction after each cycle meant that the material was undergoing change in structure or composition. The suspicion is that high strains at the fibre ⇔ resin interfaces are causing micro cracks that are enabling the resin to cause further contraction during the next cooling cycle. Once again, engagement with material suppliers should be sought to manage this issue.

The replication method used to create mirror was found to be insufficient in achieving fidelity of form and texture of the mirror. Preliminary polishing trials were conducted post-replication with a small positive effect. More extensive polishing trials should yield further improvement and the target of 20nm Ra texture is thought to be achievable, as should the form tolerance assuming there is sufficient depth of resin-rich layer to polish.

The technology to create a CFRP for a cryogenically cooled primary mirror is at a very early stage. Significant development and, ultimately investment, is required to improve the readiness level for a mission. However, the benefits of this development are clear, and a target areal density of less than 10kg/m² is not in question.

4.7.1 Summary of possible areas of development

To summarise the following research topics need to be considered in order to utilise the attractive specific stiffness and tailorability of CFRP for a cryogenic mirror, (This list is by no means exhaustive and is in no particular order):

- Fibre architecture and influence of 3D weaving on the stiffness of CFRP mirrors
- The stiffness and survivability of a CFRP chopped strand mat mirror during launch loading and operation
- Sandwich construction of a CFRP mirror and its distortion at 4K.
- The Thermal properties (CTE, conductivity and diffusivity) of the matrix, fibre and composite at temperatures from ambient to 4K

- Mechanical properties of the chosen fibre architecture of a CFRP mirror at 4K
- Coating technologies and their survivability at 4K
- Replication method to achieve FISICA specifications using CFRP on prototype mirror
- Distortion of a prototype mirror during cooling and investigation into the scalability of results
- Methods to decrease time constant for CFRP mirrors curing mechanical cooling to 4K
- Out of autoclave, novel curing of CFRP mirrors to recue residual stress
- UV degradation at Cryogenic temperatures of CFRP mirrors.
- Development of cryogenic test methods for the above.
- Long term stability of CFRP mirror at low temperature loads
- Effect of thermal cyclic loading on CFRP mirror
- Effect of vibration, via acoustic and other sources on CFRP infrared mirror.
- Diamond turning of CFRP mirrors
- Statistical analysis of the repeatability of CFRP fabrication process for far infrared interferometer mirror pair.
- The effect of ply misalignment on a CFRP unidirectional mirror when cooled to 4K.
- The influence of residual stress on a CFRP during cooling to 4K.
- Moisture ingress on a CFRP mirror cooled to 4K.

5 SATELLITE POSITIONING CONTROL-LOOP BASED ON THE USE OF AN ACCELEROMETER

In this section are reported the investigation on the technical challenges in implementing closed loop accelerometer feedback for satellite position control to satisfy positional accuracy requirements. The study is connected to the FIR interferometer in the conditions of satellites mechanically interconnected as for SPIFFY case. Particularly, it will be analysed in detail the case of a rigid truss, identifying the necessary algorithms to maintain satellite positions in respecting of the requirements. The team from AGI with experience of similar on board systems conducted this effort using inputs from INAF-IAPS and substantial coordination with LAM, where development of a metrology test-bed using a nano-satellite has taken place. The objective of this study takes into account the particular maneuvers that the interferometer must perform during the observation modes and its environmental conditions, particularly to the dynamical noise, both in the band, in which the satellite must be controlled, and out of this (to avoid accelerometer saturation and aliasing effects).

At the end of this section are reported the informations concerning the study of a high sensitive accelerometer prototype defined and implemented so to be used for spacecraft control loop, in a FIR Interferometer space mission.

In sintesy, the main subjects of this section are:

i)   study of the accelerations acting on the interferometer, principally due to its dynamical movements and to the noise present on their satellites,

ii)   possible use of the accelerometer with respect to the interferometer metrological problems,

iii)   experimental and theoretical study of the technical challenges in implementing closed loop accelerometer feedback for satellite position control to satisfy positional accuracy requirements.

iv)   definition of an accelerometer meeting the requirements imposed by its use in a FIR interferometer space mission and implementation of a prototype of accelerometer with such characteristics.

The study has been performed in close connection with the activity concerning the task 2.3 "Validation of key technologies with nano-satellite". In this contest and a prototype of accelerometer to be validated has been also defined and implemented: Description of this activity will be given in the section_6.

Remarks:

a)   Similarity between the satellites interconnection with tethers and mechanical boom is very strong and several considerations here reported for the boom interconnection can be retained also for the tethers configuration.

b)   Several parts of the activities here reported has been already described in the DEL_1.3, but it is retained that the repetition is usefull for the completeness of the argument.

5.1   METROLOGICAL PROBLEMS AND DYNAMICAL CONTROL.

The gravity gradient acting on the interferometer placed in the Lagrange point L2 (candidate orbital location) is very small and so the relevant accelerations present on the interferometer are those due to its rotation performed around the ILS (Instrument Line of Sight) combined with the variation of the ITD. In this condition accelerometers installed on the telescopes can measure directly their tangential and centrifugal acceleration, related to the ITD and to the rotation angles (determined by the star sensors); by means of a feed-back system, this information can be used to control the thrusters, so to force the system to follow an opportune control law, for the variation of the ITD and angular velocity. The control can give the possibility of the acquisitions of the u, v points in the minimum time and best conditions optimized for the relative observation mode.

Together with the analysis of the control laws for the telescopes of the interferometer, it is necessary to take under control the metrological problems for the accuracies required in the measurement and/or determination of the relative distance between the telescopes and the requirements for the levels of noise present on them, so to keep the noise for the Optical Path Difference (piston, tilt and wave-front error) within the levels required for the visibility of the interferometer. Placed in the Lagrange point L2, the interferometer is maintained in this position by means of traditional techniques of attitude control, to which will also be entrusted the task to point the telescope towards the observed sources. In the next phase of operation of the interferometer, it will rotate around the axis passing through the sources and for its HUB (axis ILS$_{HUB}$), reducing the distance between the two outer satellites-telescopes ($R_1(t)$, $R_2(t)$) so to cover the u-v plane.

In a first idea the two satellites go through a spiral at a constant tangential velocity (about one meter in $25s$) with an appropriate control law that will govern the distance between the two telescopes and the rotation speed of the interferometer, so to ensure maximum coverage of the $u - v$ plane, in respect of its functionality from both the spatial and spectroscopic point of view; it is clear that also other modalities to cover the u-v plane will be considered, as for example to readjusting the satellites baseline every half turn. In L2 the dominant accelerations acting on the interferometer are essentially the inertial accelerations, determined by its rotation, in particular the centrifugal accelerations are of the order of 10^{-3}g. The measurement of these accelerations with precision of 10^{-8}g, should allow the control of the system (this at least for the tethered and booms connection between the two telescopes) through the variation of the distance between the two satellites and its rotation, in accord to the law of conservation of its momentum. The variations of these accelerations are expected at periods of about 24 hours, which represent the estimated time to walk the spiral so to cover the entire plane $u - v$. Also, we can underline the fact that the difference between the two measured accelerations is connected to the angular system rotation and to the distance between the two points at which the radial accelerations are measured:

$$a_d = \omega(t)^2 \cdot R(t),$$

Where

$$R(t) = R_1(t) + R_2(t)$$

The formula gives the opportunity to recover the absolute distance between the two telescopes, if ω is measured (star sensors or gyroscope).

In **Error! Reference source not found.** is reported a general scheme of the possible control loop for the dynamic control of the interferometer; the system is monitored by means of an IMU that gives information on the interferometer angle rotations, and to the accelerometers that monitor the centrifugal and tangential accelerations. The monitored values will be compared by the ones coming to a control law and the error values are sent to the actuators (thrusters and step motor).
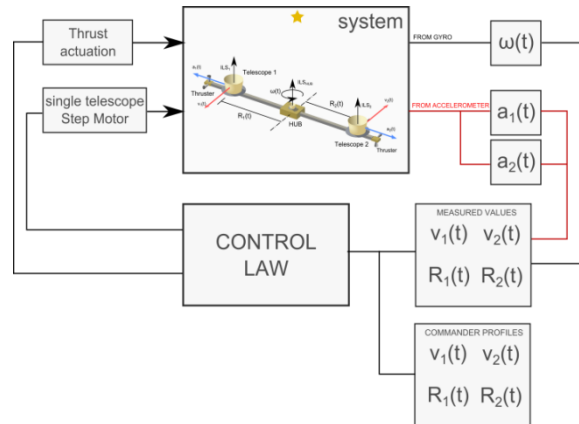
Figure 5.1. *Possible scheme of the interferometer control loop*

5.2 ACCELERATIONS ACTING ON A FIR SPACE INTERFEROMETER

In this subsection are reported the principal results concerning the evaluation of acceleration acting on a system of satellites disposed in L2, due to the gravity gradient and to the system dynamics for the interferometer that move to cover the uv plane, in particular are considered the acceleration acting on a system of two telescopes connected to a central hub by means of a mechanical interconnection: tethers or support boom.

As we can see from the indicated results of this analysis, the value of the accelerations due to the gravity gradients acting on the telescope is several orders of magnitude less than the one arising from the telescope dynamics necessary to follow during the science observation mode. Anticipating a conclusion of this study, we can assert that the main goal associated to the task_2.2 and regarding the possibility to implement a control loop using an accelerometer for a satellite in L2 and study an appropriate control law in order to permit the right movements and coverage of all the uv plane, can be reached.

5.2.1 Acceleration due to the Gravity Gradients

Using the Eulero-Hill formulas it is possible to evaluate the differential gravity acceleration acting between two satellites orbiting in L2; acceleration that must be imparted by the orbital control on the satellites in order to maintain their distance fixed.

A reference having its origin in the center of rotation of two satellites, arranged as shown in figure_5.2-1, with the x axis oriented as the Earth-Orbit joining, the z axis normal to the ecliptic and y to complete the right-handed triad, it is in rotation with respect to an inertial reference frame, because it rotates at about the speed with which the trajectory of the point L2 completes a revolution around the Earth. The results indicated that, for two satellites

disposed on the plane with a phase-shift between them of 180 $degrees$, in free falling, the distance between them change in time, harmonically oscillating between 1000 and 2000 m, where 1000m is the initial position. To keep the satellite at the same distance, their orbit must therefore be controlled through an acceleration that is always of the same order of magnitude of the natural force, then about $10^{-10} \; m/s^2$ and at the orbital period.
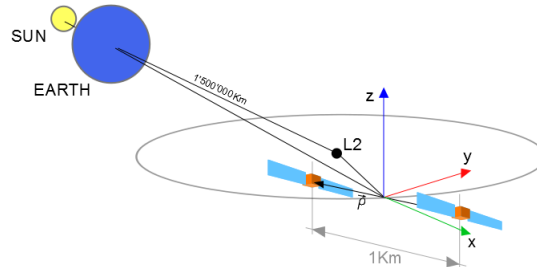
Figure_5.2.1-1 *Eulero reference frame.*

In the figure_5.2.1-2/3 are shown respectively: the relative distance between the two satellites not interconnected, the distances between the two satellites vs the rotation angle and the accelerations in the Euler reference frame in L2, due to the gravity gradient.
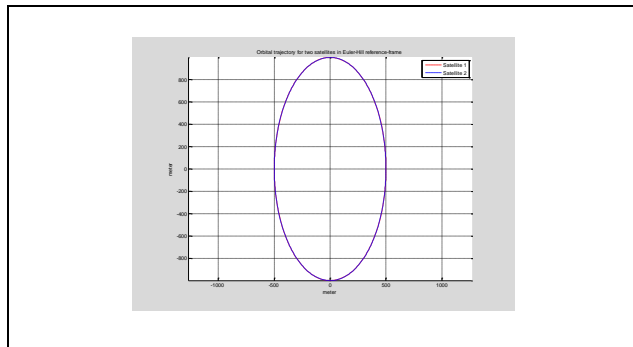
Figure_5.2.1-2 *Elliptical trajectory of two satellites out of phase by 180 ° in a Euler non-inertial reference frame.*	**Figure_5.2.1-3** *Relative distance between the two satellites not interconnected orbiting in L2.*
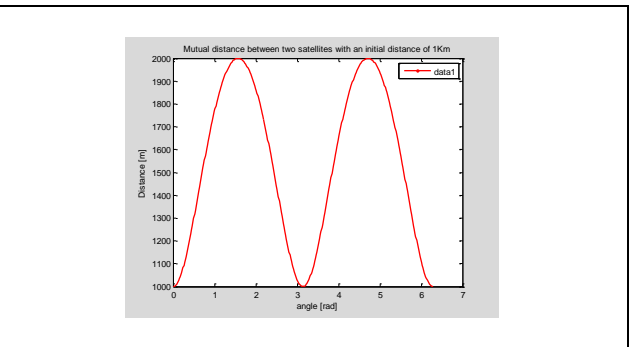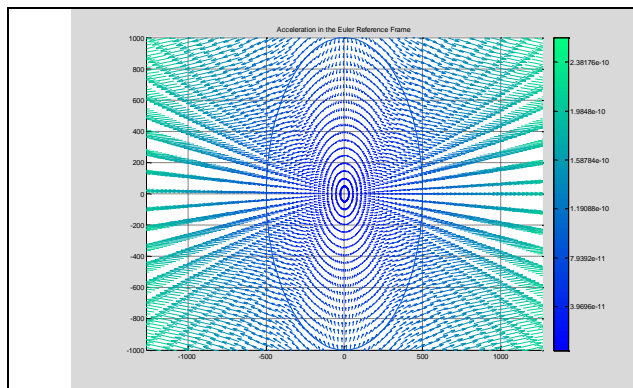
	Figure_5.2-4 *Accelerations in the Euler reference frame in L2, due to the gravity gradient.*

In this case the frequencies are due to the orbital periods around L2 and so at 365 days.
It is necessary to remark that the accelerations connected to the gravity gradient are at the level of $10^{-10} \; m/s^2$. In the following we will consider the accelerations acting on the

interferometer system during its rotation to acquire all the u, v points, it is clear that the acceleration due to the gravity gradients, will change in frequency but not in its amplitude.

We will go now to resume the obtained results for the evaluation of the accelerations acting on the interferometer and due to its dynamical motions, starting with the description of the system.

In Figure_5.2.1-5 is shown a FIR Interferometer telescope constituted by two telescope and a central hub connected with two booms while in the figure_5.2.1-6 is shown the same telescope with the indication of the observation plane, on which the dynamics of the interferometer is performed, clearly perpendicular to the ILS (Instrument Line of Sight), axis around which the interferometer rotates.
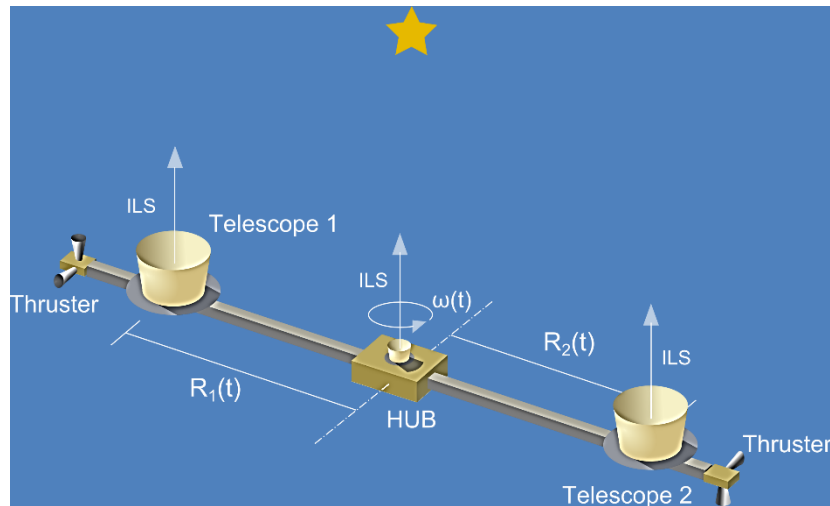
Figure_5.2.1-5 *FIR Interferometer telescope constituted by two telescope and a central hub connected with two booms.*
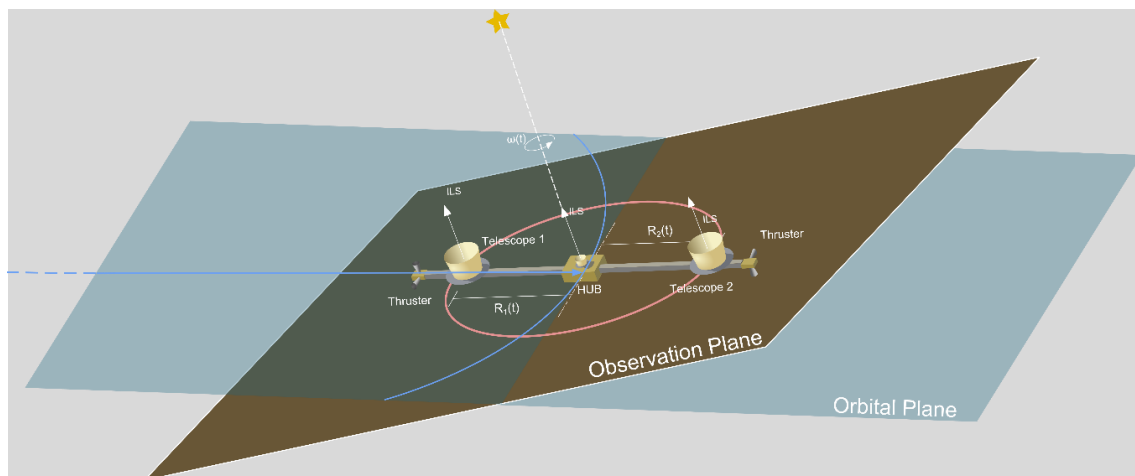
Figure_5.2.1-6 *FIR Interferometer telescope constituted by two telescope and a central hub connected with two booms, with the indication of the observation plane.*

For what we told before, it is clear that if we want to force a system of two satellites in L2 to follow a particular trajectory, in first approximation we can ignore the acceleration

necessary to compensate for the gravity gradient change and take into account only the accelerations necessary to give the desired dynamics to the satellites.

5.2.2 Acceleration due to the interferometer dynamics

In the following we will resume the results concerning the dynamics of the interferometer for the three following cases:

a) Changing the distance $R(t)$ between the two satellites following a spiral trajectory, without the use of thrusters.

b) Changing the distance $R(t)$ leaving the system to change in consequence of its angular velocity (to avoid consumption of propellant), but ensuring the coverage of the u, v plane with an adequate tangential velocity.

c) Changing the distance $R(t)$ with the introduction of a simultaneous momentum, to maintain the system on a spiral and conserving the appropriate tangential velocity.

Here the principal scope is to get information about the level of accelerations involved in the movements that the interferometer has to perform, to verify the capability of an accelerometer to detect them and permitting to implement a control loop or to give the possibility, taking them into account, to remove the perturbing effects.

5.2.2.1 *Interferometer dynamic in L2 – Spiral trajectory*

In the following are listed the formulas concerning a system of two satellites placed in L2 forced to describe a spiral in a plane x,y, in order to cover the complete uv plane.

$$x(t) = D\left(1 - \frac{t}{T}\right)\cos(\omega_T t) + \frac{D}{T\omega_T}\sin(\omega_T t)$$
$$y(t) = D\left(1 - \frac{t}{T}\right)\sin(\omega_T t)$$

$$\dot{x}(t) = -D\omega_T\left(1 - \frac{t}{T}\right)\sin(\omega_T t)$$
$$\dot{y}(t) = D\left(1 - \frac{t}{T}\right)\cos(\omega_T t) - \left(\frac{D}{T}\right)\sin(\omega_T t)$$

$$\ddot{x}(t) = -D\omega_T\left(1 - \frac{t}{T}\right)\sin(\omega_T t)$$
$$\ddot{y}(t) = D\left(1 - \frac{t}{T}\right)\cos(\omega_T t) - \left(\frac{D}{T}\right)\sin(\omega_T t)$$

Where T is the period of reference with which the trajectory is travelled, $\omega_T = \frac{2\pi}{T}$ is the angular velocity, while D is the initial distance of the satellite from the centre of the reference. If the characteristic time within which the trajectory is to be accomplished is of the order of 24 hours, the accelerations to impart to the satellite to control its dynamics is much bigger that the one necessary to keep it in the L2 orbit and so decoupled between them.

Trajectory, speed and acceleration in the x, y plane are described in figures_5.2.2.1-1. The main results is that the acceleration is of the order of $8 \cdot 10^{-4} \, m/s^2$, several orders of magnitude greater than the one acting on them due to the gravitation in L2.
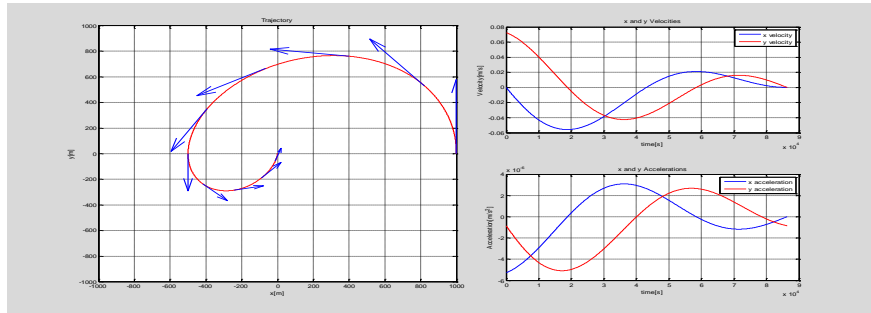
Figure_5.2.2.1-1 *Trajectory speed and acceleration for the spiral to be followed by the satellite*

5.2.2.2 *Change of the ITD without use of thrusters.*

In following the analysis concerning the maneuvers of the interferometer is summarized, following different laws for the ITD change, without the use of thrusters to keep the tangential velocity constant and so to save propellant. The study is finalized to find the optimal law that gives the better coverage of the u, v plane and with the tangential velocity that remains the closest possible to the desired one. For the scopes of this document, we focus on the value of the level of accelerations at which the telescope is exposed and at their frequency range, that become a requirement for the accelerometer.

The analysis refers to a simplified system constituted by two equal ideal masses representing the telescopes that can move in the observation plane linked together by the booms. The central Hub has an internal motor permitting to change the ITD $R_1(t)$ and $R_2(t)$. As the system will be a sort of big gyroscope it will conserve its angular momentum, while the angular velocity and the tangential velocity will increase and decrease with a fixed law, function of the booms length vs time.

Between the studied laws for the ITD change, the cubic law is the one that better fit the need to have the most regular steps length during the rotation. But the square offers a good coverage.

In the following figure the radial displacements, the velocity and the acceleration of one of the two telescopes vs time are shown for these two laws respectively.
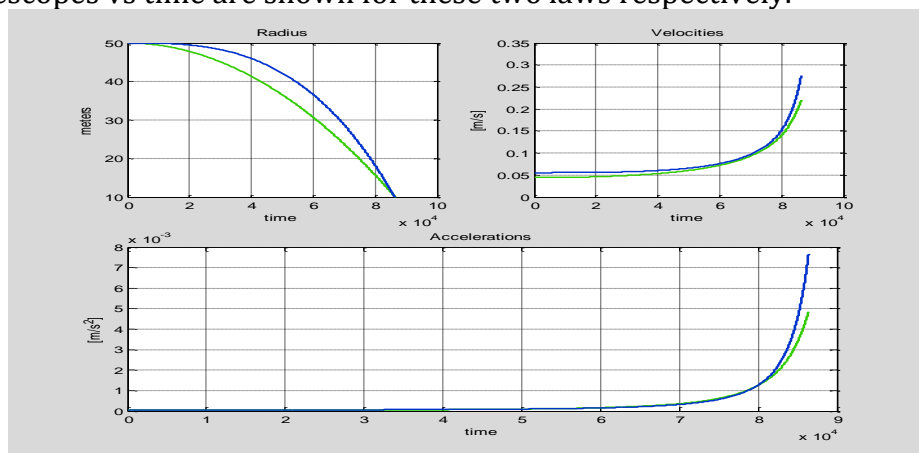
Figure_5.2.2.2-1 *Velocities and Centrifugal accelerations for the cubic and square law.*

For the scope of the definitions of the characteristics of the accelerometer the message to retain is that the accelerations do not exceed $8 \cdot 10^{-3} \ ^m/_{s^2}$, with a temporal variation of $24h$; value well inside the characteristics that can be met with the proposed accelerometer.

5.2.2.3 *Change of the ITD with use of thrusters.*
In the following figure_5.2.2.3-1/2 are reported the spiral trajectory for a thrusters assisted maneuver, and the necessary torque to obtain it.

| **Figure_5.2.2.3-1***Spiral trajectory for a thrusters assisted maneuver*	**Figure_5.2.2.3-2** *Spiral trajectory for a thrusters assisted maneuvers, torque vs time*
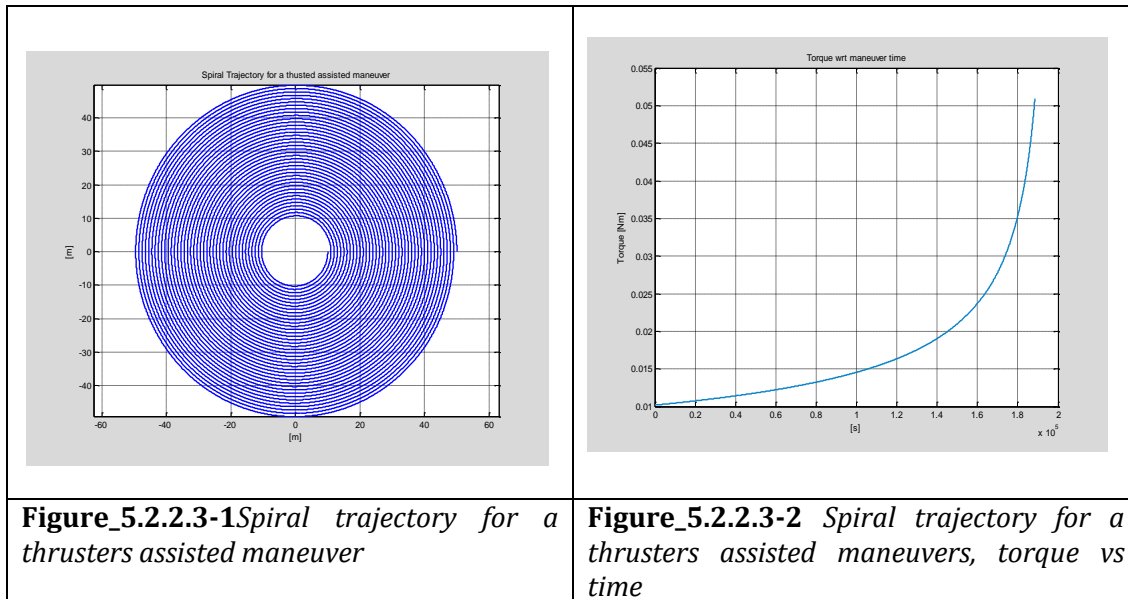
5.3 NOISE ANALYSIS
In this section will be considered the possible causes of perturbations of the observations performed with a FIR space interferometer. In particular the noise perturbing the single spectroscopic measurements of a (u, v) point will be considered, and due to the noise presents on every element of the interferometer (each telescope, hub combiner) and to the differential noise due to the vibration of the whole telescope structure.
The noise concerning the spectroscopic measurements here analysed is strictly connected to the OPD errors (see **Error! Reference source not found.**), or "PISTON effect" considered in the SPIRIT study. This effect, together with the pointing and WFD errors (see **Error! Reference source not found.**), represents the major sources of noise, determining the loss of visibility and spectral and imaging fidelity. Hereafter we analyse the direct effect of these disturbances, acting as jitter during the acquisition of the spectrographic signal as function of the positions of the sled of the OPD.

5.3.1 Analysis of noise relative to the acquisition of a single point of the plane u, v (spectroscopic measurement)
To the analysis of the noise relative to the single point of the (u, v) plane it is necessary to take into account that, as indicated in the ESA CDF FIRI study, the single spectroscopic measurement for a point in the u, v plane is performed in a time of order of about $24 \ sec$, for a total number of points in the u, v plane equal to about 1370. Similar numbers are

found for SPIRIT. For each elementary measure the base configuration to consider is as shown in the following figure:
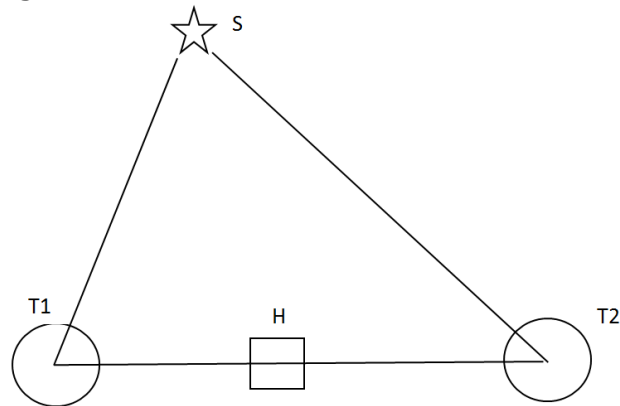
Figure_1. Base interferometer configuration for the measurements of a single u, v point.

where the indicated points are:
S: Position of the observed sky area,
T1: First telescope.
T2: Second telescope
H: Interferometer Hub (Point where the recombination for the execution of interferometry takes place)

The whole system is referred to an inertial reference frame and we can think that the plane defined by the triangle is coplanar with the xy plane of the inertial reference. In this configuration are to be found all the causes of a possible change in the two paths listed below:

$$S - T1 - H \ and \ S - T2 - H,$$

and then the variations of the lengths: $S - T1, \ S - T2, \ T1 - H \ and \ T2 - H$.
These lengths can vary both due to the overall movement of the support structure of the two telescopes and the central hub, both due to the noise present on each single element.
We consider now all types of noise that can act on the single elements (T1, T2, H) in an independent manner and such as to give contributions not correlated with those of the other two units. The types of noise can be of two types:
• Stochastic Noise
• Deterministic Noise.
The first type of noise is associated with vibrations that extend in a certain band of frequencies without showing particular peaks, for which the integration time, determines a narrowing of the band on which this noise is integrated with a consequent decrease of its *rms* values. The noises of this type, associated with different sources are *added quadratically*.
The second type of noise is associated with vibrations and signals present at precise frequencies, for which the integration produces a narrowing of the frequency band in which the noise is integrated, but if this band includes the frequency of the deterministic noise, the latter is not reduced. In this case the noises are *added linearly*.

For both types of noise it is necessary to assess their effect on the interferometric measurement and thus give the requirements for the maximum acceptable noise or determine them with precision and remove their effect in the process of data analysis.

Only for the noise of the deterministic type, one can think to measure them with a suitable system, for example with an accelerometer and use this information for controlling the actuators that cancel the effect. Since the noise is added to the signal, it is necessary to actuate the feedback only at frequencies in which the noise is present, while the system should be free at frequencies in which the signal acts. In this case all the differential movements of the interferometer elements can be considered as noise.

Both types of noise, stochastic and deterministic, act to change the difference of the two optical paths, producing a variation of the interference of the two light beams at the detector, with an intensity that varies with the period of the wavelengths present in the beam, we would refer to this as the *jitter effect*.

Recalling that the spectroscopic scanning is obtained with the movement of the slide of the OPD and taking into account that the minimum wavelength to be detected is equal to $\lambda_{min} = 25 \, \mu m$, it is clear that the effects of noise, translated into displacement, must be much smaller than this minimum wavelength.

One may think that the displacements of the OPD slide determine a linear variation of the optical path in a ratio one to one, or through a certain multiplication factor (multiple reflections), in any case, the time required to produce this variation determines, in its inverse, the frequency at which the intensity modulation is seen.

$$I = I(\lambda) = I(v \cdot t) = I(v_s/f))$$

The criteria for choosing the sled velocity are:

1) Minimization of the acquisition time of the single point of the u, v plane
2) Transferring the Signal to a frequency range where vibrational noise is low.

In the hypothesis of a movement of the slide at constant speed v, the peaks of maximum intensity will occur at times equal to $t_n = \frac{\lambda_n}{v}$ and then at frequencies $f_n = \frac{v}{\lambda_n}$; the highest frequency will correspond to the minimum wavelength, assumed to be $\lambda_{min} = 25 \, \mu m$. It is therefore important to make a frequency analysis of the noise present on the satellite and then choose a suitable speed of the slide such as to send the signals to be detected, in a frequency band in which the vibrational noise level is minimal.

The problem is thus to acquire a signal that varies with λ, as function of time through the speed of the sled. The presence of noise causes acquisitions not to be made at well-determined positions as expected from the constant speed of the slide but in positions determined by this velocity plus a noise contribution. In other words the problem is thus to acquire a signal as a function of λ where λ does not vary linearly but has components due to noise. It follows that:

$$I = I(\lambda) = I(v \cdot t + \lambda_r)$$

In case the considered spectral band of the FIR interferometer is as below:

$$[\lambda_{min}, \lambda_{max}] = [25 \, \mu m, 500 \mu m]$$

and if it is decided that the max distance, related to the largest wavelength is performed by the ODL in ~26 s, it follows a speed equal to: $V_S = 500 \cdot \frac{10^{-6}}{26} = 1.9 \cdot 10^{-5} m/s$. The consequent frequency band in which the signals are translated is:

$$[f_{max}, f_{min}] = \left[\frac{V_s}{\lambda_{min}}, V_s/\lambda_{max}\right] = [6.4 \cdot 10^{-1} Hz, 3.8 \cdot 10^{-2} Hz]$$

Here below a simulation is reported concerning the acquisition of an interferometric signal $I = I(\lambda)$, in the presence of the indicated jitter noise. In the first analysis we considered the acquisition of an interferometric signal varying sinusoidally with respect to λ, acquired through a constant speed movement of the OPD, with added white noise.

$$I(\lambda) = I_0 \cdot \cos\left(2 \cdot \pi/L_s \cdot (V_0 \cdot t + x_b)\right)$$

It is necessary to note that this case is not corresponding to a real case, because usually the Brownian noise is in terms of force or acceleration and the corresponding displacements is obtained integrating it and so decreasing with 40dB per decade with respect to the accelerations, nevertheless the example give good indications of the limitations that the jitter effects introduce in the spectroscopic measurements.

In **Error! Reference source not found.** the results of this simulation are reported using the parameters reported in **Error! Reference source not found.**.

Table 5.3.1-1. *Parameter used for the performed simulation.*

I_0	10^{-6}
L_0	$500\ \mu m$
t_0	$26\ s$
$V_0 = L_0/t_0$	$1.9 \cdot 10^{-5}\ m/s$
L_s	$1/5 \cdot 10^4 = 20 \cdot 10^{-6}$
x_b	$10^{-6} \frac{m}{\sqrt{Hz}} - 10^{-11}\ m/\sqrt{Hz}$ -
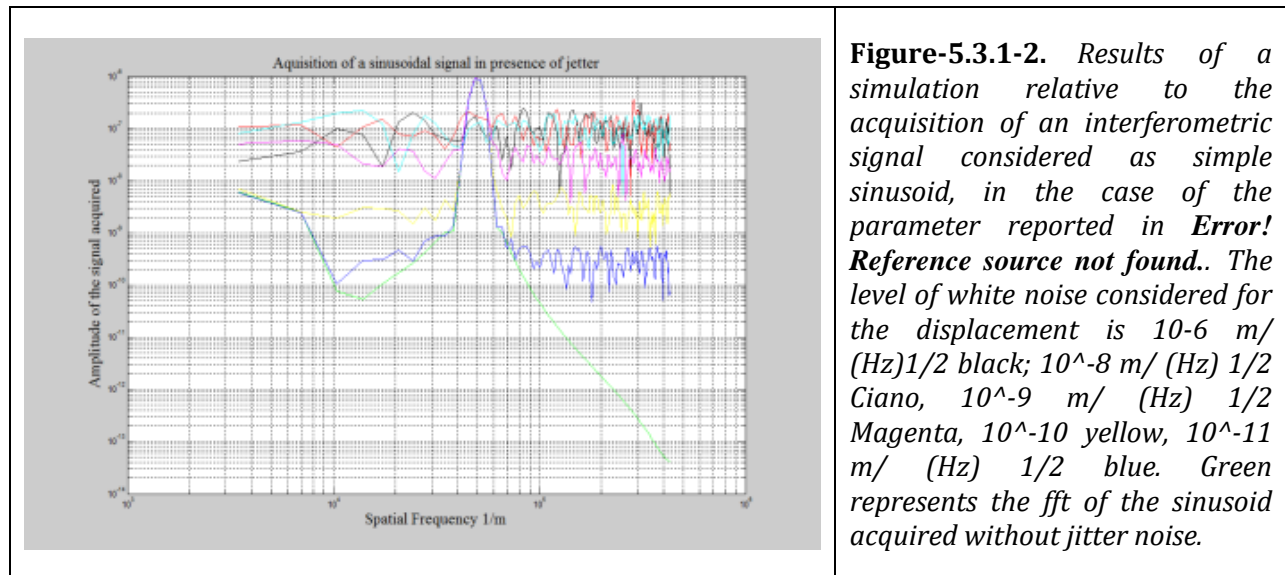
Figure-5.3.1-2. *Results of a simulation relative to the acquisition of an interferometric signal considered as simple sinusoid, in the case of the parameter reported in **Error! Reference source not found.**. The level of white noise considered for the displacement is 10-6 m/ (Hz)1/2 black; 10^-8 m/ (Hz) 1/2 Ciano, 10^-9 m/ (Hz) 1/2 Magenta, 10^-10 yellow, 10^-11 m/ (Hz) 1/2 blue. Green represents the fft of the sinusoid acquired without jitter noise.*

In **Error! Reference source not found.** the analogue simulation is reported obtained changing only the value of the amplitude of signal to be acquired, now equal to 10^{-4} instead of 10^{-6}. It is possible to see that there is no change in terms of ratio between signals to noise.
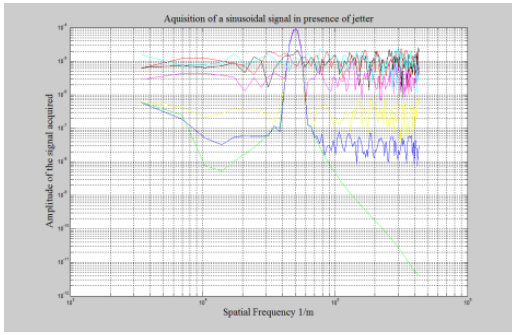
Figure-5.3.1-3. *Results of a simulation relative to the acquisition of an interferometric signal considered as simple sinusoid, in the case of the parameter reported in **Error! Reference source not found.** except for the value of the amplitude of the signal to be acquired, now equal to 10^{-4}. The level of white noise considered for the displacement is as in **Error! Reference source not found.**.*

It is possible to deduce that the sinusoidal signal can be detected only if the white noise in displacement is under $10^{-8} \, m/(Hz)^{1/2}$, this to be compared with the spatial frequency to be detected $f_s = \frac{1}{5 \cdot 10^4}$, corresponding to $\lambda_s = 20 \, \mu m$.

If we are in the presence of a deterministic noise at a certain frequency, always in the case of the above example, the amplitude of the signal to be detected would be given by the relation:

$$I = I_0 \cdot cos\left(\frac{2 \cdot \pi}{\lambda_0}(v \cdot t + v_0 \cdot t_0 \cdot cos(\omega_0 t))\right)$$

5.3.2 Example of noise presents on a satellite.

Here an example of vibrational noise that can be present on a satellite is described. The information corresponds to that of the Radio Science Experiments on the ESA Cornerstone mission to Mercury, BepiColombo.

In **Error! Reference source not found.** the requirements for the deterministic vibrational noise inside the frequency measurements band on board the MPO (Mercury Planetary Orbiter) are shown, one of the two satellite considered for the BepiColombo Mission for the exploration of Mercury and to test the General Relativity; requirements that hold in the context of the RSE (Radio Science Experiments). The corresponding displacements values can be found using the relation: $x = a/(2*pi*f)^2$. In **Error! Reference source not found.** we show the requirements for the stochastic vibrational noise inside the frequency measurements band.

Table_5.3.2-1. *Vibrational noise inside the frequency measurements band on board the MPO (Mercury Planetary Orbiter) BepiColombo Mission for the RSE (Radio Science Experiments).*

Frequency Hz	$3 \cdot 10^{-5}$	$10^{-4} - 10^{-3}$	10^{-1}
Acceleration values (m/s^2)	$3 \cdot 10^{-9}$	$10^{-9} - 10^{-9}$	10^{-8}
Corresponding displacements m	$8.4 \cdot 10^{-2}$	$2.5 \cdot 10^{-3} - 2.5 \cdot 10^{-5}$	$2.5 \cdot 10^{-8}$

Table_5.3.2-2. *Stochastic vibrational noise inside the frequency measurements band on board the MPO (Mercury Planetary Orbiter) BepiColombo Mission for the RSE (Radio Science Experiments)*

Frequency Hz		$3 \cdot 10^{-5}$	$10^{-4} - 10^{-3}$	10^{-1}
Acceleration values	$\frac{m}{s^2}/\sqrt{Hz}$	$3 \cdot 10^{-9}$	$10^{-9} - 10^{-9}$	10^{-8}
Corresponding displacements $m/\sqrt{Hz}$		$8.4 \cdot 10^{-2}$	$2.5 \cdot 10^{-3} - 2.5 \cdot 10^{-5}$	$2.5 \cdot 10^{-8}$

In **Error! Reference source not found.** the requirements of **Error! Reference source not found.** are illustrated, showing that the acceleration values in black and displacements in red, and in **Error! Reference source not found.** is shown the requirements for the microvibration deterministic noise outside the frequency measurements band on board the MPO (Mercury Planetary Orbiter).
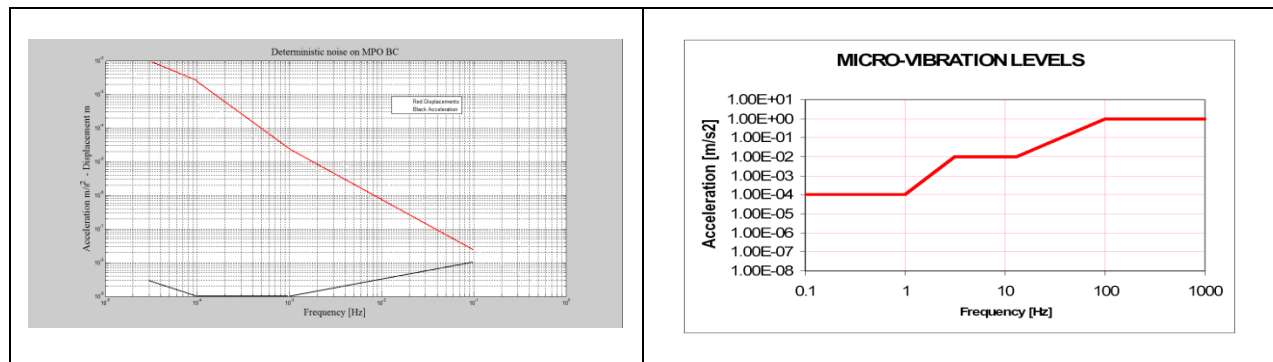
Figure_5.3.2-1. *Deterministic vibrational noise inside the frequency measurements band on board the MPO (Mercury Planetary Orbiter) BepiColombo Mission for the RSE (Radio Science Experiments).*

Figure_5.3.2-2. *Level of the micro-vibration deterministic noise outside the frequency measurements band on board the MPO (Mercury Planetary Orbiter), takes as requirement.*

In **Error! Reference source not found.** and **Error! Reference source not found.** the noise presents on the MPO BepiColombo due to the motions of the solar array and the HGA (High Gain Antenna) respectively are shown, as assessed by ASTRIUM (ASTRIUM ASSESSMENT OF THE MICROVIBRATION BUDGET FOR BepiColombo).
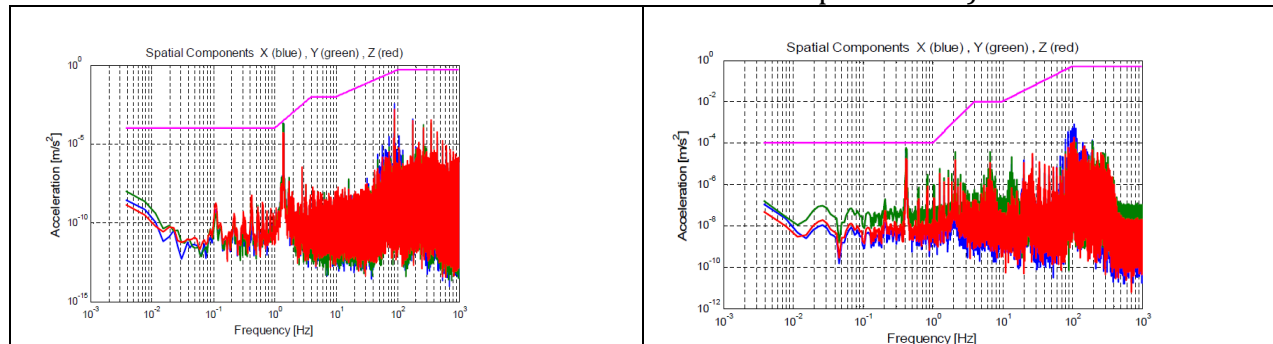
Figure_5.3.2-3. *Noise presents on the MPO BepiColombo due to the motions of the solar array as assessed by ASTRIUM (ASTRIUM*

Figure_5.3.2-4. *Noise presents on the MPO BepiColombo due to the motions of the HGA (High Gain Antenna) as assessed by ASTRIUM*

Error! Reference source not found. shows the micro-vibration noise on board the MPO outside the frequency band in x and z direction due to the reactions wheels, compared with the requirements (solid line). The translation between accelerations and displacements can be performed as previous indicated (double integration)
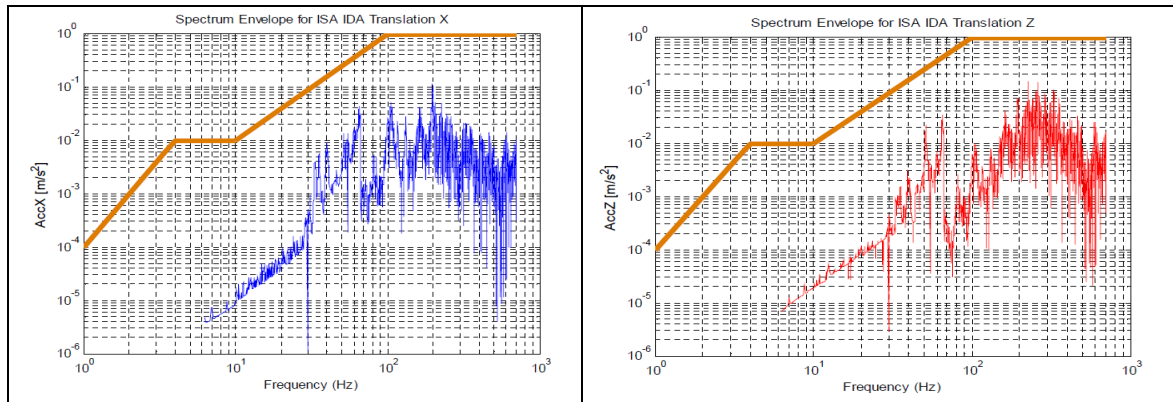
Figure_5.3.2-5 *Micro-vibration noise on board the MPO outside the frequency band in x and z direction due to the reactions Wheels, compared with the requirements (solid line). The translation between accelerations and displacements can be performed as previous indicated (double integration).*

In **Error! Reference source not found.**5.3.2-6 the spectral density is shown of the solar radiation pressure for the BepiColombo MPO in orbit around Mercury, very close to the Sun. The solar radiation pressure at the orbital period of the MPO is $10^{-6}\,m/s^2$, corresponding to a displacement equal to 1.6 m at the orbital period of 2.3h.
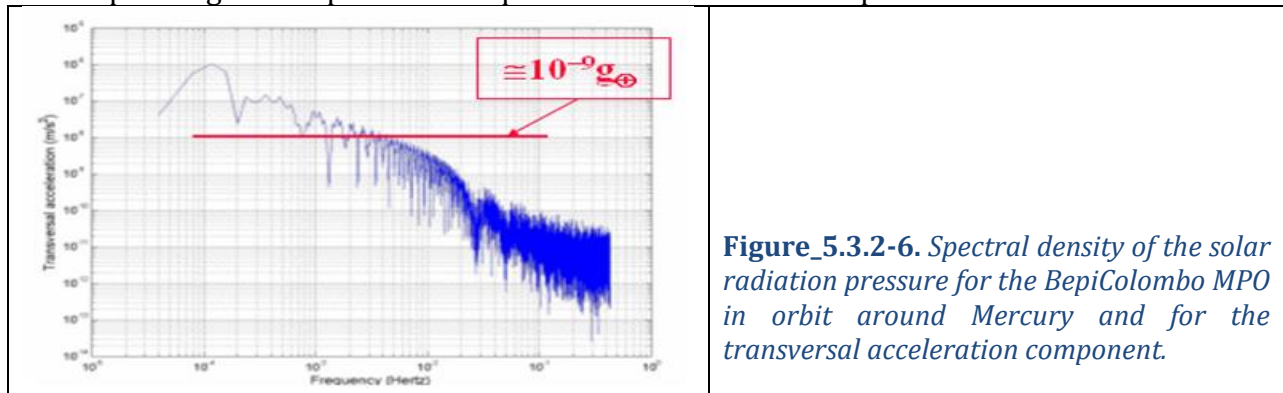
Figure_5.3.2-6. *Spectral density of the solar radiation pressure for the BepiColombo MPO in orbit around Mercury and for the transversal acceleration component.*

The MPO IMU mission uses an accelerometer to measure the on-board accelerations. The accelerometer measurements error is connected to its position vs the MPO COM, position that can be defined with a vector indicating the distance between the instantaneous MPO center of mass (CoM) and that of the accelerometer CoM:

$$\vec{R} = \vec{R}_0 + \Delta\vec{R}_0 + \vec{R}_t(t) + \Delta\vec{R}_t(t)$$,

given in terms of time-independent and time-dependent parts (known parts and error parts). In **Error! Reference source not found.** is reported the angular rate and angular acceleration noise requirements for an accelerometer used for the MPO IMU navigation in

case it is installed with its CoG coincident with the MPO COM (case A) and at a distance of 20cm (case B).

Table_5.3.2-3. *Accelerometer requirements on the angular rate and angular acceleration*

	Case A)	Case B)
$\delta\omega$	$1.34 \cdot 10^{-5}$ $rad/s/\sqrt{Hz}$	$0.54 \cdot 10^{-5}$ $rad/s/\sqrt{Hz}$
$\delta\dot{\omega}$	$1.76 \cdot 10^{-8}$ $rad/s^2/\sqrt{Hz}$	$0.56 \cdot 10^{-8}$ $rad/s^2/\sqrt{Hz}$

In the table_5.3.2-4 the MPO temperature variations at the orbital period are reported, sidereal period, and that due to random fluctuations. It is clear that the temperature variation will be much less for the interferometer in L2, nevertheless considering the big dimension of the satellite their influence due to thermal contraction will be high especially at the interferometer angular rate.

Table_5.3.2-4. *MPO temperature variations at the orbital period, sidereal period, and random.*

Frequency	T (°C)
Mercury revolution period	25 peak-peak
MPO orbital period	4 °C peak-peak
Random noise	$4\ °C/\sqrt{Hz}$

At the end of this section we like to remember that the FIRI frequency band, in which we will see the signal, is:

Band: $[f_{max}\ f_{min}] = [V_s/\lambda_{min}\ V_s/\lambda_{max}] = [6.4 \cdot 10^{-1}\text{Hz}\quad 3.8 \cdot 10^{-2}\text{Hz}]$.

Assuming that the optical path delay slide needed for a R~3000 we obtain, $MPD_{max} = 6.5\ cm = 0.065\ \cdot 10^{-3}\ m$, in a time of $26\ s$, it follows that its speed is equal to:

$$v = \frac{6.5 \cdot 10^{-2}}{26} = 2.5 \cdot 10^{-3}\ m/s$$

At this speed correspond a $f_{min}\ ed\ f_{max}$ of the signal to be detected respectively equal to

$$f_{min} = \frac{v}{\lambda_{max}} = \frac{2.5 \cdot 10^{-3}}{500 \cdot 10^{-6}} = 5\ Hz$$

$$f_{max} = \frac{v}{\lambda_{min}} = \frac{2.5 \cdot 10^{-3}}{20 \cdot 10^{-6}} = 125\ Hz$$

It is difficult to work at these frequencies due to the high value of the noise present on the satellite. In order to reduce the frequency of the signal to be detected, it necessary to work with a speed of the slide a factor of 10 or 100 lower.

5.3.3 Analysis of noise relative to the acquisition of all points in the u, v plane (spatial measurement)

The reconstruction of the mapping of the sky area inside the FOV is made by means of inverse Fourier transform of all spatial frequencies with their proper amplitudes, contained in the u, v plane, measured with the interferometer for all appropriate radial and angular positions of the two telescopes. In the case of FIRI the u, v plane can be decomposed of 1373 distinct points (that fill it densely) and as mentioned earlier each point is observed by the appropriate spectroscopic scanning for a time of ~26 sec and then proceeding to the next measurement by moving the two telescopes (in radial and angular manner) with respect to the line joining the HUB with the center of the FOV.

But, in every case the angular resolution is determined as function of wavelength λ and baseline B by the relation $\alpha = \frac{\lambda}{2B}$. At the maximum baseline observation, every point is acquired during a displacement of 1m with a radius of rotation equal to 50m, and so the average angle associated to this point and related to the requirement precision in angle is about $\frac{1}{50} rad$ which is not very stringent.

In the following the list of the main causes of noise to be considered for the evaluation of the deterministic and stochastic noises acting on the interferometer are reported; the list holds for the noise in the whole structure of the interferometer as well as on each of its elements (hub and telescope)

List of the deterministic noise effects
1) Inertial accelerations ω, $\dot{\omega}$
2) Attitude Control
3) Gravity Gradient
4) Vibrational noise due to the AOCS
5) Vibrational noise connected to the satellite structure
6) Thermal noise
   - Solar Radiation pressure (Satellite rotation)
   - Noise due to the power dissipation of the instruments presents on the satellite (principally On Off of the instruments)
7) Noise due to the appendices movements.
   - Solar pannel
   - RW vibrations (desaturation, maneuvers)
   - Antenna movements.
8) Sloshing fuel
9) Out of band Microvibration (High frequency)

List of the stochastic noise effects
1) Inertial accelerations $\delta\omega$, $\delta\dot{\omega}, R, \Delta R$
2) Gravity Gradient $R, \Delta R$
3) Vibrational noise due to the AOCS
4) Vibrational noise connected to the satellite structure
5) Thermal noise
   - Solar Radiation pressure (Satellite rotation)

- Noise due to the power dissipation of the instruments presents on the satellite (principally On Off of the instruments)
6) Noise due to the appendices movements.
  - Solar pannel
  - RW vibrations (desaturation, maneuvers)
  - Antenna mouvements.
10) Sloshing fuel

5.4   MODAL ANALYSIS SIMULATION FOR A CONNECTED INTERFEROMETER

In this section we present a modal analysis concerning an interferometer constituted of two telescope connected to a central hub by means of two mechanical booms. In **Error! Reference source not found.** are reported the main parameter used in the simulation.

Table_5.4-1. *List of the main parameter used in the modal analysis*

	Value
Satellites Mass (kg)	2 X 850
Central Hub Mass (Kg)	313
Booms Mass (Kg)	2 X 421
Booms length (m)	2x50

Error! Reference source not found. shows the assembly of the interferometer with the two telescope and the central hub used in the following simulations, and **Error! Reference source not found.** shows the individual parts, telescope, boom, and hub. Note that in this first analysis the values for the components used in the simulation are taken from the FIRI study, in particular for what concern the structure of the boom.
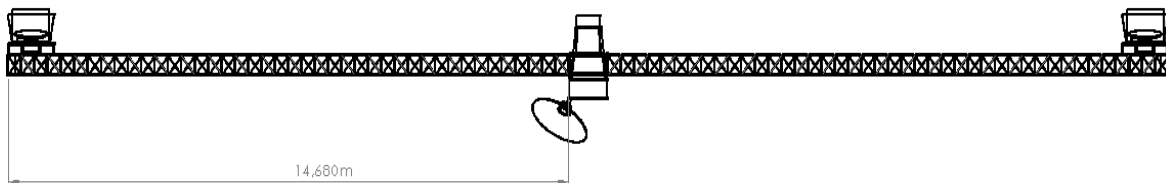
Figure_5.4-1. *Assembly of the interferometer with the two telescope and the central hub.*
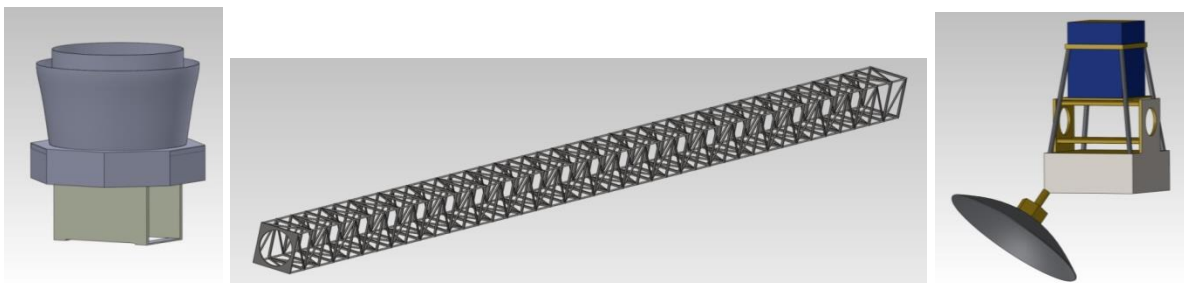
Figure_5.4-2. *Model design of telescope (left), boom (middle), and hub (right).*

Error! Reference source not found._5.4-2 reports the frequencies obtained with the modal analysis for the first four normal modes, illustrated in **Error! Reference source not found.**_5.4-3.

Table_5.4-2. *First fourth frequencies obtained with the modal analysis*

Normal Mode	Value (Hz)
First	0,84
Second	0,098
Third	3,39
Fourth	3,5
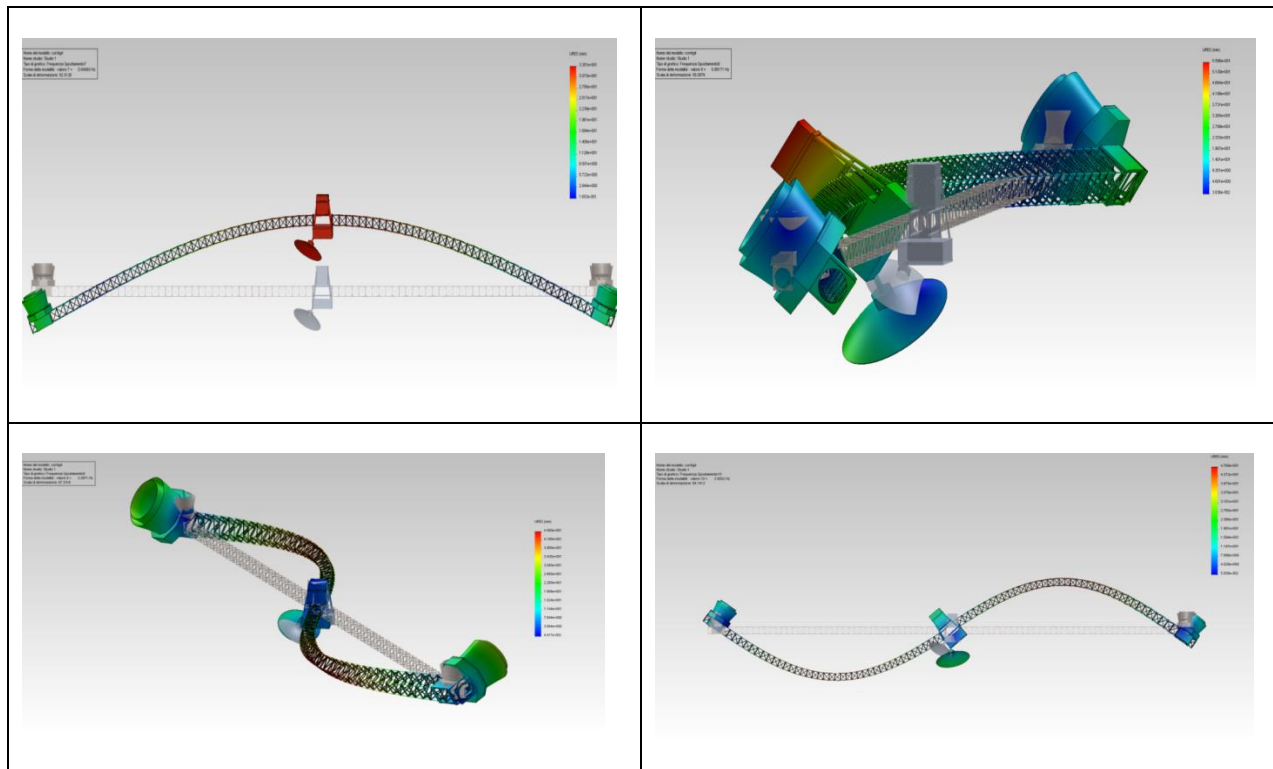
Figure_5.4-3. *From top to bottom, visualization of the first four normal mode of the FIRI structure.*

The analysis presented is of fundamental importance because it allows to determine the indicative values of the frequencies of the structure and in particular the shape of the vibrational mode of the system, that attain to the metrological problem in terms of precision in the distances between each telescope and the central Hub, but also in the pointing precision of each telescope to the source. In particular the indicated normal modes are excited by transient effects induced by the manoeuvres of the telescope (retargeting and change of the ITD), and it's of fundamental importance to evaluate their values and to introduce dissipaters able to reduce their relative mechanical values so to come back after the induced transient to a low level of vibration. In the following section a dynamical analysis will be presented concerning the first normal mode of the interferometer, here introduced.

5.5 DYNAMIC ANALYSIS IN CLOSED LOOP OPERATION

In the following section the dynamic analysis of the interferometer using thrusters to maintain constant angular velocity during the entire u-v plane scan is reported.

The study starts with a dynamical analysis performed using the *Simmechanics* tool of MATLAB, this analysis is a continuation of the modal analysis performed in the previous section and gives the ideas on the dynamic vibration of the interferometer and on the possible control loop to be implemented in order to control its dynamics during the observation.

The tool permits to simulate the dynamics of the bodies through the definitions of the masses, momentum of inertia, their positions, the mechanical constraints (springs), forces and momentum acting on them. The analysis taks as reference the structure shown in **Error! Reference source not found.**_5.4-1. In **Error! Reference source not found.**_5.5-1/2 we show the implemented scheme for the performed dynamic analysis.
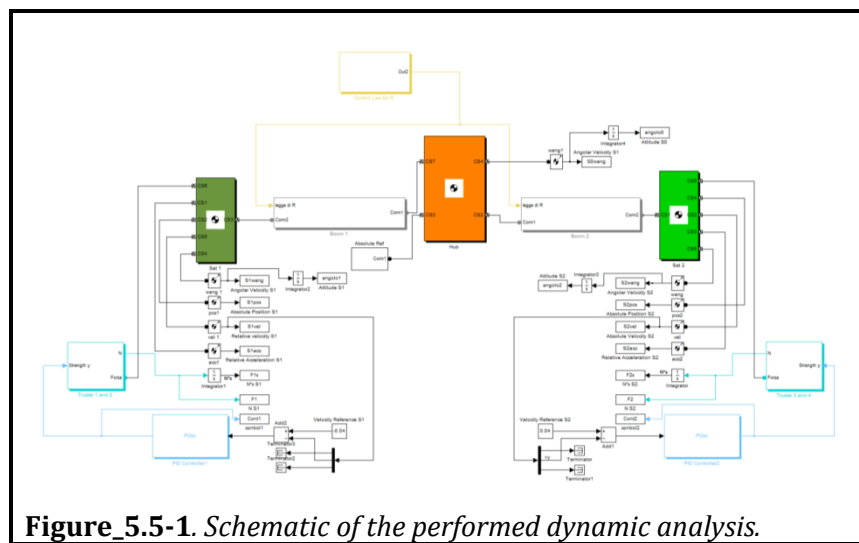
Figure_5.5-1. *Schematic of the performed dynamic analysis.*

The meaning of the main elements reported in the Figure_5.5-1 used for the simulation are reported in the following list:

a) Green boxes – Satellites with masses equal to 1000Kg

b) Orange box – Hub with mass equal to 320Kg

c) Two rigid elements with zero mass, connecting the central Hub to the telescopes.

d) Pivot point on the three masses. The introduced elastic torsional spring with the introduced dissipations are defined in order to determinate an oscillation frequency equal to $\omega_{int\_1} = 0.2Hz$ and a quality factor $Q_1 = 100$, as indicated in the FIRI study where its values range between 20 and 200.

e) Yellow box – Radial actuator with possibility to contain the law for the ITD (Inter Telescope Distance) change: 1m steps, spiral ecc.

f) Blue boxes – Two actuators (thrusters) and two PID (Proportional Integral and Derivative) for the control loop actuation.

g) Comparing elements to determinate the desired tangential velocity, taken equal to $0,04 \ m/s^2$.

h) All the analysis is performed in a two dimensional case (on the rotational plane)

The indicated parameters are summarized in **Error! Reference source not found.**.
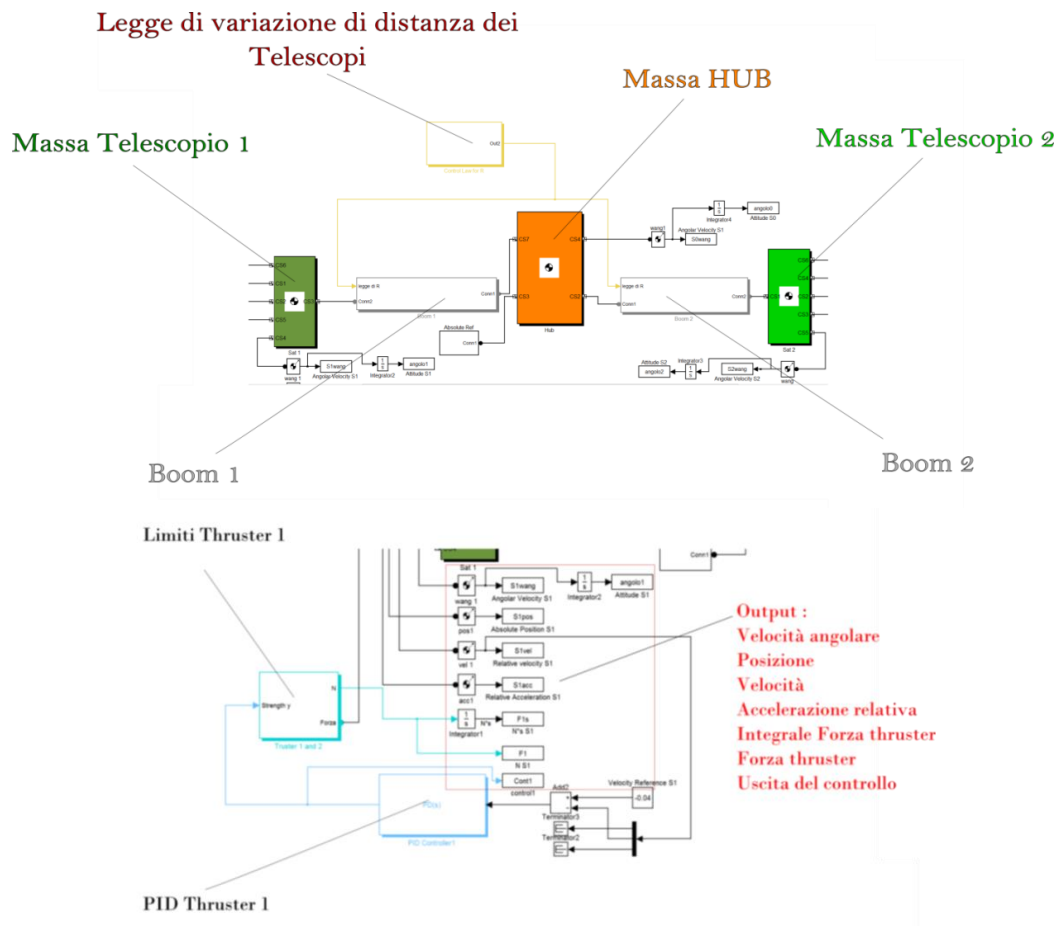
Figure_5.5-2. *Extracts of **Error! Reference source not found.** naming the main elements used for the simulation.*

Table_5.5-1. *List of the main parameters and condition used in the dynamic analysis*

	Value
Satellites Mass (kg)	2 X 1000
Central Hub Mass (Kg)	320
Booms Mass (Kg)	2 X 0
Booms length (m)	2X50

Error! Reference source not found. 5.5-3 reports the analog analysis performed for FIRI, with the evidence of the dissipation factor.
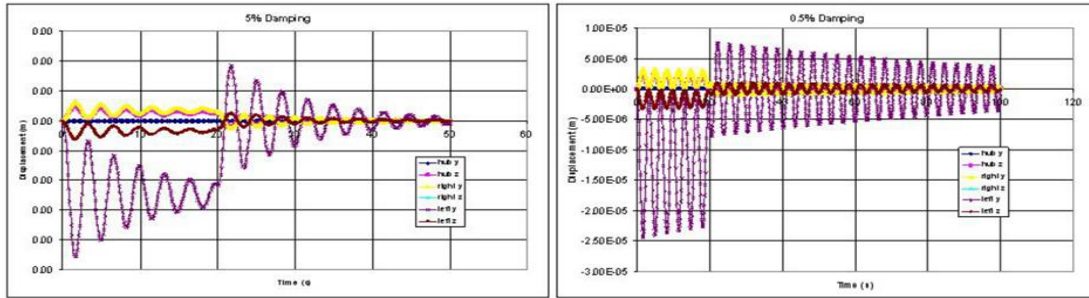
Figure_5.5-3. *Analysis performed for FIRI, with the evidence of the dissipation factor for the transient response of the telescope deceleration for 5% and 0,5% of critical damping.*

In the following the results of the performed analysis are shown. The two telescopes are initially positioned at $50m$ away from the HUB, the system will be posed in rotation with a tangential velocity equal to $v_T = \omega \cdot \frac{ITD}{2} = 0{,}04 \; m/s^2$, in this case, with $ITD = 100m$, the interferometer rotates at an angular velocity equal to $\omega = 8 \cdot 10^{-4} \; rad/s$; after a rotation of $180°$ the ITD will be reduced of $1m$ applying to the telescope a radial acceleration of sinusoidal shape for a time of $20s$. This radial acceleration besides the reduction of the ITD, produces also a transient in the interferometer that will be damped with a time constant equal to $\tau = Q_1/\omega_{int\_1}$. Remembering that ω_{int_1} is the angular velocity of the first interferometer normal mode, after every $180°$ of rotation the procedure is repeated.

When the ITD is changed, due to the momentum conservation law, the angular velocity increases. The thrusters can act to keep it at the assigned value by means of a control loop so that the tangential velocity will remain at a constant value equal to $0.04m/s$. We assume the two thrusters are able to give a force equal to $\mp 2.5 \; 10^{-2}N$ with the loop gain fixed at 1000. The control system and the kind of thrusters determine the time and modality of the control.

5.5.1 Trajectory description

In **Error! Reference source not found.**_5.5.1-1 the distance between one telescope and the HUB as function of time is shown during the whole procedure that brings the two telescope to a $ITD = 24m$.
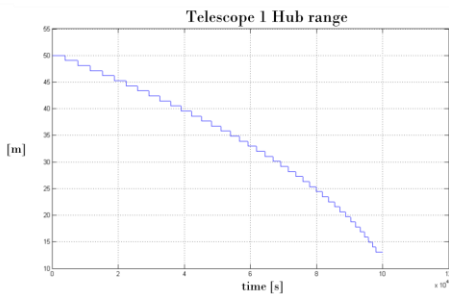
Figure_5.5.1-1. *Distance between one telescope ad the HUB vs the time, during the whole procedure that brings the two telescopes to $ITD=24m$.*

In figure_5.5.1-2 the position of the telescopes is shown as they rotate around the ILS in an inertial reference frame and in the plane perpendicular to the ILS, describing their trajectories during the whole procedure that brings the two telescope to $ITD = 24m$.
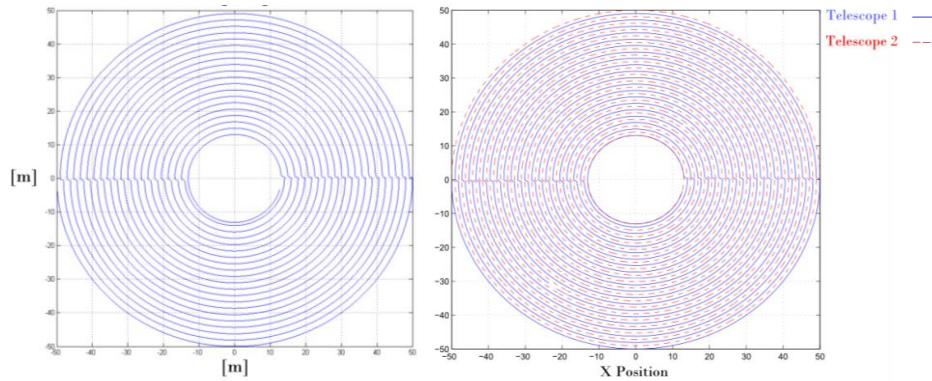
Figure_5.5.1-2. Position of Telescope 1 (left) and both telescopes (right) that rotate around the ILS in an inertial reference frame and in the plane perpendicular to the ILS, during the procedure to acquire the whole u, v plane.

Concentrating on the transient movements during the 1-m change of radial distance at each 180 degree position, **Error! Reference source not found.** 5.5.1-3 shows the trajectory of one telescope in an inertial reference frame and in the plane perpendicular to the ILS during this phase change. **Error! Reference source not found.** shows tangential velocity during this phase change, coming back to the assigned velocity of 0,04 m/s^2 controlled by the control loop. **Error! Reference source not found.** 5.5.1-4 shows the tangential velocity during the entire radial scan.

Error! Reference source not found. 5.5.1-5 shows the radial acceleration needed for one telescope to come back to the assigned velocity of 0,04 m/s^2 controlled by the control loop, and **Error! Reference source not found.** 5.5.1-6 and **Error! Reference source not found.** 5.5.1-7 show the temporal evolution of radial position and accelerations and tangential velocity and acceleration, in full scales and zoomed scales, respectively.

Figure_5.5.1-3. *Position of one telescope in an inertial reference frame and in the plane perpendicular to the ILS, describing its trajectory during the phase to change its radial position of 1m.*

Figure_5.5.1-4. *Tangential velocity of one telescope in an inertial reference frame and in the plane perpendicular to the ILS, the tangential velocity increase describing the ITD change phase, to come bake to the assigned velocity of 0,04 m/s controlled by the control loop.*
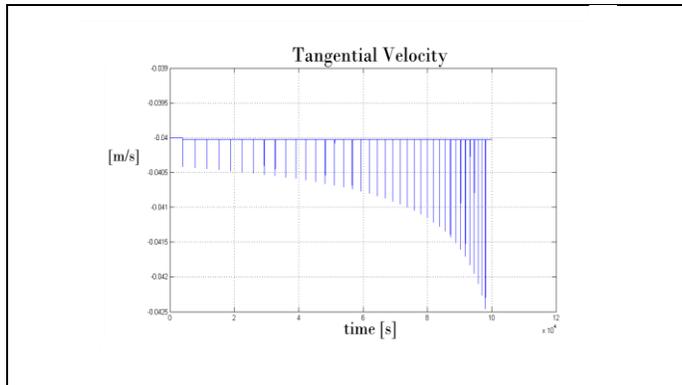
Figure_5.5.1-5. *Same as **Error! Reference source not found.**, covering the duration of a radial scan.*	**Figure_5.5.1-6.** *Particular of the radial acceleration of one telescope in an inertial reference frame and in the plane perpendicular to the ILS, describing the ITD change phase, to come bake to the assigned velocity of 0,04 m/s^2 controlled by the control loop.*
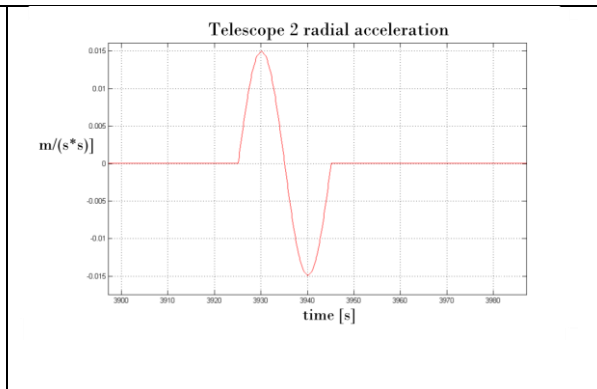
Figure_5.5.1-7. *Graphs showing particulars of some physical quantities, describing the ITD change phase, to come back to the assigned velocity of 0,04 m/s^2 controlled by the control loop.*	**Figure_5.5.1-8.** *Same as **Error! Reference source not found.**_5.5.1-7 with zoomed vertical scales.*
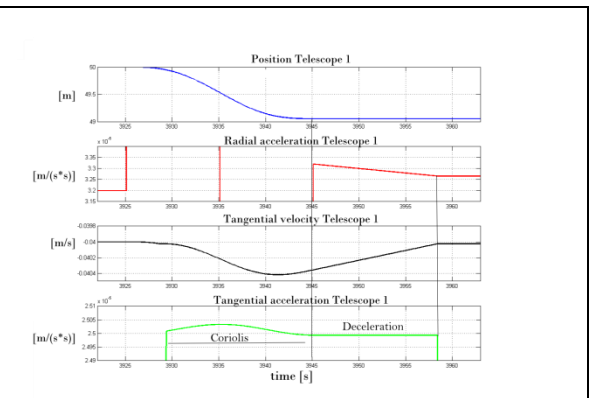
5.5.2 Thruster power

Error! Reference source not found. shows the action of the two thrusters during all the observation time to cover all the u, v plane (left) and a zoom on one of the phase change (right). The integrated thruster force is shown in **Error! Reference source not found.**_5.5.2-2, and the resulting change in angular momentum is shown in **Error! Reference source not found.**_5.5.2-3.
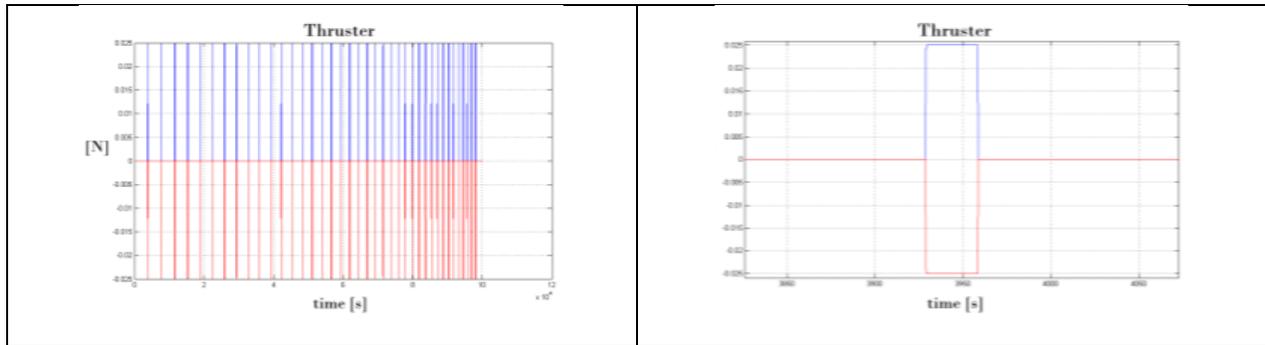
Figure_5.5.2-1 *Action of the two thrusters during all the observation time to cover all the u, v plane (left) and during an ITD phase change (right).*
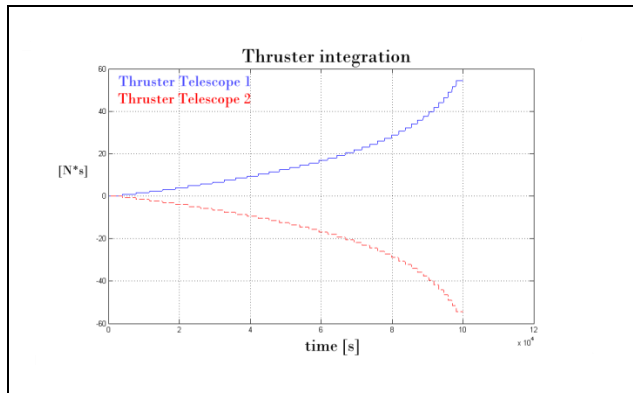
Figure_5.5.2-2. *Thruster forces integration action during the whole observation period.*
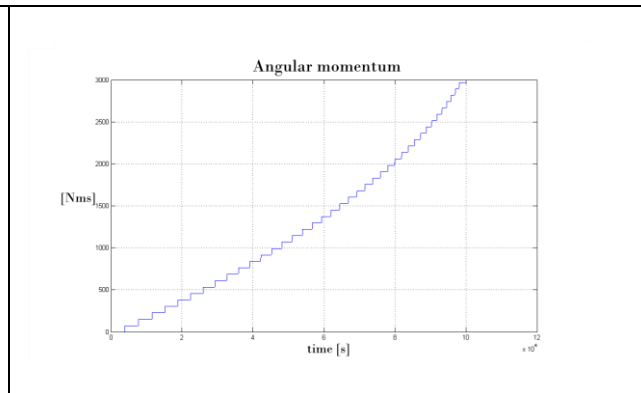
Figure_5.5.2-3. *Angular momentum change in the same time of the previous graph.*

5.5.3 Transient movements

Transient acceleration and displacements are shown in **Error! Reference source not found.**_5.5.3-1 and **Error! Reference source not found.**_5.5.3-2, respectively. Oscillations of peak-to-peak amplitude of 2 10⁻⁶g at a frequency of 0.2Hz, resulting in a displacement of 10 microns, are observed.
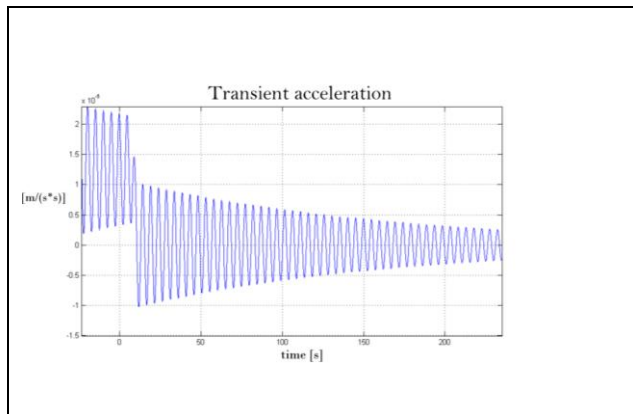
Figure_5.5.3-1 *Transient response in acceleration of each single telescope, after the shutting off the thrusters. The full vertical scale is 40 m/s² or 4 10⁻⁶g.*
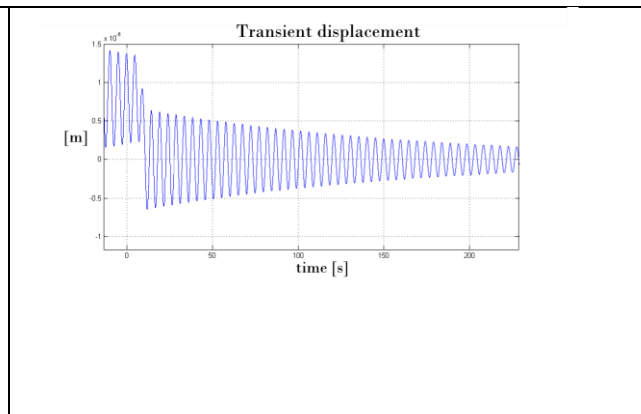
Figure_5.5.3-2 *Transient response in displacement of each single telescope, after the shutting off the thrusters. The full vertical scale is 30microns.*

5.6   ACCELEROMETER FOR A FIR INTERFEROMETER

In this subsection we report on the activities concerning the study and caracterizations of the implemented accelerometer with high sensitivity that offer the possibility to be used in a FIR Interferometer for space use. The use of an accelerometer in a FIR space interferometer, offers a unique opportunity to satisfy the metrological requirements imposed to the mission. Precision positioning of the satellites and control dynamic of the interferometer during the on target observation modes of the interferometer will have a great benefit in the use of a high accuracy accelerometer. In particular the accelerometer can be a key element of a control loop that guarantees the necessary precision during the observation modes. The activity here reporte his related to the task 2.2, dedicated to the examination of the technical challenges to implement an appropriate accelerometer to satisfy the requirement of such FIR space mission.

5.6.1   Heritage: ISA Accelerometer for BepiColombo mission to Mercury

In this subsectios are reported the heritage that is at the base of this study concerning the use of the accelerometer in a Far Infrared Space Interferometric mission is reported. In particular we report on the activity related to the use of the accelerometer ISA (Italian Spring Accelerometer) selected for the *BepiColombo* ESA Cornerstone mission to Mercury, and on the main aspects and problems of its integration on the MPO (Mercury Planetary Orbiter) *that had very strong similarity with the possible use of an accelerometer in a FIR space mission*. The described activity includes the results of a pluriannual work performed by the "Experimental Gravitation" team and the AGI srl, in the field of the fundamental physics research in gravitation and in the development of accelerometers, gradiometers and other instruments for geophysical applications.

In the BepiColombo mission, ISA (Italian Spring Accelerometer) is one of the main payloads devoted to a class of space experiments indicated as *Radio Science Experiment (RSE).* In these experiments the use of tracking techniques to measure the position and velocity of the satellite is combined to the use of an accelerometer to measure the acceleration acting in a specific point of the satellite, i.e. where it is installed, allowing to refer the Precise Orbit Determination (POD) with respect to this point, that can be regarded as in free fall, if the acceleration acting on it will be removed. BepiColombo is the first ESA interplanetary mission direct to a planet (Mercury) especially challenging because Mercury's orbit is so close to our star, and difficult to reach due to the enormous gravity of the Sun. It will be launched in 2017 with an Ariane 5 rocket from ESA Spaceport in Kourou, French Guiana, and it will arrive at Mercury in 2024.

The scientific goals of the RSE are related to the study of the planet (its structure and its gravitational field) and aim to test the general relativity to an unprecedented level of accuracy, by means of the measure of the post-Newtonian (PPN) parameters β and γ.

Apart from the transponder and the accelerometer, the RSE uses also the information of a star tracker for the absolute attitude of the spacecraft and a camera to determine the angular displacement of MPO, with respect to the Mercury surface.

5.6.1.1   The ISA accelerometer

The accelerometer selected for the BepiColombo mission – the Italian Spring Accelerometer (ISA) – has been developed at IAPS/INAF and is now under development for space use by Thales Alenia Space - Italia. A prototype with a sensitivity of 10^{-9} $m \cdot$

$s^{-2}/\sqrt{Hz}$, one order of magnitude better of what is required for the RSE, in the required frequency band ($3 \cdot 10^{-5} \div 10^{-1}\ Hz$), has already been implemented and tested for a long time.

The implementation and integration of the ISA accelerometer on the MPO take into account several requirements and conditions; among them we can recall the following ones:

- Sufficient sensitivity and appropriate frequency band of the accelerometer.
- Thermal and mechanical interfaces with the MPO, including constraints on vibrations, accommodation with respect to the MPO CoM (position, position accuracy and stability), interface temperature excursion and short-term stability, and the thermal design of the accelerometer, with the goal of minimizing its mass.
- Minimizing of the effects of any disturbances unlikely to be eliminated by spacecraft design (small-amplitude, low-frequency vibrations).
- Identification of suitable calibration methods and strategies.

We notice that all the indicated activities have to be performed also in case of the use of accelerometers in a FIR Interferometric space mission.

In Figure_5.6.1_1 it is shown the envelope of the total noise considered for the RSE, coming from the accelerometer and the tracking, in terms of equivalent accelerations. The red line represents the ISA noise, considered as white and at a level of $10^{-9} m/s^2/\sqrt{Hz}$. The green line represents the thermal noise due to a possible white noise at a level of $4°C/\sqrt{Hz}$, present at the mechanical interface between the MPO and ISA, attenuated by the passive thermal filter of the MPO. The blue line represents the total noise for the tracking expressed in acceleration. The black line represents the total noise (quadratic sum of the previous ones). This plot is a good guideline to set the limits of the vibrational noise allowed on the MPO.
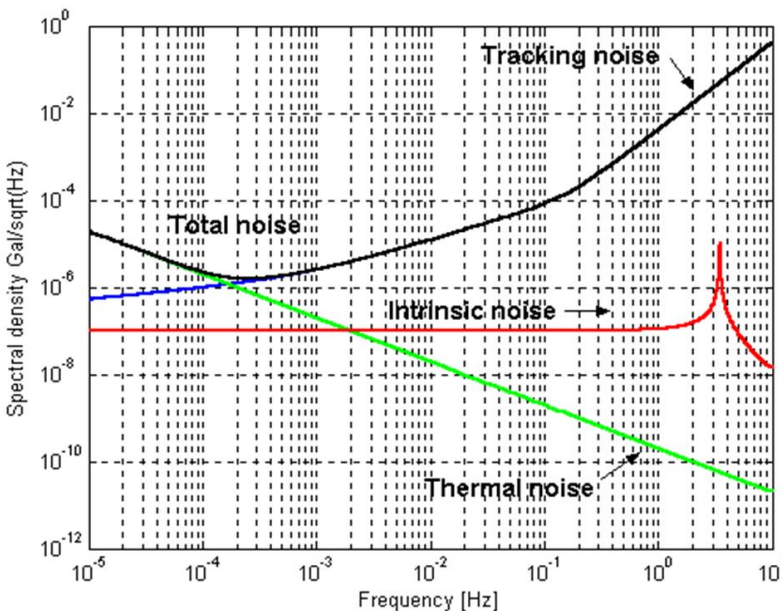
Figure_5.6.1_1 *Total noise considered for the RSE, coming from the accelerometer and the tracking, in terms of equivalent accelerations.*

Instrument System Description

The ISA Instrument configuration is based on two units: the "ISA Detector Assembly" (IDA) and the "ISA Control Electronics" (ICE) which interfaces electrically the MPO. In figure_5.6.1_2 is shown the general architecture of the instrument, where it is possible to see the three sensors with the relative sections for biasing the transducers and to pick-up the signal, amplify and read-out it after the demodulation. Also indicated are the modules for accelerometer calibration, thermal control, reference, processing and control.
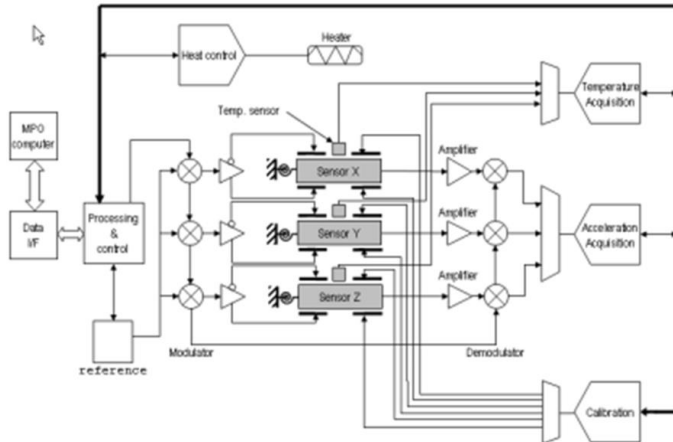
Figure_5.6.1-2 *General functional instrument architecture.*

Mechanical arrangement
The implementation of the three-axes accelerometer is made by three mechanical elements arranged with their centers of mass along the same axis (which, if possible, will be made coincident with the MPO rotation axis). This choice allows avoiding the inertial effects due to the nominal angular velocity and angular acceleration, equal to zero for points lying along the rotation axis; the gravity gradient effects will be minimized too, especially if the sensitive element with axis parallel to the rotation one is positioned with its center of mass coincident with the spacecraft CoM. In Figure_5.6.1.3 are shown the three accelerometer elements with the sensitive axis of the central element aligned along the satellite rotation axis (Z axis); the origin of the reference frame is the spacecraft nominal CoM.
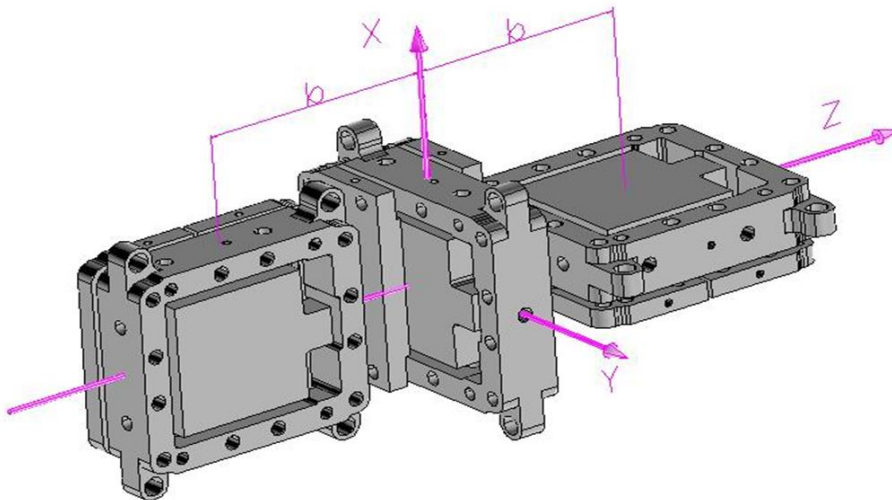
Figure_5.6.1-3 *Arrangement of the three sensitive axes*

The criteria used to implement the electronics for the accelerometer are the following ones:
- obtain the right sensitivity of the apparatus;
- be very compact;
- have the lowest level of power dissipation;
- be very stable with respect to temperature changes.

A very stable reference is used by a modulator to generate an alternate voltage that biases the capacitive bridge. The modulated signal is sent to a low-noise amplifier followed by a demodulator; after the demodulation the signal is sent to an analog-to-digital converter (A/D) that uses the same reference signal. A microcontroller commands the demodulation, the averaging, the filtering and the other functionalities of the accelerometer.

5.6.1.2 The ISA accelerometer

The accelerometer selected for the BepiColombo mission – the Italian Spring Accelerometer (ISA) – has been developed at IAPS/INAF and is now under development for space use by Thales Alenia Space - Italia. A prototype with a sensitivity of $10^{-9} \, m \cdot s^{-2}/\sqrt{Hz}$, one order of magnitude better of what is required for the RSE, in the required frequency band ($3 \cdot 10^{-5} \div 10^{-1} \, Hz$), has already been implemented and tested for a long time.

The implementation and integration of the ISA accelerometer on the MPO take into account several requirements and conditions; among them we can recall the following ones:
Sufficient sensitivity and appropriate frequency band of the accelerometer.

5.6.1.3 Instrument operations concept and error budget

The accelerometer continuously measures the three components of the acceleration acting on the MPO as well as the inertial and gravitational gradient components acting on its proof masses. The concept of the instrument operation is to detect all the accelerations that perturb its pure gravitational orbit. In fact the MPO in orbit around Mercury is a not an inertial system; in every points on it (in particular in the center of mass of each proof mass) acts an acceleration given by the following formula:

$$g(\vec{r}, t) = -\vec{\nabla} V(\vec{r}, t) - \vec{\Omega} \wedge (\vec{\Omega} \wedge \vec{r}) - 2\vec{\Omega} \wedge \vec{v} - \dot{\vec{\Omega}} \wedge \vec{r} - \vec{\alpha}(t)$$

where $V(\vec{r}, t)$ is the gravitational potential, $\vec{\Omega}$ the angular velocity, $\vec{r}$ the position vector on the satellite from the reference origin to a point on the MPO (center of mass of each proof mass), $\vec{v}$ its velocity vector, and $\vec{\alpha}(t)$ any linear acceleration acting on the MPO. The first three terms on the right-hand side can be easily recognized as gravitational, centrifugal and Coriolis accelerations, respectively. The last term depends on the variation of the angular velocity. On the reference system of the "free falling" MPO it is possible to measure also the acceleration gradients.

Inertial Effects - These effects are related with the last four terms of the previous formula. We can divide them in linear and angular accelerations.

Linear accelerations - Every point in the satellite is under the same action of linear accelerations; these can be external to the satellite, as the solar radiation pressure, and internal to the satellite, as in the case of the motion of the mechanical parts (reaction wheels among them), fuel sloshing, and mechanical vibrations with high mechanical merit

factor. These accelerations are the main components that need to be measured in order to reduce the effect of perturbations on the gravitational orbit of the MPO. It is necessary to remember that ISA is not an absolute accelerometer and therefore it is not able to measure constant accelerations, and the reliability of its output is only for measurements in its own dynamic range.

Angular accelerations - For the angular accelerations the effect on the satellite is different on points at different distances from the rotation axis; to avoid these effects the accelerometer must be installed with its center of mass very close to the MPO CoM (possibly coincident). Also in this case it is necessary to underline that ISA cannot detect constant angular accelerations, but only terms varying with time and, clearly, if the MPO center of mass is away from the center of mass of the ISA proof masses.

Coriolis acceleration - This effect arises only if there is a motion of the proof masses. Recalling that the accelerometer is hard mounted on the MPO and each proof mass can move only with one degree of freedom, the Coriolis acceleration, acting perpendicularly to this direction has no effect on it.

Gravitational effects - The gravitational effects on the ISA proof masses can be induced by a mass in the satellite and by a mass external to it. The gravitational effects induced by the satellite mass are, in general, constant and so, they are not detected by ISA. Gravitational effects induced by masses, which are in motion on the satellite, produce effects that are variable with time and likely to be detected. Such effects can be due to reaction wheels, fuel sloshing, level change of the fuel, and so on. Gravitational effects induced by masses external to the satellite are mainly due to Mercury and to the Sun.

Thermal effects - Thermal variations inside the MPO have very strong implications on the performance of the accelerometer, acting directly on it and inducing perturbations through the thermoelastic deformation of MPO structure. Recalling that the accelerometer stability is $5 \cdot 10^{-7} m/s^2/{}^{\circ}C$, this means that to avoid the impact of the thermal effects on it, the thermal variations must be less than $2 \cdot 10^{-2}\ {}^{\circ}C$ in the frequency range of the accelerometer.

Inertial effects induced by the thermal variations - ISA is not an absolute instrument and cannot detect constant signals (gravitational and inertial), but depending on the temperature change, inertial and gravitational constant effects can be "modulated" by the change of the center of mass position of the proof mass and by the change of the sensitive axis direction.

Intrinsic accelerometer noise - The last noise term that we mention here is the intrinsic accelerometer noise. It is necessary to recall that this noise is flat in the ISA frequency range, and at the level of $10^{-9} m/s^2/\sqrt{Hz}$.

Here we report schematically the error budget of ISA, with the purpose to introduce the main parameters of interest and to deduce the requirements imposed by the on board accelerometer to the MPO spacecraft. The ISA error budget can be estimated taking into account separately the two kinds of noise:

i) sinusoidal or pseudo-sinusoidal contributions;

ii) random contributions.

In Tables_5.6.1_1-2 are specified the contribution of each type of error with respect to the accelerometer accuracy $A_0 = 10^{-9}$ g. The noise of the first kind is mainly due to Mercury's gravity gradients (i.e., its tidal forces) and to the apparent forces on the rotating spacecraft,

while the noise of the second kind is mainly due to the angular-rate and angular-acceleration noise due to the MPO attitude control, necessary to guarantee the spacecraft nadir pointing. The displacement $\vec{R} = (\Delta X, \Delta Y, \Delta X)$ of each proof mass with respect to the spacecraft CoM can be seen as the sum of four different terms:

$$\vec{R} = \vec{R}_0 + \Delta\vec{R}_0 + \vec{R}_t(t) + \Delta\vec{R}_t(t)$$

where $\vec{R}_0$ represents the proof mass position in the MPO frame with respect to the nominal position of the spacecraft CoM, $\Delta\vec{R}_0$ represents the errors in knowledge of such position. The spacecraft CoM is not fixed in position in the MPO frame because of the fuel consumption and sloshing and the high gain antenna (HGA) movements. The $\vec{R}_t(t)$ term accounts for such displacements that therefore impact on the accelerometer measurements. The last term $\Delta\vec{R}_t(t)$ accounts for the error in the knowledge of the MPO CoM movements: the errors in the determination of $\vec{R}_t(t)$. In other words, $\vec{R}_0$ and $\Delta\vec{R}_0$ define the time–independent part of the proof masses positions with respect to the spacecraft CoM, while, $\vec{R}_t(t)$ and $\Delta\vec{R}_t(t)$ are the time-dependent part of the proof masses positions with respect to the CoM of the spacecraft. The value of the main involved parameters are determinate so as to keep the error budget for the pseudo-sinusoidal terms below 10^{-8} m/s² and that of the random contributions below $10^{-8} m/s^2/\sqrt{Hz}$.

As we can see, the first kind of error is directly connected to the determination of the ISA positions ($\Delta\vec{R}_0$ and $\Delta\vec{R}_t$), imposing requirements on them, while the second kind of error is connected directly to the ISA positions ($\vec{R}_0$ and $\vec{R}_t$), imposing requirements on these positions as well as in the attitude control errors ($\delta\omega, \delta\dot{\omega}$).

Table_5.6.1-1. *Error budget for the pseudo-sinusoidal noise.*

Type	Due to	Spectral content	requirement on	Error % A$_0$
Gravity-gradients	n	Orbital period P and ½P	$\Delta\vec{R}_0$; $\Delta\vec{R}_t(t)$	85
Apparent forces	$\omega_0 ; \dot{\omega}_0$	Orbital period P and ½P		
Thermal effects	2 °C	Orbital period P	ΔT	15
Components coupling	Misalignment angle	Orbital period P	$\Delta\alpha$	**Negligible**
Total				**100**

In the previous table, n represents the MPO mean motion ($\cong 7.52 \cdot 10^{-4} rad/s$), ω_0 ($\omega_0 \propto n$) and $\dot{\omega}_0$ ($\dot{\omega}_0 \propto n^2$) are, respectively, the MPO angular rate and angular acceleration, $\Delta\vec{R}_0$ and $\Delta\vec{R}_t(t)$ are the displacement errors (see the text), 2 °C represents the amplitude of the thermal effect (that will be attenuated by a factor 700 by the ISA active thermal control), finally $\Delta\alpha$ represents the error (orbital period component) of the time-independent misalignment angle of the accelerometer. The MPO orbital period P is about 8355 s. The

last column gives the maximum percentage of error over one orbital period of the MPO with respect to the requested accuracy A0 (with $A_0 = 10^{-9} g_\oplus$).

We define nominal effects, or nominal noise, the acceleration errors coming from the sum of the gravity-gradients effects with those produced by the apparent forces. The maximum disturbing accelerations produced by these nominal effects are function of the accelerometer proof masses displacements ΔX, ΔY and ΔZ with respect to the MPO CoM ($\Delta\vec{R}_0$ and $\Delta\vec{R}_t(t)$). The 85% impact for the maximum error from this nominal noise arises from the 15% constraint for the thermal effect. This is dictated by the thermal stability of the accelerometer to the temperature variations (about $5 \cdot 10^{-8} g_\oplus/°C$) and to the thermal attenuation that we are able to reach inside the accelerometer band, in particular in the low--frequency part of the accelerometer bandwidth, i.e., in the $10^{-4} \div 10^{-3}$ Hz band. The ISA active thermal control guarantees attenuation by a factor of 700. The thermal effect at the MPO orbital period has amplitude of about 2 °C; we therefore obtain for the thermal disturbing acceleration:

$$A_{therm.}|_{orb.} \cong 2 \, °C \cdot 5 \cdot 10^{-8} \frac{g}{°C} \cdot \frac{1}{700} = 1.4 \cdot 10^{-10} \, g$$

which is about 15% of the requested accuracy. With regard to the misalignment angle, estimated to be 1/3000 radians, its contribution to the error budget is negligible. Indeed, the maximum non-gravitational acceleration at the MPO orbital period is due to the direct solar radiation pressure, and it has been estimated to be $a_{sun} \cong 10^{-6} \, m/s^2$; we therefore obtain: $A_{mis.ang.}|_{orb.} \cong 1 \cdot 10^{-6} \, m/s^2 \cdot \frac{1}{3000} = 3.3 \cdot 10^{-10} \, m/s^2$

that is about 3% of the requested accuracy, and therefore negligible with respect to the other contributions.

Table_5.6.1-2. *Error budget for the random noise.*

Type	Due to	Spectral content	requirement on	Error %A
Apparent forces	$\vec{R}_0; \vec{R}_t(t)$	Random	$\delta\omega$; $\delta\dot{\omega}$	60
Thermal effects	$4 \, °C/\sqrt{Hz}$	Random	ΔT	30
Noise on the MPO	Movements due to the HGA, fuel sloshing, …	Random		10
MPO CoM displacement	Movements due to the HGA and fuel consumption, …	Random	$\Delta\vec{R}_t(t)$	70
Components coupling	Misalignment angle	Random	$\delta\alpha$	**Negligible**
ISA intrinsic noise		Random		**Negligible**
Total (not correlated noise)				**<100**

In the previous table, the vectors $\vec{R}_0$ and $\vec{R}_{t(t)}$ define, respectively, the ISA position matrix and the MPO CoM movements due to the HGA and fuel consumption. The quantities $\delta\omega$ and $\delta\dot{\omega}$ are due to the attitude control necessary to keep the MPO at its nominal angular rate and nominal angular acceleration, $4 \, °C/\sqrt{Hz}$ represents the amplitude of the thermal effect

(that will be attenuated by a factor of 700 by the ISA active thermal control), $\Delta \ddot{R}_t$ is the random acceleration noise arising from the error part of displacement of the CoM as function of time, finally $\delta\alpha$ represents the error (random component) of the misalignment angle of the accelerometer. The last column gives the maximum percentage of error with respect to the requested level of noise A (with $A = 10^{-9} g_\oplus / \sqrt{Hz}$), here assumed equal to the accelerometer sensitivity. The errors are assumed not correlated.

With regard to the results shown in Table_2.1.2-2, it is assumed that the random noise sources are not correlated and we add their contributions in a root-sum-square fashion.

5.6.2 Precision required to the accelerometer.

In the previous sections we have given information about the level of acceleration signals and frequency band acting on a FIR space interferometer, determining the range of accelerations to be measured; here we give a simple evaluation of the precision required of the accelerometer, which represents its basic element. The precision, together with the level of the acceleration value necessary to be measured, determines the dynamics necessary for the accelerometer.

If the accelerometer will be used to determine the ITD, associated to the measure of an IMU, no matter if it is used in an open loop or as elements of a feed-back loop, also to control the ITD(t) law, the considerations to derive its measuring precision follow.

For every wave-length of the spectrum in the interval $[\lambda_{min} \ \lambda_{max}] = [25 \ \mu m \ 500 \mu m]$, the distinct spatial harmonics will be obtained for variations of the ITD at steps of $0.5m$, an imprecision on the steps at level of $3mm$ seems a good requirement. In this case, the following equations hold for the acceleration and its noise:

$$a + \delta a = \omega^2 \cdot R = (\omega_0 + \delta\omega)^2 \cdot (R + \delta R) \approx {\omega_0}^2 \cdot R + {\omega_0}^2 \cdot \delta R$$

This holds if the angular velocity is measured with high precision with a STR or IMU, in order for the error in the $\delta\omega$ to be negligible. To obtain the desired precision $\delta R = 3mm$, it is necessary to employ an accelerometer with resolution better than:

$$\delta a = {\omega_0}^2 \cdot \delta R = \left(\frac{2 \cdot \pi}{T}\right)^2 \cdot \delta R = 9 \cdot 10^{-9} \ m/s^2$$

The proposed accelerometer has a precision, experimentally measured on the ground of $10^{-9} \frac{m}{s^2} / \sqrt{Hz}$, so able to perform the measure with the necessary precision also at a rate higher than 10Hz.

5.6.3 General description of the Accelerometer

In this section a description of the high sensitive accelerometers that are thought to be used in the FIR Space Interferometer is reported; the description is related to its main features and gives information about the possibility to implement an accelerometer compatible with its use on such a mission. In particular the focus has been made in its use in a feed-back loop intended for the control of the dynamics followed by the interferometer during its observation modes.

It should be emphasized that what is reported in the following is the '"heritage" of several years of activities performed by the group of the experimental gravitation of the IAPS/INAF

in the development of accelerometers with high sensitivity, to which later was added the activities carried out by AGI Ltd. in the development of accelerometers for geophysical use. The proposed accelerometer is a three axial instrument able to work in space conditions on board of a satellite in "free-fall" and so, not subject to the Earth gravity. Apart its high sensitivity and dynamic, its main feature lies in the possibility to perform its calibration on ground and so in presence of the Earth gravity.

5.6.3.1 General Description

The proposed accelerometer uses the know-how acquired in the development of high sensitive instruments to detect accelerations, as for the high sensitivity accelerometer ISA (Italian Spring Accelerometer), a tri-axial accelerometer for space applications (i.e. BepiColombo ESA mission), or gravitational effects, as in the GReAT (General Relativity Accuracy Test), an experiment to test the WEP (Weak Equivalence Principle).

Its fundamental characteristic, from which it is derived the ISA name, is determined by the fact that the test mass of each individual sensing element is attached to its reference structure by means of a mechanical spring that allows its movement only along a direction (sensitive axis), securing it tightly in the other two directions.

Every single axis of the accelerometer is constituted by three main parts:

- the mechanical oscillator,
- the signal detection,
- the actuation and control.

In the Figure_4.1-1 it is possible to see its general scheme.
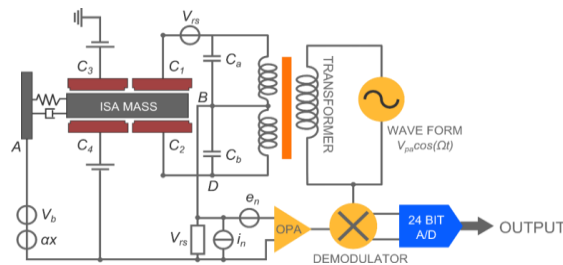
Figure_5.6.3-1 *Schematic drawing of the accelerometer scheme*

5.6.3.2 Mechanical Oscillator

The mechanical oscillator can be regarded as a test mass connected to the reference frame through a spring with low elastic constant; the acceleration acting on its reference frame (the same of the satellite) is seen as an inertial acceleration acting on the test mass. To detect these accelerations it is necessary to measure the consequent displacement of the proof mass with respect to the reference frame.
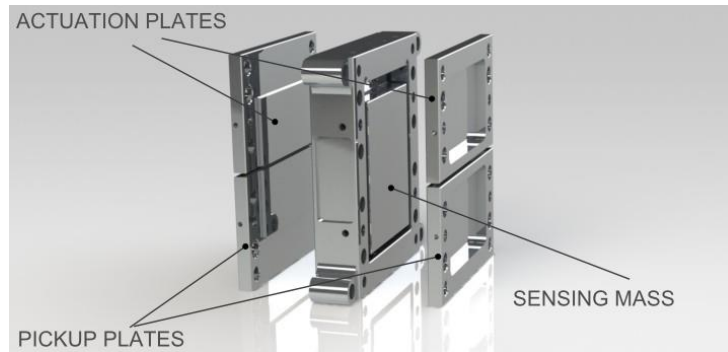
Figure_5.6.3.2-1 *Accelerometer mechanical structure.*

Figure_5.6.3.2-1 shows the mechanical part of the accelerometer. It consists of a central plate, in which the proof mass is connected to an external rigid frame by means of an elastic element (flexural or torsional) constituting a harmonic oscillator. Usually the sensitivity axis is perpendicular to the face of the proof mass. Four additional plates are connected on the opposite sides of the central one and electrically separated by insulating washers, forming plain capacitors. A couple of these capacitors provide the reading of the signal. The other couple has more than one function. It could be used: to lower the electromechanical frequency of the oscillator; to bring the capacitive bridge to its equilibrium position, by the application of a constant voltage; as an actuator, to excite the mechanical oscillator with known electrical signals.

Referring to the angle rotation of the test mass around its rotation axis, the harmonic mechanical oscillator is described by the equation:

$$I \cdot \ddot{\theta} + \eta_t \cdot \dot{\theta} + k_t \cdot \theta = N.$$

Where: k_t represents the elastic constant, I the proof mass moment of inertia, η_t its dissipation coefficient and N the magnitude of the external torque.

Equivalently, we can refer to the displacement of its *com* (center of mass) using the formula:

$$M\ddot{x} + \eta \cdot \dot{x} + k \cdot x = F,$$

with the following positions:

$$F = \frac{N}{b}, \ \ x = \theta \cdot b, \ \ M = \frac{I}{b^2}, \ \ \eta = \frac{\eta_t}{b^2}, \ \ k = \frac{k_t}{b^2}$$

Where b is the distance between the CoM and the rotation axis.

With this assumption the formulae for the evaluation of the mechanical resonance frequency and for its quality factor are respectively:

$$f_0 = \frac{1}{2\pi}\sqrt{\frac{k}{M}} = \frac{\omega_0}{2\pi} \ \ \text{and}$$

$$Q^{-1} = \frac{\eta}{M\omega_0}.$$

As we can see, the quality factor is connected to the oscillator brownian noise.
The accelerometer works at frequencies lower than the resonance frequency of the mechanical oscillator, where the transfer function between the acceleration of the sensitive mass and its displacements is: $x(\omega) \approx a(\omega)/\omega_0^2$.

5.6.3.3   Signal Detection and noise analysis

The two opposite sensing capacitors, C_1 and C_2, with the fixed external capacitors, C_a and C_b, inserted in a bridge configuration, provide the extraction of the signal. The bridge is driven by the transformer with an alternate voltage $V_p = V_{p0} \cdot \cos(2\pi f_p t)$.

The mechanical signal causes the variation of the capacity of the two detector capacitors and the subsequent modulation at the signal frequency of the residual output voltage. This signal is seen as an unbalance of the bridge. The output of the capacitive bridge is sent to a low noise amplifier, characterized by input impedance Z_i with very high value, an equivalent generator of voltage noise e_n and an equivalent generator of current noise i_n. Table_5.6.3.3-1 shows a list of the elements that appear in the scheme of Figure_5.6.3.1-1, with their meaning.

Table_5.6.3.3-1 *List of elements appearing in the electric scheme*

Element	Description
$\alpha\, x$	Voltage generator associated with signal
v_b	Generator associated with Brownian noise
e_n	Generator associated with amplifier noise
i_n	Current generator associated with amplifier noise
Z_i	Amplifier input impedance
V_{rs}	Voltage generator associated with loss capacitors

We analyze now the different contributions to the noise of the system, starting with an indication on the signal level, represented in the scheme with the $\alpha \cdot x$ generator.
If the distance between the two faces of the capacitors is $d_1 \approx d_2 = d$ the formula establishing the relationship between the amplitude value of the mechanical signal at frequency f_s and the value of the signal at the bridge output, at frequency $f_p + f_s$ or $f_p + f_s$ is: $v_s = \alpha \cdot x$, where x is the displacements of the *com* of the test mass and $\alpha = V_{CD}/(2 \cdot d)$ represents the transducer factor (maximum value of the electrical field inside each single detection capacitor).

Brownian noise associated to the harmonic oscillator
The dissipation of the mechanical oscillator is associated with a generator of Brownian noise that causes acceleration in the unit band, equal to:

$$a_b^{\;2}(\omega) = \frac{F^2(\omega)}{M^2} = \frac{4k_b T\eta}{M^2} = \frac{4k_b T\omega_0}{MQ}$$

In this equation k_b is the Boltzmann constant, T is the thermodynamic temperature of the oscillator, ω_0 is its resonance frequency, Q is the mechanical quality factor, M is its mass and η is the mechanical dissipation factor. It is clear that in order to have a low level of Brownian noise we need to have a mechanical system with a high mechanical quality factor.

Electrical dissipation and total Brownian noise.
It is easy to see that the electrical dissipations present in the transducer coupled to the mechanical oscillator produce a lowering of the total electromechanical merit factor, given by the following formula:

$$\frac{1}{Q_t} = \frac{1}{Q} + \frac{1}{Q_{de}}$$

Where

$$\frac{1}{Q_{de}} = 4\frac{\omega_0 \cdot tg\delta}{\Omega_p \cdot \beta},$$

and having indicated whit $tg\delta$ the angle of loss of the electrical part of the transducer and with β the electromechanical coupling factor given by the following formula $= \frac{\alpha^2 C}{M \cdot \omega_0^2}$, with C the transducer capacitor.
Taking into account of this dissipation, the total Brownian noise can be written as:

$$a_b{}^2(\omega) = \frac{F^2(\omega)}{M^2} = \frac{4k_b T \eta_{tot}}{M^2} = \frac{4k_b T \omega_0}{M Q_t}$$

Where $\eta_{tot} = \omega_0/Q_t$.
It is necessary to note that also the resonance frequency will slightly change when the transducer is biased.
Preamplifier noise
We can underline that an equivalent voltage noise generator and an equivalent current noise generator can model the amplifier noise contribution by means of the following formulas:

$$\begin{cases} e_n{}^2 = 4k_b T_n Z_n \\ i_n{}^2 = 4k_b T_n / Z_n \end{cases}$$

Where Z_n and T_n are respectively the noise impedance and the noise temperature of the amplifier, defined with the following relations:

$$Z_n = e_n/i_n, \qquad T_n = \frac{e_n \cdot i_n}{4 \cdot k_b}$$

These noise generators act in two different ways: directly to produce a voltage at the input of the ideal amplifier; producing a fluctuation of charge across the detection capacitors and a consequent acceleration in the harmonic oscillator.
Total system noise
Using the previous indications, the total noise in acceleration, from the point of view of the mechanical oscillator, can be expressed by the formula:

$$a_t{}^2(\omega) \approx \frac{4 \cdot k_b \cdot \omega_0}{M}\left[\frac{T}{Q_t} + T_n\frac{4Z_n C \omega_0}{\beta}\right]\Delta f$$

Where $\Delta f = 1/\Delta t$ is the inverse of the acquisition time for each single measurement.

5.6.3.4   Use of the control capacitors

In this subsection we will give indications about the use of the control capacitors that can produce modifications of the frequency of the oscillator, electrical variation of the capacitive pick up-bridge, and as electromechanical actuator.

Electrical lowering of the frequency of the mechanical oscillator
Applying a constant voltage V across one of the control capacitors a torque is produced that, for small ϑ, is given by:

$$M = -\frac{1}{2}V^2\left(-\frac{C_0}{d_0}b + \frac{C_0}{d^2_0}b^2\vartheta\right)$$

where b is the distance between the center of mass of the central plate and the rotation axis, ϑ is the rotation angle, C_0 is the capacity of the capacitor, when the plate is in its equilibrium position, V is the voltage on it and d_0 is the distance between the two faces of the planar capacitors. The term depending on ϑ has the effect of a negative elastic constant that reduces the torsion elastic constant of the oscillator, causing a lowering of the system resonance frequency. The new frequency is given by:

$$\omega^2 = \frac{k - \frac{V^2 C_0}{d_0^2}b^2}{I} = \omega_0^2(1-\beta)$$

where we have introduced the electromechanical transducer factor β:

$$\beta = \frac{C_0 V^2}{m\omega_0^2 d_0^2}$$

The simultaneous application of the constant voltage on two opposite capacitors gives a factor of 2 in the previous formula and allows maintaining the proof mass in its equilibrium position. We must say that this procedure, essential to increase the accelerometer sensitivity, reduces its frequency band.

Electrical variation of the equilibrium conditions of the capacitive bridge
The term in equation of the momentum, that doesn't depend on ϑ, represents a constant torque that changes the position of the proof mass and therefore the four capacitors capacitance values. Simple evaluations indicate that the value of the capacitor on which the constant voltage V is applied and that of the adjacent capacitor, increases according to the equation:

$$C(V) = C_0\left(1 + \frac{1}{2}\frac{C_0 V^2 b^2}{4k_t d_0^2 - V^2 C_0 b^2}\right) = C_0\left(1 + \frac{1}{2}\frac{\beta}{1-\beta}\right)$$

On the other hand, the capacitors capacity decreases. It is clear that if we want to have a low frequency and get large variations of capacity, we need to have high values of β. We must notice that if $\beta = 1$ the frequency becomes zero, two capacities go to infinity and two

to zero (this in principle). This means that the system becomes unstable; the attraction force, determined by the electric field between the two faces of the capacitor, is equal to or larger than the elastic restoring force.

Electromechanical actuator

To characterize the system it is useful to have the possibility to excite it at known frequencies. This possibility is obtained using the control capacitors as an actuator. Superimposing an alternate voltage $v = v_0 \cos(2\pi f_e t)$ to the constant voltage V, from equation 3 we can see that, besides the terms seen before, a torque M_1 results at frequency f_e, given by:

$$M_1 = \frac{C_0}{d_0} bvV \ ,$$

At 2 f_e, the torque is equal to:

$$M_2 = b \frac{C}{d_0} v^2 \ .$$

Terms causing small variations of the elastic constant are not considered. Such an actuator could be used to calibrate using an electrical signal.

5.6.4   Accelerometer calibration

In this section the concept for the ISA accelerometer calibration on the ground and in space is described. As already said, the difficulties to calibrate an apparatus for gravitational measurements on-ground are mainly due to the presence of environmental noise and of Earth's gravity. We start remembering that for the accelerometer here considered, of the ISA kind, that must operate in a frequency band: $(3*10^{-5} \div 10^{-1} \ \text{Hz})$, it is almost impossible to insulate the apparatus from the environmental noise; so, any calibration must be performed while trying to circumvent the unavoidable seismic noise, or forcing it at a level of excitation well above it.

5.6.4.1   Parameter measurements

A first way to calibrate the accelerometer is by means of the measurements of all the fundamental parameters that determine its characteristic in terms of sensitivity and to evaluate it by means of calculation. In the previous section the formula for the evaluation of the accelerometer total noise has been given, both electrical and of mechanical nature for every single axis of the accelerometer; in tables_5.6.4-1/2 are shown the main mechanical and electrical parameters necessary to be measured experimentally so to evaluate the accelerometer intrinsic acceleration noise.

Table_5.6.4-1 *Mechanical parameters of the oscillators*

M	Proof mass	0.22 kg
I	Inertia	$4 \cdot 10^{-4}$ kg/m^2
f_o	Mechanical resonance frequency	3.5 Hz
Q_m	Mechanical quality factor (environment vacuum)	$0.3 - 10^4$

Table_5.6.4-2 *Electrical parameters of the accelerometer*

| $C_1 = C_2 = C_3 = C_4$	Detection and actuation capacitors	300pF
$tg\delta_{C1}$	Angle of electrical loss in the capacitors	$4*10^{-4}$
$C_a = C_b$	External fixed capacitor	300pF
$tg\delta_{Ca}$	Angle of electrical loss in C_a	$3*10^{-4}$
v_n	Equivalent voltage noise generator	$3*10^{-9}V/\sqrt{Hz}$
i_n	Equivalent current noise generator	$7*10^{-15}A/\sqrt{Hz}$
T_n	Amplifier noise temperature	0.38K
Z_i	Amplifier input impedance	$8*10^5\Omega$
A	Amplification	50
α	Transducer factor	$10^5V/m$
β	Electromechanical transducer factor	$3*10^{-2}$

Let us recall that the mechanical quality factor Q_m is tightly related to the vacuum conditions in which the sensor is located, being strongly dependent on the gas trapped in the gap between the faces of the plain capacitors. The two values indicated in table_5.6.4-1 for Q_m are related to the pressure of 10^3 *and* 10^{-4} *mbar*.

From the values reported in the Table_5.6.4-1/2 it is possible to evaluate the sensitivity of the accelerometer; this gives a value equal to $3.3\cdot10^{-12}g_\oplus/\sqrt{Hz}$ in vacuum and $3\cdot10^{-10}g_\oplus/\sqrt{Hz}$ at atmospheric pressure (limits due to the Brownian noise). For the BepiColombo ISA accelerometer we chose a Q_m equal to 100, so that the resulting sensitivity is $10^{-9}m/s^2/\sqrt{Hz}$

5.6.4.2 On Ground calibration

The analysis of the noise sources and the theoretical evaluation of the performance of the accelerometer are not satisfactory and, consequently, direct experimental tests are necessary. In the Figure_5.6.4.2-1 we show a prototype of the implemented accelerometer. The main parts of this instrument are the three mechanical units (with their own preamplifiers) arranged in order that their sensitive axes are perpendicular to each other. In the same box are also included the microcontroller and all the electronics for power supply, demodulation of signal and acquisition of data.

For on-ground calibrations the accelerometer is disposed on a base equipped with three support points, controlled with micrometer screws. By adjusting these screws, the gravity acceleration can be set parallel to a sensitive axis (e.g. z) and perpendicular to the other two axes (x, y). In these conditions the unit with sensitive axis along the vertical is subjected to acceleration equal to 1 $g_\oplus$; the other two units are sensitive to a component of $g_\oplus$ depending on the angles ϑ_x, ϑ_y, from the horizontal plane. For small variations of ϑ_x, ϑ_y, their value in radians corresponds to the acceleration in $g_\oplus$ to which the unit is subject.
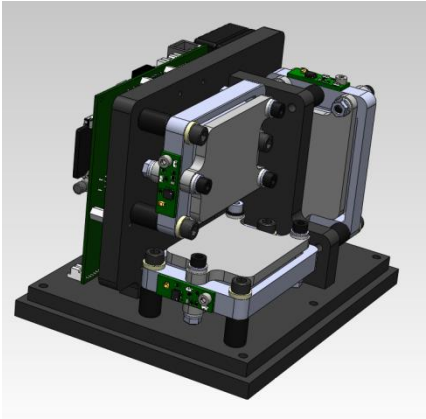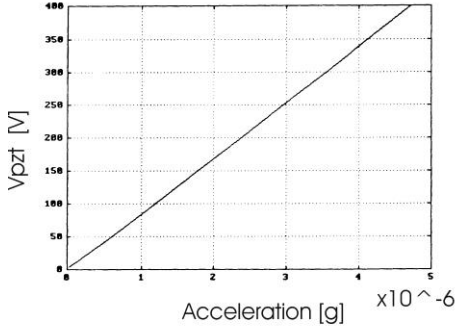
Figure_5.6.4.2-1 *Prototype of ISA accelerometer.*	**Figure_5.6.4.2-2** *Output of the accelerometer excited with d.c. accelerations.*

Measurement of transducer factor and linearity

The calibration of each single unit of the accelerometer is performed applying to it a known component of the gravity acceleration by varying the proper angle (ϑ_x , ϑ_y) and by reading the related output. In this case the connection between the input acceleration and output voltage is direct and enables an evaluation of the transducer factor. To perform an evaluation also of the system linearity, the micrometer screws are replaced with a piezoelectric element, able to give a very small displacement with a sonsequent small change of the angle. Figure_5.6.4.2-2 shows the output of a single unit of the accelerometer, excited with d.c. accelerations, step by step. The x-axis represents the acceleration measured by the accelerometer, while the y-axis represents the voltage given to the piezoelectric. It also represents the inclination in radians (multiplied by a conversion factor equal to $2 \cdot 10^{-8} \, rad / V$). The plot shows the linearity of the accelerometer response, for a wide range of accelerations.

Measurement of the electromechanical actuation factor

Biasing one of the control capacitors with a constant voltage *V*, and superimposing an alternate voltage $v = v_0 \cos(\omega_e t)$, a torque equal to $M_1 = \dfrac{C_3}{d_3} bvV = \alpha_{att} . v$ at frequency f_e will arise, where C_3 is one of the two control capacitors, b the distance between the rotation axis of the oscillator and the proof mass CoM, and d_3 the distance between the two faces of the plane capacitor. From the experimental measurement of the parameters that appear in the formula, it is possible to evaluate the actuation factor α_{att} . Another possibility is to measure it experimentally. The measure is performed applying to the accelerometer elements to be calibrated a well-known torque by changing the component of gravity acting on them, by means of the micrometric screw system and measuring the voltage necessary

to produce the same torque. We have to remember that in this case the torque is given by:

$$M_1 = \frac{C_3}{d_3} bV^2 = \alpha_{att} V .$$

Usually in the use of the electromechanically actuator, the two actuators capacitor are used simultaneously in order to avoid the bias voltages producing a constant torque that unbalances the pick-up bridge.

Measurement of the accelerometer transfer function (resonance frequency and mechanical quality factor)

An important requirement of an accelerometer is to have a flat transfer function in its frequency band; in our case this is obtained because the accelerometer transfer function is primarily related to the mechanical harmonic oscillator that operates at frequencies well below its resonance frequencies, while the actuation system and its pick-up (amplifier, demodulator) give a contribution flat in frequency (very narrow band around the pick-up bridge bias frequency). The measurement of the transfer function can be performed in two ways: exciting the system using the electromechanical actuator with a constant amplitude voltage swept in the frequency range where the transfer function must be evaluated, or exciting the system with a direct acceleration, using the micrometer screw so to change the component of $g_\oplus$ acting on the specific element with sensitive axis initially in the horizontal plane.

The Figure_5.6.4.2-3 shows the transfer function of one single axis of the accelerometer. In this case, Q_m is kept low by avoiding high vacuum conditions, so to allow the use of a dynamic signal analyzer, which does not work correctly if Q_m is high. As it can be seen, above the fundamental frequency, equal to 3.5 Hz, the system has a second harmonic at 16.6Hz.
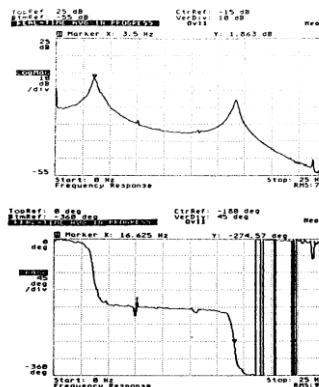
Figure_5.6.4.2-3 *Transfer function of the accelerometer.*

From the previous arguments it follows that the parameters necessary to characterize the transfer function are the mechanical frequency, the mechanical quality factor and the response of the system at zero frequency. The correct determination of the transfer function is evaluated with a precise determination of these parameters. The measurement of the mechanical frequency and of the high mechanical Q (100 in this case) is performed placing the accelerometer in a vacuum chamber, exciting the mechanical oscillator at its resonance at high level and looking at its free exponential decay.

Measurement of the intrinsic noise of the system

Every single axis of the ISA accelerometer can be calibrated on ground under the action of gravity by placing it in a horizontal plane so to null the Earth gravity effects. Differential measurements, performed with two accelerometer elements with sensitive axes parallel, permit to reject the horizontal seismic noise present in the laboratory, leaving to check their sensitivity at levels better than $10^{-10}m/\sqrt{Hz}$. In the figure_5.6.4.2-4 are shown the signals recorded by two ISA accelerometer elements arranged with their sensitive axes parallel. As it is possible to see, every
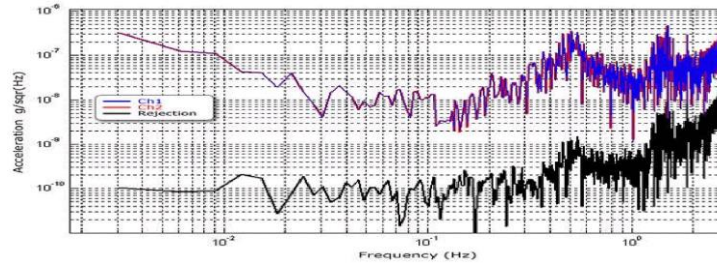
Figure_5.6.4.2-4 *Difference of seismic signals recorded by two ISA elements arranged with their sensitive axes parallel* between them.

element detects the seismic noise present in the laboratory, showing a minimum equal to $10^{-8}g/\sqrt{Hz}$ at frequencies of about 10^{-1} Hz (red and blue line). The estimate of the sensitivity of the apparatus at the lowest level and in such low range of frequencies has been possible only using differential measurements methods. In the same figure the level of the difference between the two previous signals is shown; the residual level is obtained adjusting the parameters for the comparison of the two accelerometers output in order to obtain a Common Mode Rejection factor bigger than 10^4. This residual acceleration at a level of 10^{-10} $g/\sqrt{Hz}$ can be retained as an indication of the level of the accelerometer intrinsic noise. To be noted that the indicated residual noise is reached in a large band of frequencies i.e. $10^{-3} - 5 \cdot 10^{-1}$ Hz.

Figure_5.6.4.2-5 *Arrangement of the two mechanical elements disposed with their sensitive axes parallel and in a horizontal plane.*	**Figure_5.6.4.2-6** *Arrangement of the two separate electronics with only a common element to perform the rejection.*
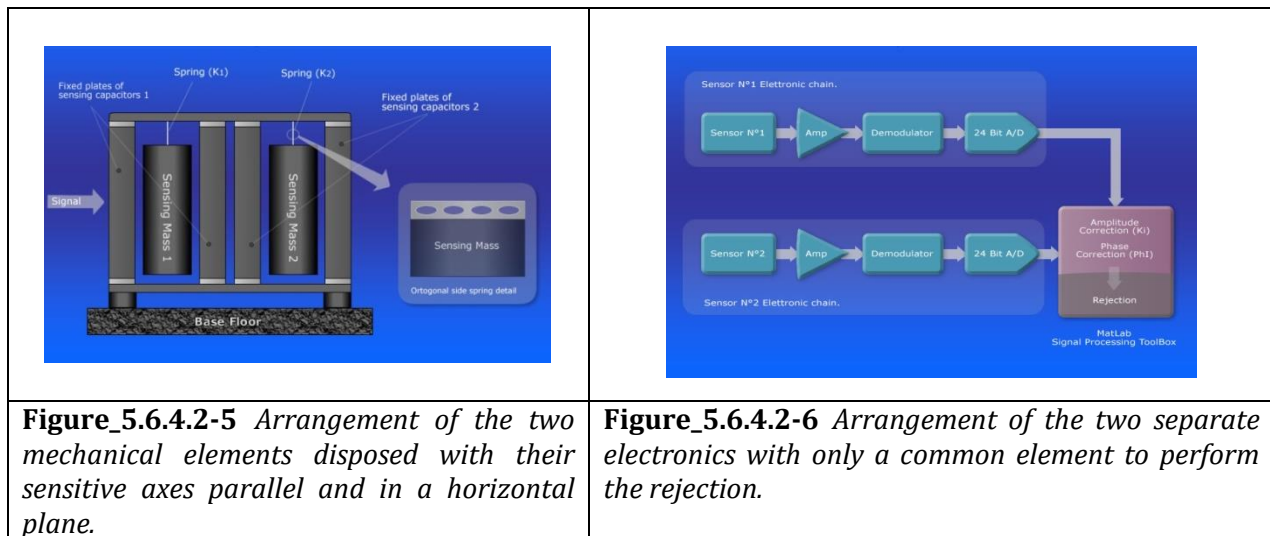
In the following figures_5.6.4.2-5/6 we reported the arrangement used to perform the previous calibration. The first one showing the mechanical arrangement, with the two

mechanical elements disposed with their sensitive axes parallel, while the second one showing the two separate pick-electronics chains.

Measurement of the ISA thermal stability

One of the main characteristics for an accelerometer is its thermal stability, i.e. its capability to be immune from changes of temperature in the environmental in which it operates. The proposed accelerometer has a thermal stability equal to $5 \cdot 10^{-7} m/s^2/°C$. The stability figure means that, a temperature change of one degree, on the electronics or mechanical parts, produces a spurious accelerometer output equivalent to an accuracy of $5 \cdot 10^{-7} m/s^2$. The only possibility to reduce this effect is to reduce the thermal variations of the environment, by means of a thermal control system. The thermal attenuation can be obtained using an active control loop or a passive one. The advantage of the active control resides in the possibility to attenuate the temperature variations at very low frequency, but this requires additional power dissipation. The passive control method consists in the employment of a system with a very large time constant for its thermal inertia, in order to have a system with a very low cutoff frequency, ensuring the required thermal attenuation inside the measurement frequency band. The calibration of this parameter is performed inserting the device into a thermo-vacuum chamber in order to change its temperature and control the corresponding signal at the output of the accelerometer due to the change in temperature.

In flight calibrations

Also if the accelerometer is calibrated on ground, at the launch of the satellite, it will be subject to very strong shock acceleration that can change its fine adjustment and so its calibration; the use of the actuators described in the previous section can permit to calibrate in flight the accelerometer, submitting it to a known electrical force, providing that the actuators have been calibrated on ground and counting on the fact that this calibration, depending only on the values of the applied voltages and on the distance between the two faces of the actuator capacitor, do not change at the moment of launch.

5.6.5   Accelerometer Characteristics

In this section we report the main characteristics of the implemented accelerometer; as it is possible to see from the reported data sheet it is well representative of the accelerometer that could be used on board a FIR space interferometer and it is actually the same type that has been employed in the on-ground test-bed as well as in the test-bed using the nano-sat.
In the table_5.6.5-1 the main characteristics for every one of the three axes of the implemented accelerometer are reported

Table_5.6.5-1 *Main Accelerometer Characteristics for every single axis of the implemented accelerometers.*

Parameters	Value
Sensitivity	1e-8 g/sqrt(Hz)
Frequency band	10^{-3} Hz – 10 Hz
Dynamic pre-processing (dB)	120
Dynamic post-processing (dB)	140

Weight (Kg)	2.5
Dimensions	155x125x125 mm
Acquisition system with preprocessing	24bit
Acquisition frequencies (Hz)	0.1,0.2,0.5,1,5,10,20
Output	Analogic or digital
Data rate (10Hz Acc. And one T) ($byte/s$)	500
Internal thermometer Pt10000	Precision better than 10^{-4} °C
Interface of communication	RS232 full-duplex/ RS485 (with adaptor)
Standard of communication	NMEA
Dimensions of a single axis mechanical element (mm)	80 x 60 x 25 (H x L x A)
Electronic dimensions for a single element (mm)	95x95
Voltage supply via USB or external (V)	5
Power dissipation (mW)	75
Linearity	> 80 dB
Internal memory	SD 2Gb
Pre-processor embedded for pre-elaborations, control and acquisition	

In the figure_5.6.5-1 a picture of the three axes implemented accelerometer is shown, while in the figure_5.6.5-2 one of the three mechanical elements with its proximity electronics is shown. In the figure_5.6.5-3/4 the single mechanical oscillator and the particular of the elastic elements are shown.

Figure_5.6.5-1 *Picture of an open view of the implemented three axes accelerometer.*

Figure_5.6.5-2 *Picture of one of the three mechanical elements with its proximity electronics.*
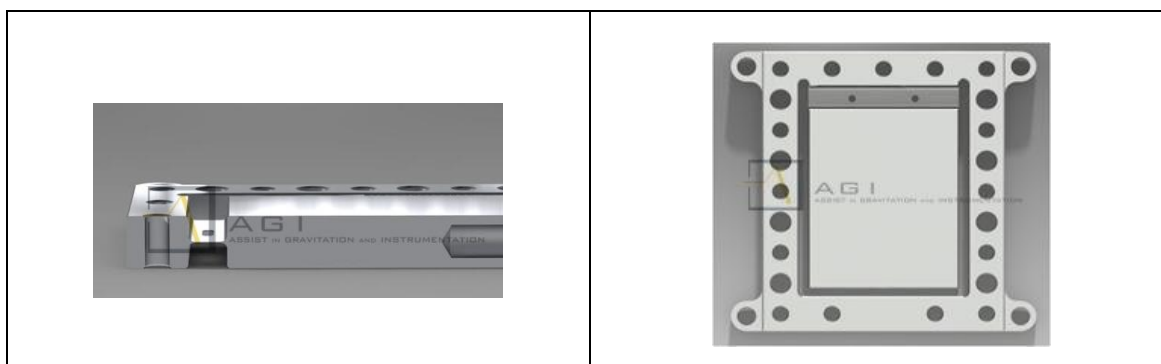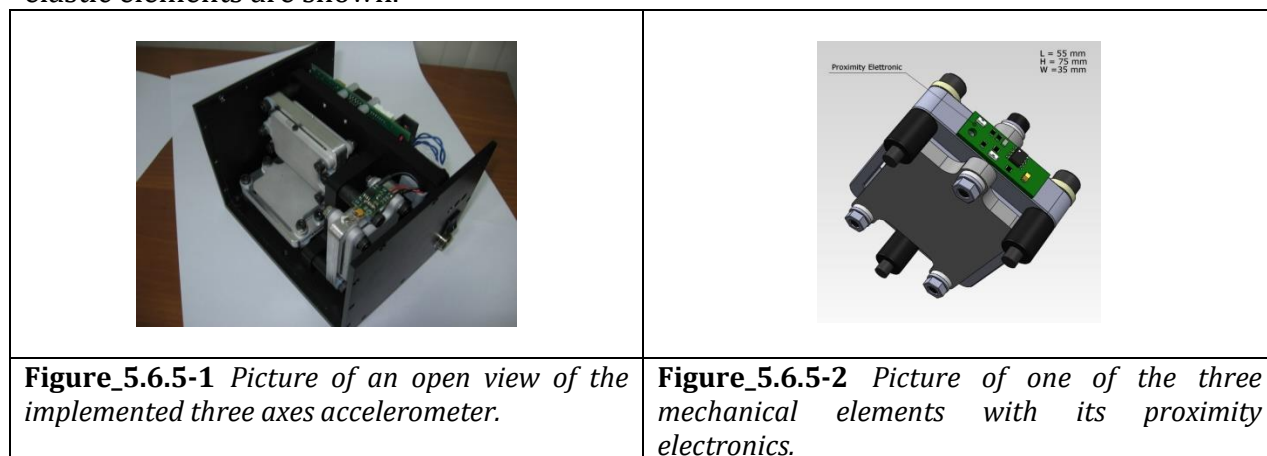
Figure_5.6.5-3/4 *Mechanical oscillator and the particular of the elastic elements.*

In the last three figures we show respectively: a picture of an open view of the accelerometer showing the implemented electronics; the conceptual scheme of the electronics; and the scheme of the front-end amplifier.

Figure_5.6.5-5 *A picture of an open view of the accelerometer showing the implemented electronics.*

Figure_5.6.5-6 *Conceptual scheme of the electronic section.*
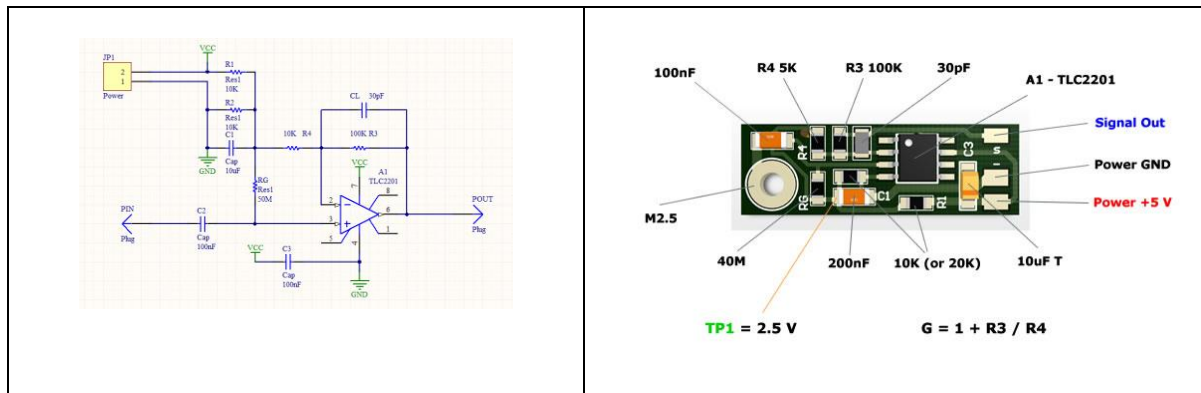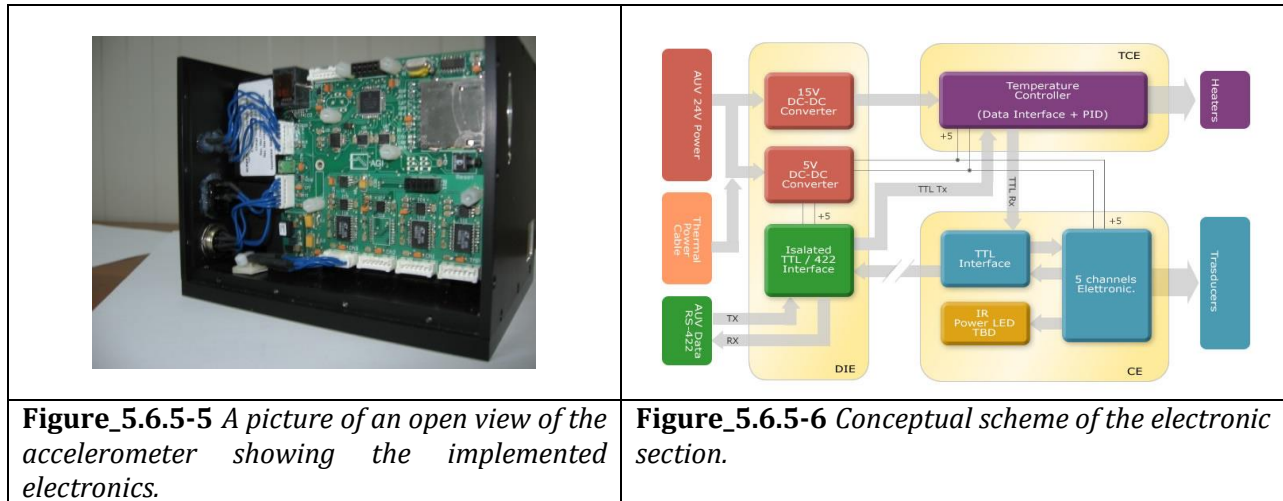
Figure_5.6.5-7 Scheme of the front-end pre amplifier.

5.7 CONCLUSIONS OF THE SECTION

The objectives associated to the Del_2-3 concerned the study related to the use of a high sensitive accelerometer as one of the principal elements of a control loop, for the precise metrological control of a FIR Interferometer space mission. The activity has been divided in four main parts, here after briefly described them, together with the relative conclusions:

1) *A preliminary study concerning the context of the accelerometer use, with the evaluation of the dynamical acceleration, arising during the observation mode and the acceleration noise acting on the FIR interferometer, in the frequency band where the interferometric signals will be detected and out of it.*

The possibility to use a high sensitivity accelerometer in a FIR Interferometer for space use, so to help satisfy the metrological requirements imposed to the mission has been studied,

with particular attention to the precise positioning of the satellites and to control the dynamics of the interferometer during the observation modes.

Preliminary studies have been done in order to have a detailed knowledge of the kind of acceleration signals and noise present on a FIR space interferometer. In particular two classes of acceleration have been analysed:

a) Acceleration and gravity gradient acceleration arising on the whole structure of the interferometer during its observation mode and connected to its dynamics.

b) Acceleration noises present on the interferometer due to the appendices movements (RW, SA, HGA) and to the transient oscillation of the whole structure of the interferometer, when the thrusters are used.

The first class of accelerations are the ones to be measured and controlled so to maintain the interferometer in its proper dynamics, following the appropriate movement so to fill the whole u, v plane. The second class is that concerning the acceleration noises acting in a frequency band where the spectroscopic signals are sent by means of the optical path delay and seen as a phase noise or piston effects.

Concerning the accelerations at point a) has been evaluated the gravity gradient acceleration acting on a system of two satellites placed in L2 and the consequent gravity accelerations due to the dynamics of the interferometer arising during observation. **The conclusion concerning this part of study is that the gravity gradient acceleration is negligible and only the one due to the dynamics must be considered in the control loop.** Several possibilities to perform the observation mode using different laws to change the ITD have also been studied, and for every one we have determined the frequency band and amplitude of the arising tangential and radial accelerations.

Concerning the accelerations included in point b), a structural analysis of a FIR interferometer with the two telescopes interconnected to a central Hub by means of two booms has been performed, so to have a possibility to reach a max $ITD = 100m$, and determine its resonance frequencies, that will been excited during the transient phase (as the ITD change); this information is taken into account in the determination of the more appropriate FIR control dynamics. We also investigated the level of noise acceleration present in a satellite in the frequency band where the spectroscopic signal will be detected and out of this band due to its possible influence as aliasing effects and saturation of the accelerometer itself.

The conclusion concerning these activities is related to the methodology to use for the choice of the frequency range where the spectroscopic signal can be translated by means of an appropriate sledge velocity, where its level is at the minimum. The same analysis can give the opportunity to set appropriate requirements for the level of acceleration noise that can be present on the FIR Interferometer.

2) *Activity concerning the possibility to implement a control-loop for the dynamical movements of the interferometer by means of appropriate simulation, followed by an experimental activity with an on-ground test bed.*

Using the information obtained by the activity described at the previous point, an activity concerning the implementation of a control loop has been performed; in the performed analysis the characteristics of a FIR Interferometer, with the two telescopes interconnected to a central Hub by means of two booms, respecting the real dimensions ($ITD = 100m$) and weight has been considered. This theoretical activity has been accompanied with

simulation of the system with an on-ground test bed. The conclusions are that it is possible to implement such kind of control loop using accelerometers, in a simple way also by means of a PID (Proportional, Integrative, and Derivative) control. The on ground test-bed activity has given a good idea on what happens during the control procedure.

3) *Activity concerning the definition of an accelerometer that meets the requirements imposed by its use in a FIR interferometer space mission and implementation of a prototype of accelerometer with such characteristics.*

In this part of the activity the characteristics of an accelerometer useful to be one of the main elements of a feed-back control loop for the FIR Interferometer have been defined. In the definition of such an accelerometer the main output relative to the previous parts of the study and the entire heritage derived from the implementation of the ISA (Italian Spring Accelerometer), the accelerometer developed for the ESA cornerstone mission for the exploration of Mercury has been used. **The conclusion is that such accelerometer has been defined and implemented; the performed tests demonstrate its perfect adherence to the requirements imposed by its use in a FIR Interferometer.**

4) *A last activity has been devoted to the participation to a space test-bed using a nano-sat, where an accelerometer will be tested.*

This last activity was devoted to test a single sensitive axis accelerometer, which has characteristics close to those that must be used in an interferometric mission. The test-bed will permit to verify the sensitivity of the accelerometer element in space, due to the fact that the orbiting nanosatellite has a sufficiently low noise level; while it is foreseen that a "big" acceleration will be detected, especially in the phases of its insertion in orbit, so to verify the functionality at a high level. A more complex test foreseen is to verify the frequency response of the accelerometer. Due to the low power available in the nanosatellite, it is not possible to use a temperature control system, so the accelerometer will have a spurious response in temperature that could mask the low frequency accelerometric signal; to mitigate these effects the accelerometer will be accompanied with a thermometer which should allow in part the reconstruction of these effects. The accelerometer element has been completely projected, taking into account also the mechanical and electrical interfaces.

6 VALIDATION OF KEY TECHNOLOGIES WITH NANO-SATELLITE

Space-born tests of key technologies, as offered by a nano-satellite mission, will be an important ingredient to improve the FIRI Technology Readiness Level (TRL) and the Task 2.3 of this study has been dedicated to the validation studies of the key technologies of FIRI with nano-satellite. The study regarded the technology validation test-bench and associated support equipment of several optics, mechanics, and electronics parts.

Preliminary parts of study have been focused to the definition of the concept of nano-satellite and resources (mass, volume, power, telemetry) typically available for the payload.

The second part of the study has been devoted to the selection of the FIRI key technology to be studied and implemented as first technological valifation.

6.1 NANOSATELLITE AND CUBESAT OVERVIEW

The nanosatellite shall provide a validation test in space for a key technology of FIRI. In this section, the main characteristics of the nanosatellite and resources available for the payload are described.

One reason for miniaturized satellites is to reduce the cost: while classical satellites require large and costy rockets, smaller and lighter satellites require smaller and cheaper launch vehicles and can sometimes be launched in multiples. They can also be launched in 'piggyback', using excess capacity of launch vehicles.

Besides the cost issue, the main rationale for the use of miniaturized satellites is the opportunity to enable missions that a larger satellite could not accomplish, such as:

- ✓ Constellations for low data rate communications
- ✓ Using formations to gather data from multiple points
- ✓ In-orbit inspection of larger satellites.
- ✓ University Related Research

6.1.1 Nanosatellite

The term "nanosatellite" or "nanosat" is applied to an artificial satellite with mass between 1 and 10 kg. For example, Figure_6.1.1_1 (left) shows the nanosat called WebSat which was developed by Ecole Polytechnique Fédérale de Lausanne. It is a 3 kg nanosatellite which is intended to broadcast Earth pictures on-line in real time from a 400 km Sun synchronous orbit.

Figure_6.1.1-1 – *LEFT: 3D view of WebSat: a nanosatellite broadcasting Earth pictures on-line in real time. MIDDLE: Picture of Cute-I, a 1U cubesat developed to tests* commercial components. RIGHT: Picture of Quake Sat, a 3U cubesat developed to detect low frequency emissions during earthquakes.

6.1.2 Cubesat General Description

A cubesat is a type of nanosatellite for space research that usually has a volume of exactly one liter (10 cm cube), mass no higher than 1.33 kg, and typically, it use off the-shelf commercial components (COTS) for its electronics.

Beginning in 1999, California Polytechnic State University (Cal Poly) and Stanford University developed the cubesat specifications to help universities worldwide perform space science and exploration. The cubesat specification accomplishes several high-level goals. Simplification of the satellite's infrastructure makes it possible to design and produce a workable satellite at low cost. Encapsulation of the launcher-payload interface takes away the prohibitive amount of managerial work that would previously be required for mating a piggyback satellite with its launcher.

Unification among payloads and launchers enables quick exchanges of payloads and utilization of launch opportunities on short notice.

The term "CubeSat" was coined to denote nanosatellites that adhere to the standards described in the cubesat design specification. Cal Poly published the standard in an effort led by aerospace engineering professor Jordi Puig-Suari. The specification does not apply to other cube-like nanosatellites such as the NASA "MEPSI" nanosatellite, which is slightly larger than a cubesat.

In 2004, with their relatively small size, cubesats could each be made and launched for an estimated $65,000–$80,000. This price tag, far lower than most satellite launches, has made cubesat a viable option for schools and universitie. Because of this, a large number of universities and some companies and government organizations around the world are developing cubesats — between 40 and 50 universities in 2004, Cal Poly reported.

As example, Figure 1 (Middle and right) shows two cubesats: Cute – I (developed by Tokyo Institute of Technology) and Quake Sat (developed by Stanford University), a 1U cubesat and a 3U cubesat respectively. The first one is designed to test COTS components whereas the second one aims to detect extremely low frequency radio emission of seismic activity during earthquakes.

The standard $10 \times 10 \times 10$ cm basic cubesat is often called a "1U" cubesat meaning one unit. Cubesats are scalable along only one axis, by 1U increments, allowing for simple implementation of "2U" ($20 \times 10 \times 10$ cm) and "3U" ($30 \times 10 \times 10$ cm) cubesast.

6.1.2.1 Cubesat deployment system

Since cubesats all have cross-section 10x10 cm regardless of length, they can all be launched and deployed using a common deployment system. Cubesats are typically launched and deployed from a mechanism called a Poly-PicoSatellite Orbital Deployer (P-POD), also developed and built by Cal Poly. The P-POD is a rectangular box with a door and a spring mechanism, as shown Figure6.1.2.1-1.

P-PODs are mounted to a launch vehicle and carry cubesats into orbit, deploing them once the proper signal is received from the launch vehicle. P-PODs have deployed over 90% of all cubesats launched to date (including un-successful launches), and 100% of all cubesats launched since 2006. The P-POD Mk III has capacity for three 1U cubesats. Since three 1U cubesats are exactly the same size as one 3U cubesat, and two 1U cubesats are the same size as one 2U cubesat, the P-POD can deploy 1U, 2U, or 3U cubesats in any combination up to a maximum volume of 3U.
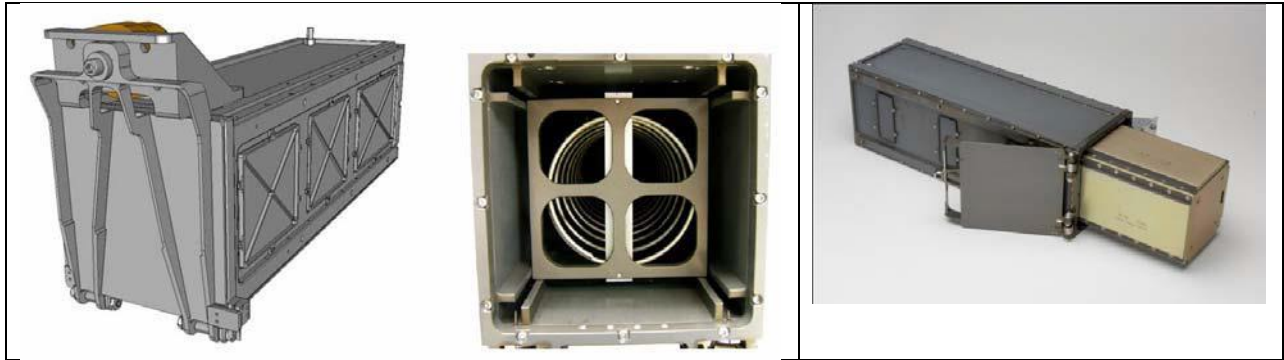
Figure_6.1.2.1-1 – *Cubesat deployment system P-POD*

6.1.2.2   Cubesat background

The first cubesats were launched in June 2003 on a Russian Eurockot, and approximately 75 cubesats have been placed into orbit since August 2012. We have elaborated a statistical survey of success rate based on available data. Unfortunately, for many cubesat missions insufficient detail is available to be considered in our survey. Figure_6.1.2.2_1 shows the status of 66 well-documented cubesat missions.

Overall, 66% of these missions have succeeded. In 2006, 14 cubesats were destroyed due to launch failure (the launch vehicle disintegrated during launch). For the rest, the failure is resulting from a communication problem.
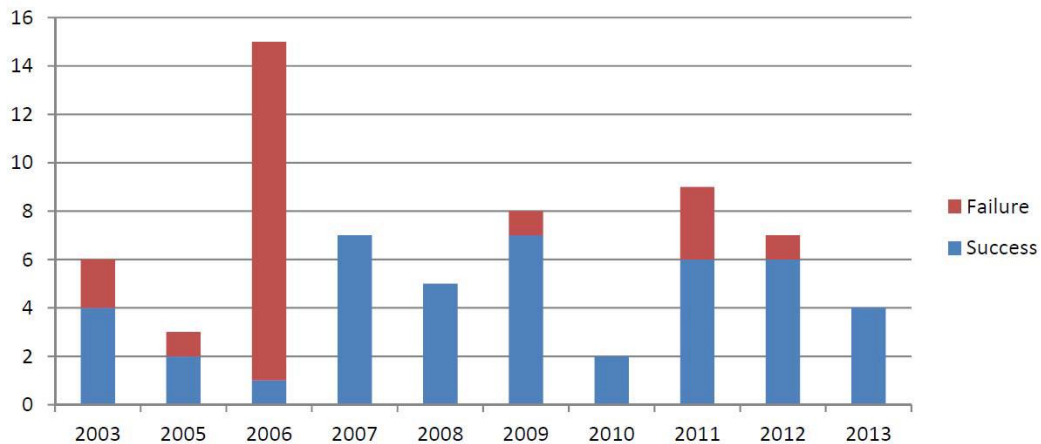
Figure_6.1.2.2_1 – *Cubesat missions success statistics.*

6.1.3   Cubesat main characteristics and specifications

The purpose of the cubesat project is to provide a standard for design of nanosatellites to reduce cost and development time, increase accessibility to space and sustain frequent launches.

Table_6.1.3_1 sums up the main characteristics of the past 10 years missions and gives us a glimpse of what can be done with cubesats.

Table_6.1.3_1 – *Summary of main characteristics of cubesat missions since 2003.*

Total mass	0,8 kg to 7,5 kg
Available power	0,3 W to 11,5 W
Total volume	1 dm^3 to 8 dm^3
Payload mass	30 % to 62,7 %
Payload power consumption	Up to 83 %
Payload volume	50 % to 60 %
Telemetry	15 bps to 256 kbps
Expected lifetime	From 21 days to 3 years
Nominal lifetime	Up to 6 years
Orbit	LEO from 350 km to 1.450 km
Development time	From 7 months to 5 years
Person assigned to the program	6 to 200

More details about cubesats and missions are available at:

- http://mtech.dk/thomsen/space/cubesat.php#3

- http://www.utias-sfl.net/nanosatellites/CanXProgram.html

- https://directory.eoportal.org/web/eoportal/satellite-missions

Following a thorough study of available COTS components and their cost and performance, we have elaborated cubesat platforms of type 1U, 2U and 3U, see Figure_6.1.3_1. This section defines the main interfaces and available resources for the payload hosted by each one of these options. The proposals for technology validation experiments should meet these specifications.
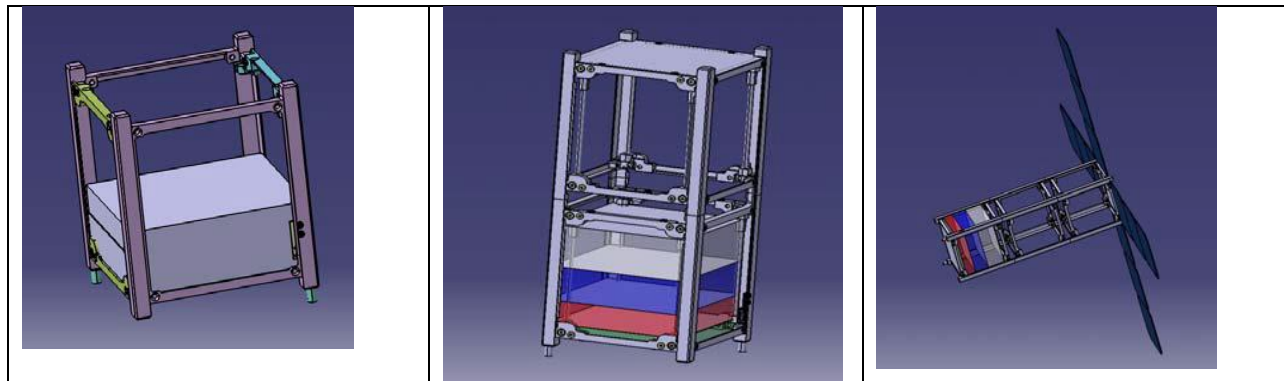
Figure_6.1.3_1 *Cubesat platforms of type 1U, 2U and 3U proposed for the FISICA study.*

6.1.4   Cubesat General and Physical Requirements

In the following are listed the cubesat geeral requirements.
- ✓ All parts shall remain attached to the cubesat during launch, ejection and operation. No additional space debris shall be created.
- ✓ Pyrotechnics shall not be permitted.
- ✓ No pressure vessels over 1.2 standard atmosphere shall be permitted.
- ✓ Pressure vessels shall have a factor of safety no less than 4.
- ✓ Total chemical energy shall not exceed 100 watt-hours.
- ✓ Total Mass Loss (TML) shall be ≤ 1.0%
- ✓ Collected Volatile Condensable Material (CVCM) shall be ≤ 0.1%

In the following are listed the cubesat physical requirements.
- ✓ Cubesat physical characteristics shall meet the specifications listed in Table_6.1.4_1.
- ✓ The cubesat center of gravity shall be located within a sphere of 2 cm from its geometric center.

Table_6.1.4_1 – *Cubesat height and mass*

	1U	2U	3U
Base	100 x 100 mm	100 x 100 mm	100 x 100 mm
Height	113.5±0.1 mm	227.0±0.2 mm	340.5±0.3 mm
Maximum weight	1.33 kg	2.66 kg	4.00 kg

6.1.5 Interface with payload and performance

In the following are listed the cubesat interface requirements parameters with the payload.
- ✓ The payload shall operate using unregulated power, 3.3V or 5.5V
- ✓ The payload characteristics shall be compliant with the specifications listed in table_6.1.5_1. These specifications derived from configurations based on off-the-shelf equipment compatible with our top level needs.

Table_6.1.5_2 gives the attitude capabilities corresponding to the chosen cubesat configurations.

Table_6.1.5_1 *Payload Characteristics*

	1U	2U	3U
Payload dimensions	98.4 x 98.4 x 44 mm	98.4 x 98.4 x 110 mm	98.4 x 98.4 x 210 mm
Payload maximum weight	390 g	1310 g	2650 g
Nominal payload power consumption	0.46 W	1.66 W	3.36 W
Peak payload power consumption	0.6 W	1.8 W	3.5 W

Table _6.1.5_2 *Cubesat Attitude Capabilities*

	1U	2U	3U
Best Attitude knowledge accuracy	5 deg	9.10^{-3} deg	9.10^{-4} deg
Best Attitude control accuracy	10 deg	6.10^{-2} deg	3.10^{-4} deg

6.1.6 Overview of the potential key technology fields

6.1.6.1 *Formation Flying*

Formation Flying (FF) is the concept of flying multiple satellites in a desired geometry to synthesize the function of a large virtual instrument. The initial FIRI proposal suggested using 3 telescopes separated by several hundreds of meters, even up to 1 km.

The scope for using Formation Flying is broad, but all formation flying missions have the following main generic features: the number of satellite is larger than one, the satellites operate in relative proximity, and relative motion control constraints must be applied to maintain the formation.

In the case of FIRI, the satellite relative motion will be determined principally by spacecraft propulsion. This type of formation is called "Non-Keplerian". The satellites are controlled autonomously on-board: the relative position and attitude are controlled in closed-loop based on relative metrology systems between the spacecraft.

A representative demonstration of FF (involving relative metrology, micro-propulsion, guidance and navigation control in closed-loop including safe deployment, reconfiguration, collision avoidance …) is clearly too demanding for any cubesat configuration.

It is worth noting that the purely technological mission PRISMA launched in 2010 has already demonstrated the capability of two satellites to operate in formation.

However, cubesats could be used to validate elementary bricks involved in the formation flying. Regarding the relative metrology, it exists typically 3 complementary classes of accuracy:

- Centimeter Class (coarse metrology): this accuracy is achieved with Radio Frequency (RF) metrology systems. Such systems have been validated (TRL9) on-board PRISMA.
- Millimeter Class (fine metrology): this metrology is achieved by using optical systems. These optical systems differ in function of the FF configuration.
- Micrometer Class (accurate metrology): this metrology is mainly achieved by laser interferometry.

All these systems are already under development and/or validation in laboratories and industries. Usually their physical characteristics are not compatible with the available resource of a cubesat.

In conclusion, except for novel elementary bricks (such as the accelerometer, see Proposal A) the use of cubesat for FF demonstration seems too challenging and not realistic in the FISICA timeframe.

6.1.6.2 Pointing and positioning

Pointing accuracy is vital for FIRI. Technology in this field is fairly advanced and it might be perceived that there is not much that a cube-sat can do to improve this with the limited Attitude Control and Positioning. An alternative form of motion could perform vital testing in prolonged microgravity conditions. Proposal B (Section 2.4.2) corresponds to this category.

6.1.6.3 Telescope dishes

FIRI will require large telescopes. There is existing heritage for specific materials in Primary and Secondary mirrors of existing and planned space telescopes. With nanosatellites, potential new mirror materials or miniaturized deployable mechanisms could be tested. However, the testing referred to here should be that which cannot be performed in a space-like environment on the ground.

6.1.6.4 Mechanisms (delay lines)

Cubesat does not offer much in terms of distance. But micro-gravity could allow a noise-test on certain mechanisms in representative conditions. The Proposal A corresponds to such a validation.

6.1.6.5 Relevant optical techniques

Space-based astronomical observations are until now done using single-dish devices. The upcoming James Webb Space Telescope (JWST) is also a single-dish telescope although the

use of segmentation introduces new problems of alignment and phasing of individual mirrors. The use of multiple-dish systems will be required in order to achieve the next step in angular resolution, beyond what can be achieved with JWSTstyle single-dish devices. Significant studies of multi-dish systems have already been done (SIM, Darwin, TPF, FIRI, …), but so far none of these concepts have been selected for construction and launch. While technological readiness of key elements like deployment, formation keeping, etc clearly constitute major risks, more conceptual issues are also seen as risk elements. Will a multi-dish system provide useful scientific images? A demonstration of a multi-dish concept, even on a miniature platform, would therefore in itself be of interest.

6.1.7   Potential candidates and context

In order to identify the appropriate payload for the nanosatellite testbed, an internal "call for Payload proposals" has been opened in the consortium. The FISICA team proposed four technical solutions that are reproduced in the next sections.

6.1.7.1   Proposal A: An accelerometer as key element of a FIRI control loop

This proposal describes the main concept of a nanosatellite testbed to demonstrate the use of an accelerometer as fundamental element of the Formation Flying control loop.

Context

The FIRI interferometer will be placed in the Lagrange point L2 and maintained in this position by means of traditional techniques of attitude control, at which will also be entrusted the task to point the telescope to the sources. In the next phase of operation of the interferometer, it will rotate around the axis passing through the sources and for its HUB (axis ILSHUB), reducing the distance between the two outer satellites telescopes ($R1(t)$, $R2(t)$), see Figure_6.1.7.1-1, so to cover the uv plane.

In a first idea the two satellites go through a spiral at a constant tangential velocity (about one meter in 25sec) with an appropriate control law that will govern the distance between the two telescopes and the rotation speed of the interferometer, so to ensure maximum coverage of the uv plane, in respect of its functionality from both the spatial and spectroscopic point of view; it is clear that also other modalities to cover the u,v plane will be considered, as for example to readjusting the satellites baseline every half turn. In L2 the dominant accelerations acting on the interferometer are essentially the inertial accelerations, determined by its rotation, in particular the centrifugal accelerations are of the order of 10^{-3} g. The measurement of these accelerations with precision 10^{-8} g, should allow the control of the system (this at least for the tethered and booms connection between the two telescopes) through the variation of the distance between the two satellites, its rotation and according to the law of conservation its momentum. The variations of these accelerations are expected at periods of about 24 hours, which represent the estimated time to walk the spiral so to cover the entire plane u, v. Also, we can underline the fact that the difference between the two measured accelerations is connected to the angular system rotation and to the distance between the two points at which the radial accelerations are measured:

$$a_d = \omega(t)^2 \cdot R(t) \text{ where } R(t) = R_1(t) + R_2(t)$$

Formula that gives the opportunity to recover the absolute distance between the two telescopes, if ω is measured (star sensors or gyroscope).
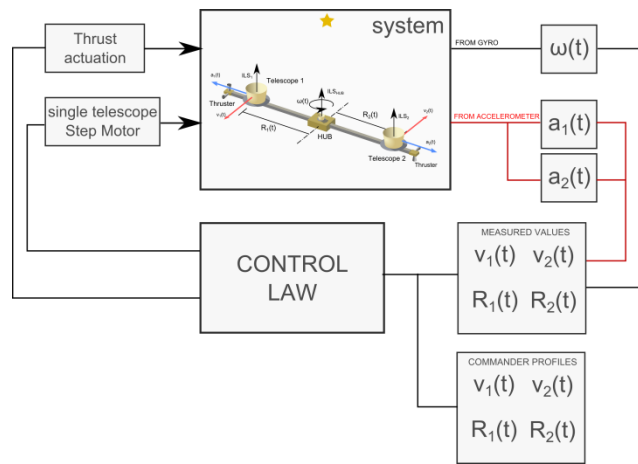
Figure_6.1.7.1-1 *Possible scheme of the interferometer control loop*.

Technology

What we propose is the test of a single sensitive axis accelerometer, which has characteristics close to those that must be obtained in the interferometric mission. In terms of signal levels, it is thought that the orbiting nanosatellite has sufficiently low noise levels, so as to verify the precision of the accelerometer, while we trust in quite "big" acceleration present in the phases of its insertion in orbit so to verify the functionality at a high level. A more complex test is to verify the frequency response of the accelerometer; due to the low power to disposition in the nanosatellite, it is not possible to use a temperature control system, so the accelerometer will have a spurious response in temperature that could mask the low frequencies accelerometric signal, to mitigate these effects the accelerometer will be accompanied with a thermometer which should allow in part the reductions of these effects. The preliminary analysis of the characteristics of the nanosatellite seems to indicate its suitability for this test, both for the mechanical and electrical interfacing point of view.

In Table_6.1.7.1-1 are reported the characteristics of the single axis accelerometer, while in Figure_6.1.7.1-2 are reported its mechanical and its electrical parts.

Sensitivity	da 1e-7 a 1e-8 g/sqrt(Hz)
Acquisition frequencies (Hz)	0.1,0.2,0.5,1,5,10,20,50,100
Output	Analogic or digital
Data rate (10Hz one acc. And one T) [byte/s]	250
Internal thermometer Pt10000	Precision better than 10^{-4} °C
Interface of communication	RS232 full-duplex/ RS485 (with adaptor)
Standard of communication	NMEA
Dimensions of a single axis mechanical element	80 x 60 x 25 (H x L x A)
Electronic dimensions for a single element [mm]	75X55X12
Voltage supply via USB or external [V]	5
Power dissipation	75 mW
Weighs [Kg]	0.200
Linearity	> 80 dB
Internal memory	SD 2Gb

Table_6.1.7.1-1 – *Single axis accelerometer characteristics*.
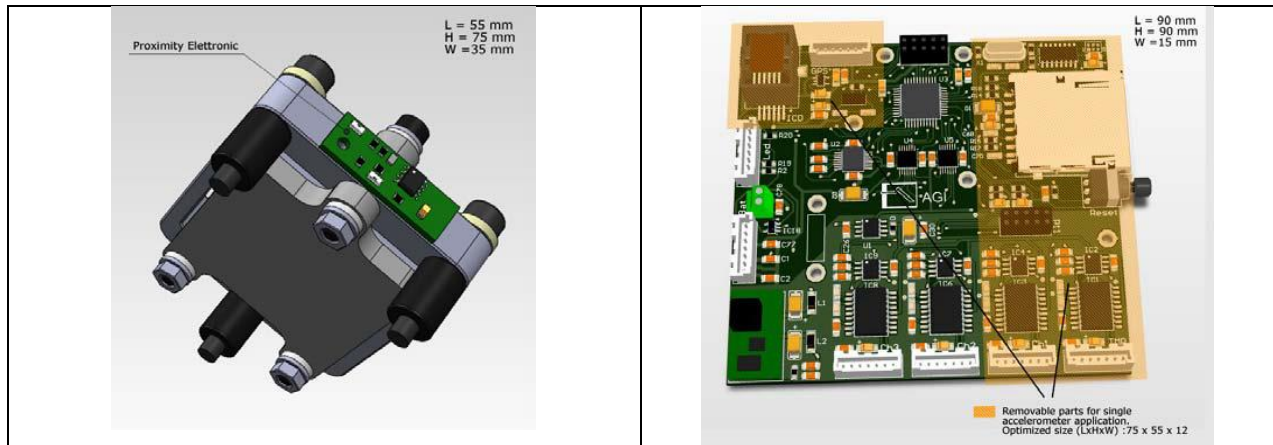
Figure_6.1.7.1-2 *LEFT: Mechanical part of the accelerometer. RIGHT: Electronic part of the accelerometer.*

Interfaces for the accelerometer and the cubesat

Here below are reported the entire interface between the accelerometer element implemented and the nano-satellite. All the interfaces have been implemented togheter with the mechanical and electronic parts.

Electrical interface

Power supply		Requirement
Voltage	5 V	
Current	<30 mA	
Power	<150 mW	<200 mW

Data Interface

Data Interface	
Type	Serial Asynchronous
Standard	RS232 or TTL (if compatible with CSP, see below)
Data Rate	>19200 baud
Parity	N
Data bit	8
Stop bit	1
Encoding	ASCII

Connector

Requirement:
2 different connectors
1. electrical power,
2. data transfer.
Standard: PC/104 pin connectors like SAMTEC ESQ-126-49-G-D or compatible.

Data Protocol

Required: Cubesat Space Protocol (CSP)
References:

➢ http://en.wikipedia.org/wiki/Cubesat_Space_Protocol
➢ https://github.com/GomSpace/libcsp
➢ https://code.google.com/p/cubesat-space-protocol/source/browse/libCSP/trunk/include/csp/csp.h

Scientific Data Rate

The data rate depends on the sampling frequency that should be at least 1 Hz. Some examples are shown in the following table.

Scientific Data Rate Example			
Bytes per sample	Sampling frequency (Hz)	Byte per second (B/s)	bit per second (bps)
33	1	33	264
33	2	66	528
33	10	330	2640
33	20	660	5280

Weight

Weight	Requirement
320 g	<300 g

Mechanical interface

In the following figures the drawing of the one-axis accelerometer, mechanically interfaced with the cube-sat is shown.
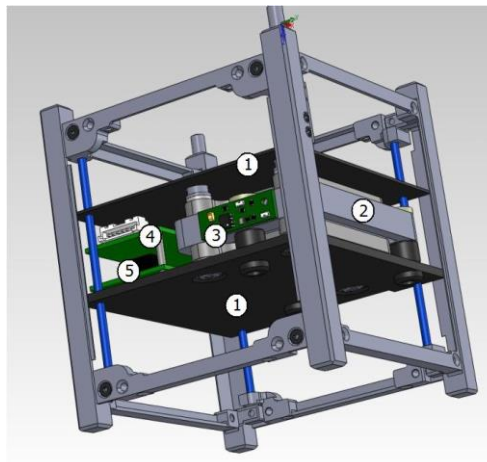
Figure_6.1.7.1-2 *Mechanical interface of the accelerometer with the cub-sat structure unit.*

The main elements are:
1) the supporting plates on the top and on the bottom of the accelerometer;
2) the sensor;
3) the electronic pre-amplifier for the accelerometer;
4) the analog electronics;
5) the digital electronics.
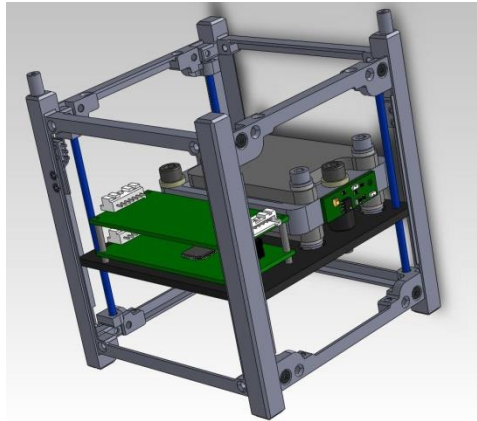
Figure_6.1-7.1-3 *Mechanical interface of the accelerometer with the cub-sat structure unit, without the support plate.*
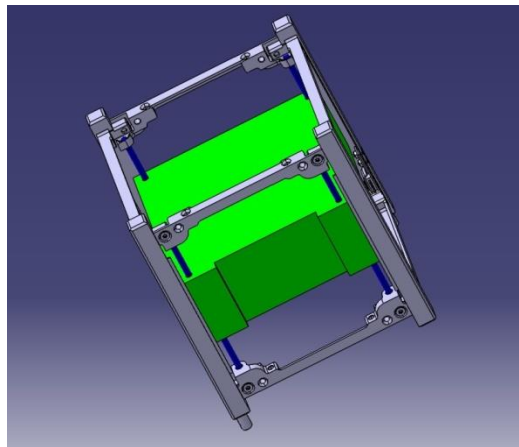
Figure_6.1.7.1-4 *Mechanical interface of the accelerometer with the cub-sat structure unit, with the indication in green of the space dedicated to it.*

In the figure_6.1.7.1-5 is shown the drawing of the mechanical interface, that reports the dimensions.

Figure_6.1.7.1-5 *Drawing of the mechanical interface, that reports the dimensions.*

To seen the DEL_2.5/6 for the description of the on ground experimental tests.

6.1.7.2   Proposal B: Thermal emission/absorption steering

Rationale
ETE-Enhanced Thermal Emission could be considered as a viable means for microsteering when produced at the extremities of a long connected structure and in opposite directions.

The scope is to attempt to micro-steer by controlling the temperature and/or the emission of purposely defined satellite surfaces.

Relevance

Long baseline structures requiring micro-pointing corrections could benefit by applying small amounts of torque to the structure via differential radiative emission (or differential response to photon pressure). This could produce non-negligible savings in the consumption of hydrazine (commonly used for spacecraft steering). The latter is the most efficient propellant and is also a very dangerous and toxic substance which has been on a list for both ESA and NASA for research of a suitable alternative due risks in its preparation.

Method/Technique

Different locations in space are subject to different amounts of solar wind and Sunrelated photon pressure. While in Pioneer-like surroundings thermal emission might be the dominant source of non-gravitational acceleration, in L2 and more so in LEO this will not be the case. To study the effects of variations in thermal emission with the purpose of specific accelerations the cube-sat should be designed in a way to either strike a balance between the solar photon pressure, the Earth's thermal emission and the cube-sat self-emission, or to make sure such contributions can be differentiated.

The cube-sat is placed in a decaying orbit so there will be virtually no control on satellite trajectory and the acceleration will be constantly varying, but a 2U or a 3U (which offers a higher degree of attitude accuracy) could perform tests where we attempt to impart angular momentum along an axis orthogonal to the cubesat elongation (lower energy required). If electro-chromia (property of changing color by application of an electric field) is achieved (even minimally), differential acceleration could be measured with respect to solar photon pressure (on the dayside) and due to combined thermal emission/absorption of Earth thermal emission (on the night side).

There are two main ways in which this could be attempted: controlling either the surface temperature or the surface emission (or both). Ultimately both techniques will require power. Post-launch the satellite will begin thermalization and this will be modelled accurately in order to account for this as well as for the decaying orbit acceleration. Surface temperature can be easily controlled by active Joule dissipation while surface emissivity is more challenging. A "simple" active mechanism that allows a single (IR black/white) panel rotation would produce maximal effect. The scenario where small versions of such a mechanism are placed on a more complex satellite is not as attractive due to the added complexity of many small moving parts. An alternative is an IR version of electro-chromia which could have interesting applications per sec.

Orders of magnitude of the effects

1-Solar photon pressure: Given the solar constant and an area of exposure of the two panels of interest (at the sides of a 3U) of A=0.01 cm2 each, the momentum imparted to such panel from the solar photon pressure is 5e-8 Ns on absorption and twice that on total reflection. Hence if we assume that we have a starting emissivity of 0.5 on two panels and that we can electronically alter these by only 0.1 in opposite ways (0.4 vs 0.6), we will obtain a torque of ~10-9 Nm (for 1kg units). Application of this torque for 10 minutes should produce a rotation of the unit of ~5 arcminutes which is easily monitored within the pointing accuracy and control.

2-Thermal emission from Earth: Calculations using an Earth blackbody radiative temperature of ~230K shows a photon pressure generally a factor 10 smaller with respect to contribution #1. While this is measureable, a general homogeneity in the cubesat panels facing Earth should allow us to neglect this effect.

3-Controlled Emission via Joule dissipation: Assume that a panel is mounted (Figure 7, right) with a weak thermal link to the cube-sat and that we can dissipate 1W of Joule power relatively uniformly (this can be achieved using a thin graphite sheet glued on a layer of printed electronic dissipators. Given the numbers in appendix for the structure and weight of the panel, a differential temperature of ~20K should be achieved between a satellite T of 250K and the panel which could provide a torque between a factor 5 and 10 smaller than that of case #1. This could hence be easily tested by having homogeneous emissivity on all panels (thereby cancelling most of #1 and #2) and applying such power.

4-Atmospheric drag: This is by far the strongest force acting on the satellite with the worst case imparting an estimated 10uN at a 300km orbit. This is 3 to 4 orders of magnitude greater than the momentum created by photon pressure or emission.

While a specific calculation will depend on the actual entire structure geometry, this will be an almost constant force which should not vary on short time constants and could be hence separated when monitoring the units' position and orientation.
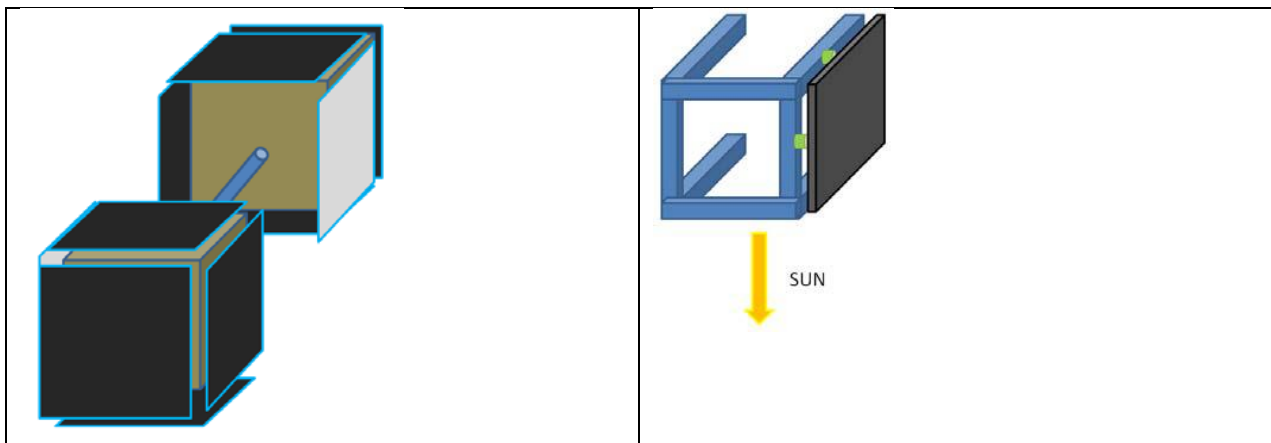
Figure_6.1.7.2-1 *LEFT: A 3U concept (for maximum AC and sensitivity to torque) where the surface emissivity (either controlled or pre-established) is purposely asymmetric to generate torque on the structure via either photon absorption/reflection or thermal emission. RIGHT: A single panel is heated to produce differential thermal emission and impart torque (note: all faces of cube would identical panels to balance photon pressure from both Sun and Earth).*

Technology

Temperature control is substantially easier as it involves the use of printed electronic circuits which can be glued/mounted at the back of high-emission panels (graphite or IR-black on thin metal panels). These can be driven with moderate power sources (solar?). Emissivity control, as mentioned, is trickier and specific materials should be investigated.

6.1.7.3 Proposal C: A thermal interferometer for Earth Observing

The exploitation of the interferometric beam-combination to improve the angular resolution can take many forms. In this case, given the low sensitivity that a small and relatively cheap camera can offer, a thermal imaging camera could be pointed towards the ground (Earth) while receiving combined beams from two apertures.

Scope

Proof that this technique is viable in the thermal infrared could open the possibility (given sufficiently fast detectors) to design a future satellite of modest size but with extendable arms (and small dishes at the extremities) to provide high-spatial thermal resolution on the ground without having to resort to extremely large dishes.

Method

A 3U would be necessary for this concept: with two small collecting optics on each of the external units and the camera core in the center one. (see Figure_6.7.3-1). Simple scanning of the satellite pointed to the ground should provide sufficient information to allow collection of data with a synthesized beam with a factor of 10 greater than if the camera lens ~2cm were pointed at the ground.

Technology

Among the issues with this proposal is the need for a pressurized central part (for the camera and electronics), data rate transfer (most commercial cameras 120x160 or 240x320 have a 30Hz acquisition with an 8 bit dynamic range). The latter suggests a data rate short of 20Mb/s... so we could decide to reduce the portion of camera read to a small amount of pixels (20x20) for a 100kbit/s.
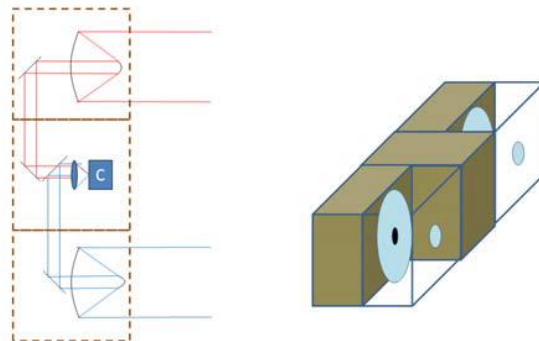
Figure_6.1.7.3-1 *Concept diagram of how a dual input synthetic interferometer 3-Unit cubesat would look like. The camera core and optics (C) could also be replaced by a single MIR or LWIR photodiode if the complexities of the design are excessive.*

6.1.7.4 Proposal D: Hypertelescope

We propose to build an extremely simple nano-satellite demonstrator of what a multiaperture imaging interferometer could achieve. Apart from one of the high-precision guiding probe on the Hubble Space telescope, it would, to the best of our knowledge, be the first ever space-borne interferometer.

Concept of multi-aperture interferometer

While a dual aperture (2A) system is at first glance less complex than a triple (3A) or more (nA) system, the requirement for full imaging capabilities sets much more stringent performance requirements, hence complexity and cost, to a 2A system.

Indeed, while 2A systems require absolute measurement of pupil geometry to quarter wave accuracy (order of a micron for a 10μm system), in a 3A or more systems, which can deduce this absolute knowledge from the scientific measurements themselves thanks to the closure phase, requirements for absolute pupil geometry control is reduced to the order of Rλ where R is spectral resolving power and λ is wavelength.

For R=1000 at λ=10μm, the pupil geometry controlled requirement is of the order of a cm, hence significantly reducing system complexity.

Multi-pupil interferometric recombination systems can become extremely complex, but this is not necessarily the case. The hyper telescope recombination scheme, following the original idea proposed by Labeyrie (A&A 1996), where all pupils are brought to interfere in a common focal plane creating a complex two-dimensional interference pattern, provides a simple and efficient recombination scheme without the use of beam splitters. Individual apertures, in the form of reflectors carried by freeflying or structurally interconnected spacecrafts located on a curved surface, can focalize light towards a common focus where the interference pattern is recorded using a bi-dimensional detector array. The focal plane spacecraft could potentially just contain a detector, but will in practice contain beam collection and exit-pupil arranging optics. The hyper telescope exit pupil does not need to reproduce its entrance pupil. In particular, the exit pupil could be densified, as in Labeyrie's original proposal (and in Michelson's famous experiment). In a scheme appropriate for a general imaging facility like FIRI, we believe the entrance pupil should be fully redundant, allowing for as many u-v points as possible to be collected in a single image. Making the pupil geometry evolve over time, the u-v plane for a given instrument pointing would be built up during the course of the observation.

Nanosat configuration

We propose to construct a nano-satellite version of a FISICA hypertelescope. To simplify, we would avoid free-flyers by selecting an object that can be observed with sufficiently small baselines to fit all in a small box: the Sun. Observed at 10μm, the sun is unresolved by millimetric apertures and resolved by a decametric aperture. The concept would consist of a 100mm-baseline hypertelescope composed of, seven 1mm diameter apertures feeding an infrared array detector. This would provide 21 baselines per image.

This system would fit into a 3U cube sat, with one unit for the telescope, one unit for the detector system (a Nano640E un-cooled array), and one unit for the satellite functions. A simpler option could consist of a visible webcam with a scaled-down aperture mask in front of it, essentially 0.1mm holes for a 10mm diameter telescope.

This could possibly fit into a 1U cubesat.

The system would demonstrate fringe stability and capacity to record and combine baselines to reconstruct an image. A parallel camera could be implemented to record real images simultaneously (on the same detector) for reference. We could possibly also implement a second interferometer channel with only two apertures, allowing a comparison of the two interferometer concepts.

Basic interferometric considerations

We consider a 7-aperture system to observe the Sun from Earth orbit at 10μm. We choose aperture size (D) in order to not resolve the sun (full sun within the aperture main diffraction lobe FWHM). Hence, for $\lambda/D = 0.5°$, D = 1.14mm. We fix D=1mm.

The size of the nanosat fixes our baseline to B=100mm, allowing a final resolution element 100 times smaller. The total number of resolution elements on the sun surface is therefore (B/D)^2 π/4 = 7900.
a b c d
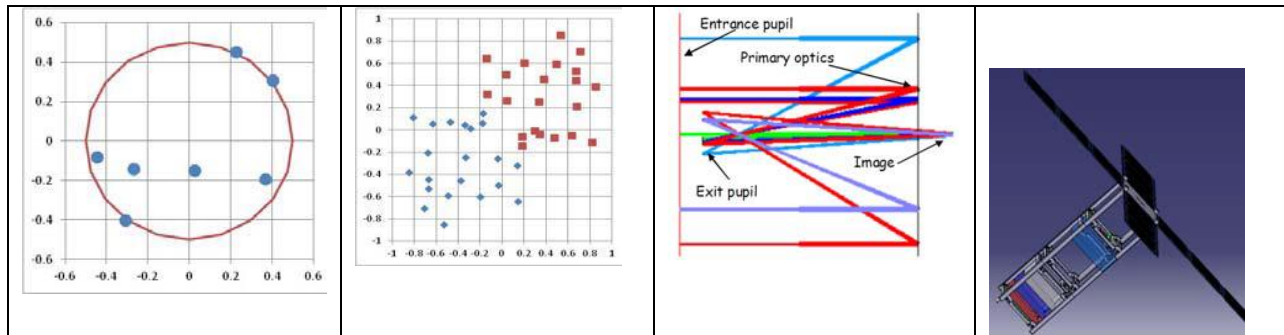
Figure_6.1.7.4-1 a) *Proposed aperture distribution. b): Instantaneous u-v plane coverage. c): First-cut raytracing of the HyperCube. d): First-cut mechanical design in a 3U CubeSat.*

Entrance Pupil Arrangement
An n-aperture, non-redundant pupil provides N=n(n-1)/2 baselines. Our n=7 system therefore gives N=21 baselines in a snapshot. We can arrange the pupils in such a way as to make sure no two baselines are equal, and that they sample evenly the baselines from an inner minimum baseline b to the maximum baseline B. If we assume a polar orbit allowing pointing the sun during a complete orbit, stabilizing the satellite such that one of its sides always faces the earth then gives a rotation of the entrance pupil with respect to the sun of 360° in typically 1.5h, providing a full coverage of the u-v plane. For B=100mm and b=20mm, the N=21 baselines give a radial sampling of (B/b)/(N-1)=4mm. One possible aperture distribution is shown in Figure 9 (a).

Exit Pupil Arrangement
Several options can be taken for the exit pupil arrangement. The simplest option is to do nothing, in which case the longest baseline will produce 100 fringes across the unresolved solar image. If all the apertures are perfectly phased this arrangement may give some kind of image of the solar disk. In the absence of phasing, just making sure optical paths are coherenced, ie within the coherence length $L = \lambda 2/\Delta\lambda = R\lambda$, The image will be a collection of some 7900 speckles from which the u-v plane information (21 visibilities and phases) can be retrieved by Fourier analysis. Retrieving this information requires at least four detectors per speckle, ie an array of 200x200 detectors.

We can reduce the number of speckles, hence detectors, in the image by densifying the pupil: increasing the size of each individual pupil relative to their separation reduces the size of the unresolved image while maintaining the fringe spacing. The optimal amount of densification must be determined through end-to-end modelling which will be done in collaboration with UCL. The main parameter here is detector noise, see estimation below. We consider an exit pupil densified by a factor 5, reducing the number of detectors to 40x40 = 1600.

We can also rearrange the aperture pattern: as long as both entrance and exit pupils are redundant we can recover the on-sky u-v points after Fourier analysis of the recorded image. In our case, where we need 7 optical elements precisely positioned in the 20mm

diameter exit pupil, we propose to place the apertures regularly spaced on a circle, hence optimizing space while remaining non redundant. There is also a choice to be made between pupil-plane and image-plane recombination; to be further studied.

Detector and preliminary power budget

We propose to use the ULIS Nano640 un-cooled bolometric array with 640x480, 25μm pixels. This array, while never flown, is space qualified by CNES in preparation for missions such as Marco Polo-R. It provides a noise equivalent temperature difference at 300K of NETD<60mK, which corresponds to a noise equivalent power of some 20pW. For our 40x40-detector images, we therefore collect a total noise power of 0.8nW. Observing the sun from earth orbit at 10μm with a 10nm wide filter (R=1000) through 7 holes of 1mm diameter we collect a total of 30nW. As a first-order design this appears reasonable, but further analysis and optimization will be performed in the early design phase.

6.1.8 Critical analysis

Each proposal (A to D) described in Sections 2.4.1 to 2.4.4 have been rated using the following criteria:

· Interest for FISICA (weight 4): either directly applicable (e.g. interferometry techniques, formation flying, …) or strongly relevant (e.g. pointing stability, noise issues, …);

· Novelty (weight 3)

· Technological Readiness Level (TRL) gain (weight 3): this excludes the novelty but includes the potential industrial gain.

· Scientific interest (weight 2): by scientific here we refer mainly to astronomical or observational data prodcuts.

· Feasibility (weight 3)

Table_6.1.8-1 summarizes the evaluation of each proposal.

Table_6.1.8-1 Proposals rating

Table 6 – Proposals rating

	Weight	Proposal A: Accelerometer	Proposal B: Steering for thermal absorption/emission	Proposal C: Interferometer for Earth Observation	Proposal D: Hypertelescope
Interest for FISICA	4	2	2	2	2
Novelty	3	2	3	3	3
TLR gain	3	3	2	2	3
Scientific interest	2	1	1	2	3
Feasibility	3	1	2	1	2
TOTAL		28	31	30	38

Proposal A is interesting since it intends to validate a key technological brick (the highprecision accelerometer) involved in the formation flying control loop. However, our current knowledge on the operational conditions (orbits, stabilization, and thermal stability) is not sufficient to guaranty the complete validation of the accelerometer with the nanosat platform. Indeed, orbits and attitude that can be achieved will generate both low and high frequencies disturbing the output of the accelerometer.

Furthermore, the thermal environment will not be stabilized and the accelerometer will be affected by these temperature variations (then adding another noise).

Therefore, a nanosatellite fully dedicated to the validation of the accelerometer seems too risky at this time.

Proposal B intends to demonstrate a promising method based on thermal emission for fine navigation while avoiding mechanical moving parts and combustion-based systems. The proposed payload is quite simple and could fit in 1U (even if the 3U configuration is preferred to enhance the torque effects).

Proposal C describes a thermal interferometer observing Earth. This payload is not complex except for 1) the optical path which has to be accurately maintained since the temperature will not be controlled in the nanosat; and 2) the camera which has to be pressurized.

Proposal D is the most interesting for both its capacity to provide a very first demonstration of space-based interferometric imaging; and its feasibility within the nanosatellite constraints. This payload is simple, mature and does not require stringent operational conditions.

It is worth noting that there would be sufficient volume, weight, and power allocations within a 3-unit cube-satellite to include the accelerometer (Proposal A) within the nanosatellite. This would also optimize the mission profile, since the current Proposal D would need very little observing time (essentially one orbit) while it would require a long lifetime for data transmission. The concept would therefore allow for long-term measurements of accelerometric data, and allow for the use of on-board navigation capacities already present on the platform in order to provide stability and controlled excitation movements of the satellite.

6.2   CONCLUSIONS AND FUTURE STEPS

The performed activity demonstrate that a nanosatellite can be a suitable element to perform demonstration experiments capable to increase the technological readiness levels of elements usefull for applications in FIR interferometer space missions. In particular, a single, 2-unit cube satellite was found appropriate to provide an optimal mission concept for the combination of the proposals before described in the points D and A.

The on-ground experiments used a low-cost CubeSat platform for the technology validation is space. The experiments are based on a two-unit (2U, 10x10x20 cm^3) CubeSat allowing the validation of a high-performance accelerometer and the implementation of the first ever space-borne imaging interferometer.

To validate the accelerometer, it is mounted at the extremity of a well-balanced 2U CubeSat for which the rotation can be controlled by a reaction wheel in such a way as to provide a controlled variation in centrifugal acceleration. The ground-based demonstration of this concept is achieved by hanging the CubeSat in a string, simulating weightlessness in a plane with negligible friction. The experiment allowed verification of the measurement concept and the dimensioning of the reaction wheel.

The interferometer is an aperture masking Fizeau interferometer simulating a future multi-aperture space interferometer possibly based on formation flight technology. Preliminary dimensioning of this miniature interferometer allowing for measurement of solar radius and limb-darkening, for which an aperture size of 10 μm and maximum baseline of 0.5mm is appropriate, shows that it can easily fit as a second payload within the 2U CubeSat. With pointing requirements of the order of 1 degree, navigation requirements are also within reach of off-the-shelf CubeSat technology. The ground-based demonstration experiment,

based on the use of a CCD camera with a masked objective mounted on a sun-tracking telescope mount, has proven capable of producing high-quality interferometric images. It has also demonstrated the use of such a miniature interferometer for determination of solar parameters such as radius and limb-darkening function. Further study of this concept could lead to a proposal to its use as a high-quality solar monitoring instrument.

7 REFERENCES

[1]   Mariotti J.-M., Ridgway, S.T. Double Fourier spatio-spectral interferometry – combining high spectral and high spatial resolution in the near infrared. A&A 195, 350, 1988.

[2]   ESA report, "FIRI, Far Infrared Interferometer," ESA CDF Study Report CDF-49(A) (2006).

[3]   Savini G, "Far Infra-red Space Interferometer Critical Assessment: Scientific Definition and Technology Development for the Next Generation THz Space Interferometer" Periodic Review , (2014)

[4]   Stahl HP., Sumrall P., Hopkins "Ares V launch vehicle: An enabling capability for future space science missions" Acta Astronautica, Volume 64, Issue 11, p. 1032-1040. (2009)

[5]   Stute T. "The Planck Telescope Reflectors" Astronomical Structures and Mechanisms Technology, , Proceedings of SPIE Vol. 5495 (SPIE, Bellingham, WA, 2004)

[6]   Swinyard B, Nakagawa T, "SPICA: A Joint JAXA/ESA Mission to Discover the Origins of Galaxies, Stars and Planets",

[7]   Stahl H. P. "JWST mirror technology development results ", Proc. SPIE, 6671, 667102 (2007)

[8]   http://research.uleth.ca/spica/documents/pdf/SPICA%20Cosmic%20Vision%202015%20Print%20Copy.pdf (2009)

[9]   Tauber J., "Planck pre-launch status: The optical system". A&A Volume 520, (2010)

[10]   "ESA pointing error engineering handbook", http://peet.estec.esa.int/files/ESSB-HB-E-003-Issue1(19July2011).pdf

[11]   FISICA deliverable D1.2

[12]   Harwitt M. et al, "Submillimeter Probe of the Evolution of Cosmic Structure" SPECS (2005).

[13]   Rinehart S. and the SPECS mission study team "SPECS: The Submillimetre Probe of the Evolution of Cosmic Structure." (2006)

[14]   Wilson M.E. et al. "The Space Infrared Interferometric Telescope (SPIRIT): Optical System Design Considerations" (2007)

[15]   Amato M., Benford D.J., Moseley S.H., Roman J. "An engineering concept and enabling technologies for SAFIR", in: Mather, J.C. (Ed.), IR Space Telescopes and Instruments. Proc. SPIE, vol. 4850. SPIE – The International Society for Optical Engineering, Bellingham, WA, pp. 1120–1131, 2003.

[16]   Blain A. "SCUBA deep fields and source confusion", in: Cristiani, S., Renzini, A., Williams, R.E. (Eds.), ESO/ECF/STScI Workshop Proc. Deep Fields. ESO Symp. Series, vol. xxvi. Springer, Berlin, pp. 129–134, 2000.

[17]   Evans N.J. Physical conditions in regions of star formation. Annu.Rev. Astr. Astrophys. 37, 311–362, 1999.

[18]   Evans, N.J., II, Star and planet formation studies with new generation Infrared telescopes. BAAS, 33, 910, 2001. Available from < http://space.gsfc.nasa.gov/astro/aasbeyond/evans >.

[19]   Haiman Z., Rees M.J., Loeb A. H2 cooling of primordial gas triggered by UV irradiation. ApJ 467, 522–531, 1996.

[20]   http://www.eso.org/projects/alma

[21]   Kogut A., Spergel D.N., Barnes C., Bennett C.L., Halpern M., Hinshaw G., Jarosik N., Limon M., Meyer S.S., Page L., Tucker G.S., Wollack E., Wright E.L. First year Wilkinson Microwave Anisotropy Probe (WMAP) observations: temperature polarization correlation. ApJS 148, 161–173, 2003.

[22]   Leisawitz D.T., Danchi W.C., DiPirro M.J., Feinberg L.D., Gezari D.Y., Hagopian M., Langer W.D., Mather J.C., Moseley S.H., Shao M., Silverberg R.F., Staguhn J., Swain M.R., Yorke H.W., Zhang X., "Scientific motivation and technology requirements for the SPIRIT and SPECS far-infrared/submillimeter space interferometers", in: Breckinridge, J.B., Jakobsen, P. (Eds.), UV, Optical, and IR Space Telescopes and Instruments. Proc. SPIE, vol. 4013. SPIE – The International Society for Optical Engineering, Bellingham, WA, pp. 36–46, 2000.

[23]   Leisawitz D., Armstrong T., Benford D., Blain A., Borne K., Danchi W., Evans N., Gardner J., Gezari D., Harwit M.,Kashlinsky A., Langer W., Lawrence C., Lawson P., Lester D.,Mather, J., Moseley S.H., Mundy L., Rieke G., Rinehart S., Shao M., Silverberg R., Spergel D., Staguhn J., Swain M., Traub W., Unwin S., Wright E., Yorke H., "Probing the invisible universe: the case for far-IR/submillimeter interferometry", in: Benford, D.J., Leisawitz, D.T. (Eds.), Second Workshop on New Concepts for Far-Infrared and

Submillimeter Space Astronomy, NASA CP-2003-212233. NASA, Washington, DC, pp. 166–176, 2003a. Available from <http://xxx.lanl.gov/abs/astro-ph/0202085>.

[24] Leisawitz D., Frey B.J., Leviton D.B., Martino A.J., Maynard W.L., Mundy L.G., Rinehart S.A., Teng S.H., Zhang X. "The Wide-Field Imaging Interferometry Testbed I: purpose, testbed design, data, and synthesis algorithms", in: Shao, M. (Ed.), Interferometry in Space, Proc. SPIE, vol. 4852, pp. 255–267, 2003c.

[25] Mather J.C., Moseley Jr., S.H., Leisawitz D., Dwek E., Hacking P., Harwit M., Mundy L.G., Mushotzky R.F., Neufeld D., Spergel D., Wright E.L. "The Submillimeter frontier: a space science imperative". Rev. Sci. Instr. (submitted). Available from <http://xxx.lanl.gov/abs/astro-ph/9812454>.

[26] Leisawitz D., Benford D.J., Kashlinsky A., Lawrence C.R., Mather J.C., Moseley S.H., Rinehart S.A., Silverberg R.F., Yorke H.W. "Prospecting for heavy elements with future far-IR/submillimeter observatories, in: Woodward, C. (Ed.), The Heavy Element Trail From Galaxies to Habitable Worlds". Astronomical Society of the Pacific, San Francisco, CA, 2003b (in press).

[27] Mather J.C et al., "The Submillimeter Frontier: A Space Science Imperative," Astrophysics 1998, astroph/9812454.

[28] http://emits.sso.esa.int/emits-doc/ESTEC/Invitation-to-ESA-Technology-Workshop.pdf

[29] Neugebauer G. et al., The Infrared Astronomical Satellite (IRAS) mission, ApJ, 278, L1-L6, 1984.

[30] Kessler M.F. et al., The Infrared Space Observatory (ISO) mission, A&A, 315, L27-L31, 1996.

[31] Gardner J.P. et al., The James Webb Space Telescope, Sp.Sci.Rev., 123, 485-606, 2006.

[32] Brown R.L., Wild, W., and Cunningham, C., ALMA – The Atacama Large Millimeter Array, Adv.Sp.Res., 34, 55-559, 2004.

[33] Pilbratt, G.L., Herschel Space Observatory mission overview, in J.C. Mather (ed.), IR Space Telescopes and Instruments, Proc. SPIE, vol. 4850, 586-597, 2003.

[34] Becklin E.E., Stratospheric Observatory for Infrared Astronomy (SOFIA), Adv.Sp.Res., 36, 1087, 2005

[35] Kamp I., Dullemond, C.P., Hogerheijde, M., and Enriquez, J.E., Chemistry and line emission of outer protoplanetary disks, in Astrochemistry: Recent Successes and Current Challenges, Proc. IAU Symp. 231, eds. D.C. Lis, G.A. Blake & E. Herbst (Cambridge: Cambridge Univ. Press), 377-386, 2005.

[36] van Dishoeck E.F. and Hogerheijde, M.R., Models and observations of the chemistry near young stellar objects, in The Origin of Stars and Planetary Systems, eds. C.J. Lada and N.D. Kylafis (Kluwer Acad. Pub.), 97-141, 1999.

[37] Kuchner M.J., and Seager, S., Extrasolar Carbon Planets, ApJ, submitted, 2005. Available from <http://arxiv.org/abs/astro-ph/0504214>.

[38] de Graauw Th., and Helmich F.P., "Herschel-HIFI: The Heterodyne Instrument for the Far-Infrared", in The Promise of the Herschel Space Observatory. eds. G.L. Pilbratt, J. Cernicharo, A.M. Heras, T. Prusti, & R. Harris, ESA-SP 460, 45-51, 2001.

[39] Frank P. Helmich · R. J. Ivison FIRI—A far-infrared interferometer Exp Astron

[40] DOI 10.1007/s10686-008-9100-2

[41] De Graauw Th., Helmich F.P. et al., "Herschel-HIFI: the heterodyne instrument for the far-infrared", in Pilbratt, G.L., et al. (eds), Proc. of The Promise of the Herschel Space Observatory, 12-15 Dec 2001, Toledo, Spain, ESA-SP460, pp. 45-51, 2001.

[42] Miller D., Saenz-Otero A., Wertz J., Chen A., Berkowski G., Brodel C., Carlson S., Carpenter D., Chen S., Cheng S., Feller D., Jackson S., Pitts B., Perez F., Szuminski J., Sell, S. "SPHERES: a testbed for long duration satellite formation flying in micro-gravity conditions", in: Proc. AAS/AIAA Space Flight Mechanics Meeting, Clearwater, FL, paper 00–110, 2002. Available from <http://ssl.mit.edu/spheres/library/AAS-AIAA.pdf>.

[43] Rupp et al, "Autonomous formation flying at DLR's German Space Operations Center (GSOC)" 58th International Astronautical Congress, Hyderabad, India (2007)

[44] Delpech et al, "Results of PRISMA/FFIORD extended mission and applicability to future formation flying and active debris removal missions" 5th SFFMT, DLR, Munich, 2013

[45] Leisawitz et al, "The Space Infrared Interferometric Telescope (SPIRIT): A Far-IR Observatory for High-resolution Imaging and Spectroscopy," Decadal Survey White Paper (2010).

[46] Reinhart et al, "The Balloon Experimental Twin Telescope for Infrared Interferometry (BETTII): An Experiment for High Angular Resolution in the Far-Infrared," PASP (2014).

[47] Wild W., Th. de Graauwa, Barysheva A., Baselmans J., Bosb A., Gao J.R., Gunst A., F. Helmich, ter Horst R., Jackson B., Koshelets V.P., Maat P., Noordam J., Roelfsema P., Venema L., Whyborn N., and Yagoubov P. "ESPRIT (Exploratory Submm-Interferometric Space Radio Telescope)" 18th International Symposium on Space Terahertz Technology

[48] Chung, S-J., Adams, D., Saenz-Otero, A., Miller, D.W., Leisawitz, D., Lorenzini, E., and Sell, S. SPHERES tethered formation flight testbed: advancements in enabling NASA's SPECS mission, in J.D. Monnier, M. Scholler, and W.C. Danchi (Eds.), Advances in Stellar Interferometry, Proc. SPIE, vol. 6268, 62680B1-13, 2006.

[49] Harwit M., et al.: Kilometer-Baseline, far-Infrared/Submillimeter Interferometer Vision Mission. Final Report, submitted to NASA, (2005)

[50] Nolet S., Kong, E., and Miller, D.W., "Autonomous docking algorithm development and experimentation using the SPHERES testbed," SPIE Defend and Security Symposium, 1315 April 2004, Orlando, FL.

[51] Farley R.E., Quinn D.A. Tethered formation configurations – meeting the scientific objectives of large aperture and interferometric science, in: Space 2001. American Institute of Aeronautics and Astronautics, Paper 2001-4770 (AIAA Accession number 39913), 2001.

[52] Lorenzini E., Bombardelli C., Cosmo M., Harwit M., Leisawitz L., Farley R., Rinehart S., Quinn D., Miller D., "Far-Infrared/Submillimeter Astronomical Interferometry with Spaceborne Tether Formations," Astrophys Space Sci (2006) 302:225–239 DOI 10.1007/s10509-006-9038-7

[53] Bainum P. M., Harkness R. E., Stuiver W., "Attitude Stability and Damping of a Tethered Orbiting Interferometer Satellite System," Journal of Astronautical Sciences, Vol. 19, p.364 (1972)

[54] Decou A. B., "Tether static shape for rotating multimass, multitether, spacecraft for 'triangle' Michelson interferometer," Journal of Guidance, Control, and Dynamics (ISSN 0731-5090), vol. 12, Mar.-Apr. 1989, p. 273-275. (1989).

[55] Bombardelli C., Lorenzini E.C., Quadrelli M.B., "Retargeting Dynamics of a Linear Tethered Interferometer," Journal of Guidance, Control, and Dynamics, vol. 27, issue 6, pp. 1061-1067 (2004).

[56] Kumar K. D., Yasaka T., "Rotation Formation Flying of Three Satellites Using Tethers," Journal of Spacecraft and Rockets, vol. 41, issue 6, pp. 973-985 (2004)

[57] Lorenzini E. C., "Large Tether-Connected Two-Dimensional Structures in Low Earth Orbit," Proceedings of the Pacific Basin International Symposium on Advances in Space Science Technology and its Applications, pp. 792-800, 7-10 June 1987, Beijing, China, p.792 (1987).

[58] Lorenzini E. C., Carroll J. A., "In-Orbit Experimentation with the Small Expendable-Tether Deployment System," Proceedings of the 41st Congress of the International Astronautical Federation, Dresden, Germany, 6-12 October 1990, Paper IAF-90-048, p.048 (1990).

[59] Lorenzini et al., Astrophys. Space Sci. (2006)

[60] Pain E., Bombardelli C., Cosmo M., Harwit M., Leisawitz D., Farley R., Rinehart S., Quinn D., and Miller D., "Far-infrared/submillimeter astronomical interferometry with spaceborne tether formations, Ap&SS, 302, 225-239, 2006.

[61] Beletsky V.V., Levin E.M.: "Dynamics of Space Tether Systems", Advances in the Astronautical Sciences, 83, Univelt (1993)

[62] Bombardelli, C., Lorenzini, E.C., Quadrelli, B.M.: Journal of the Astronautical Sciences 52(4), 475 (2004)

[63] Bombardelli, C., Lorenzini, E.C., Quadrelli, B.M.: Journal of Guidance Control and Dynamics 27(6), 1061 (2004)

[64] Cosmo M.L., Lorenzini E.C., Bombardelli C.: in Proceedings of 14th AAS/AIAA Space Flight Mechanics Conference, Maui, Hawaii, Paper AAS-04-171 (2004)

[65] DeCou A.B.: in Proceedings of the 3rd International Conference on Tethers in Space Toward Flight, San Francisco, CA (1989)

[66] Lorenzini E.C.: Journal of Guidance, Control, and Dynamics 10(3), 242 (1987)

[67] Lorenzini E.C. Carroll, J.A.: ESA Journal 15(1), 27–33 (1991)

[68] Lorenzini E.C., Bombardelli, C. Quadrelli, B.M.: in Proceedings of the 13th AAS/AIAA Space Flight Mechanics Meeting, PaperAAS03-222, Ponce, Puerto Rico (2001)

[69] Miller D.W., Hall S R.: Journal of Guidance, Control, and Dynamics, 14(2), 350 (1991)

[70] Pain, H.J.: The Physics of Vibrations and waves.Wiley, 3rd Edition, pp. 156–163 (1983)

[71] Quinn D.A., Folta, D.C.: in Proceedings of the 23rd Annual AAS Guidance and Control Conference. Breckenridge, CO (2000)

[72] Tomlin D.D., e al.: Space Tethers: Design Criteria,NASA TM-108573, (1997)

[73] Wilson J.M., Control of a Tethered Artificial Gravity Spacecraft, Ph.D. thesis, Stanford University, 1990.

[74] Nakaya K, et al., "On Formation Deployment for Spinning Tethered Formation Flying and Experimental Demonstration," 18th International Syposium on Space Flight Dynamics, 11-15 October 2004, Munich, Germany.

[75] Kokubun K, et al, "Deployment,Retrieval Control of Tethered Subsatellite Under Effect of Tether Elasticity," J. of Guidance, Control and Dynamics, Vol.19,No.1, January-February 1996.

[76] Fujii H.A., "Wave-Absorbing Control of Transverse Vibration of Tethered System," Journal of Astronautical Sciences, Vol 51, No.3, pp 249-259, 2004.

[77] Kim, M., and Hall, C.D., "Control of a Rotating Variable-Length Tethered System," J. of Guidance, Control and Dynamics, Vol.27, No.5, Sep-Oct 2004.

[78] Chung S.-J., Kong E. M, andMiller D. W., "Dynamics and Control of Tethered Formation Flight Spacecraft Using the SPHERES Testbed," 2005 AIAA Guidance, Navigation and Control Conference, San Francisco, August 2005.

[79] NASA web page, "International space station, facts and figures," http://www.nasa.gov/mission_pages/station/main/onthestation/facts_and_figures.html#.VNhsDBanZck .

[80] Tibert G., "Deployable Tensegrity Structures for Space Applications" PhD Thesis, Kungl Tekniska Hogskolan, Stockholm, Sweden (2002).

[81] ROCCOR web page, "Roll-able Trusses", http://www.roccor.com/products/roll-able-trusses /

[82] Community Plan for Far-IR/Sub-mm Space Astronomy, in proc. New Concepts for Far-Infrared and submillimeter Space Astronomy 2003, eds. D.J. Benford & D.T. Leisawitz (Washington, DC: NASA), NASA CP-2003-212233, pp. xv - xxv. Available from < http://astrophysics.gsfc.nasa.gov/reports_pubs/>.

[83] Harwit M., Leisawitz D., Rinehart et al. "A Kilometer-Baseline Far-Infrared/Submillimeter Interferometer in Space," SPECS Vision Mission Study Final Report, AIAA.

[84] Harwit M. et al., "Far-Infrared/Submillimeter Astronomy from Space Tracking an Evolving Universe and the Emergence of Life: A White Paper and Set of Recommendations for the Astronomy and Astrophysics Decadal Survey of 2010," http://www.ipac.caltech.edu/pdf/FIR-SMM_Crosscutting_Whitepaper.pdf , (2010)

[85] Astronomy and Astrophysics in the New Millennium 2001, National Research Council, (National Academy Press: Washington, DC).

[86] Abusafieh A., Federico D., Connell S. "Dimensional stability of CFRP composites for space-based reflectors," Proc. SPIE 4444, 9–16 2001.

[87] Arao Y., Koyanagi, J., Utsunomiya S., and Kawada H. "Effect of ply angle misalignment on out-of-plane deformation of symmetrical cross-ply CFRP laminates: Accuracy of the ply angle alignment," Compos. Struct. 93(4), 1225–1230 (2011).

[88] Baffes C., Mast T., Nelson J., Ponslet E., Stephens V., Stepp L., Williams E. "Primary Mirror Segmentation Studies for the Thirty Meter Telescope", Proc. SPIE, Vol. 7018, (2008)

[89] Baiocchi D., Stahl H.P., "Enabling Future Space Telescopes: Mirror Technology Review and Development Roadmap". Astro2010: The Astronomy and Astrophysics Decadal Survey, Technology Development Papers, no.23, (2009)

[90] Bath D., Spain D., Ness E., William S., Bougin M. "Evaluation of segmented and brazed mirror assemblies" Proceedings of the SPIE 5868:34–41 (2005)

[91] Bely P., "The Design and Construction of Large Optical Telescopes", Springer New York (2003)

[92] Catanzaro B. Thomas, J., Backovsky, S., Barber, D., Small, D., Johnston, R., Cohen, E. "Effects of aberrations (low order and quilting) on the performance of the all-composite design for the Herschel Space Observatory". Proc. SPIE 4444, Optomechanical Design and Engineering (2001),

[93] Catanzaro B., Connell S., Mimovich M, Backovsky S., Williams G., Thomas J., Barber D., Johnston R., Hylton J., Dodson K., Cohen E. , "Cryogenic (70-K) measurement of an all-composite 2-m-diameter mirror" Proc. SPIE 4444, Optomechanical Design and Engineering 2001, 238 (November 5, 2001)

[94] Carrión J. G, "Composite Materials for Future Launcher Applications: Testing to Meet Requirements from Cryogenic to Hot Temperatures", Proceedings of European Conference on Spacecraft Structures, Materials and Mechanical Testing, (2000)

[95] Cheng J., "The Principles of Astronomical Telescope Design". Springer New York. (2009)

[96] Delouard P., Krahenbuhl U., Peikert G. "Materials characterisation at cryogenic temperatures for the Planck telescope", Proceedings of the European Conference on Spacecraft Structures, Materials and Mechanical Testing 2005 (ESA SP-581). (2005)

[97] Gardner JP., "The Scientific Capabilities of the James Webb Space Telescope" Proc. of SPIE, 7010-19, (2008),

[98] Hochhalter J., Maji A., Reicher D., Process Induced Errors in Replicated CFRP Mirrors. ASCE Space 2004 Conference Proceedings: pp. 875-880 (2004)

[99] Jaworske D., Jeunnette T., Anzic J. "Measurements of Print-Through in Graphite Fiber Epoxy Composites", 34th International Sampe Symposium, May, 1989, pp. 780-789.

[100] Johnson J., Grobsky K., Bray DJ. "Rapid fabrication of lightweight silicon carbide mirrors" Optomechanical Design and Engineering 2002, Proceedings of SPIE Vol. 4771 (2002)

[101] Kalia S., Fu SY., "Polymers at Cryogenic Temperatures", Springer (2013)

[102] Kaneda H., Nakagawa T., Enya K., Tange Y., Imai T., Katayama H., Suganuma M., Naitoh M., Maruyama K., Onaka T., Kiriyama Y., Mori T., Takahashi A., "Optical testing activities for the SPICA telescope", Proceedings of the SPIE, Volume 7731, (2010)

[103] Kendrick S., "Monolithic versus segmented primary mirror concepts for space telescopes". Proc. of SPIE Vol. 7426 7426O-1 (2009) Koelle, D. E., Janovsky, R., – "Development and transportation costs of space launch systems", DGLR Fachausschuss S4.1, DGLR/CEAS European Air and Space Conference (2007)

[104] Kia H. "Modelling of Surface Deformation of Glass Fibre Reinforced Composites", Journal of Composite Materials, Vol. 20, July 1986, pp. 335-346.

[105] Kim K., Hale R. "Analysis of Surface Deformation Due to Thermal Load on Circular Quasi-Isotropic Laminate Mirrors" Proc 49th AIAA/ASME/ ASCE/AHS/ASC Structures, Structural Dynamics, and Materials Conf., Schaumburg, Illinois, AIAA Paper 2008-2185, 7-10 Apr. 2008.

[106] Martin H., Burgea H., Cuerden B., Miller S., Smith B., Zhao, C. "Manufacture of 8.4 m off-axis segments: a 1/5 scale demonstration" Optical Fabrication, Metrology, and Material Advancements for Telescopes, Proceedings of SPIE Vol. 5494 (SPIE, Bellingham, WA, 2004) .

[107] Martin R., Romeo R., Barber G., Braem A., Brook N., Cameron, B., D'Ambrosio C., Harnew N., Lessnoff K., Metlica F., Websdale D., "Lightweight CFRP spherical mirrors for the LHCb RICH-1 detector". Proc. SPIE 6670, Nonimaging Optics and Efficient Illumination Systems IV, 66700O (2007)

[108] Massarello J., DeBlonck B., Maji A. "Rapid Fabrication of Mirrors with Nanolaminate Facesheets and Composite Structures" SEM International Congress, Costa Mesa, CA, June 2004

[109] Massarello J., Welsh J., Hochhalter J., Maji A., Fuierer P., "Fibre print-through mitigation technique for composite mirror replication", Optical Engineering, v 45, n 12, December, 2006, p 123401

[110] Monnier J. D., "Optical interferometry in astronomy," Rep. Prog. Phys. 66, 789-857 (2003)

[111] Matson L., Chen M., DeBlonk B., & Palusinski, I. "Silicon Carbide Technologies for Lightweighted Aerospace Mirrors" . In Advanced Maui Optical and Space Surveillance Technologies Conference(2008).

[112] Onaka T., Sakon I., Fujiwara H., Shimonishi T, Lee HG., Ishihare D., Kaneda H., Okade Y, "Recent results from the infrared satellite AKARI" Interstellar Matter and Star Formation: A Multi-wavelength Perspective ASI Conference Series, (2010)

[113] Polis D., Sovinski M., Harris B., Puckett D. "Cryogenic Durability of a carbon fibre reinforced cyanate ester resin composite: Degree of cure" NASA Goddard Space Flight Centre (2006)

[114] Qu BB., Sutcliffe MPF. "Modelling generation of fibre waviness during processing" 14th European Conference on composite materials, Paper ID: 329-ECCM14 (2010)

[115] Romeo R., "Carbon fibre reinforced composite mirror and method of making the same" US Patent US20060092535 A1, (2006)

[116] Stahl HP.,"JWST Lightweight Mirror TRL-6 Results" In Aerospace Conference 2007 IEEE (2007)

[117] Thompson S., Bichon S., Grant R., "Influence of ply misalignment on form error in the manufacturing of CFRP mirrors" Optical Materials Express, Vol. 4, Issue 1, pp. 79-91 (2014) http://dx.doi.org/10.1364/OME.4.000079

[118] Utsunomiya S., Shimizu R., "Monitoring of Dimensional Stability of CFRP Mirrors for Space Telescopes by Using Embedded FBG Sensors", The 17th International Conference on Composite Materials, Scotland,(2009)

[119] Utsunomiya S., Kamiya T., Shimizu R. "Development of CFRP mirrors for space telescopes", Proc. SPIE 8837, Material Technologies and Applications to Optics, Structures, Components, and Sub-Systems, 88370P (2013)

[120] Thompson S., Brooks D., Doel P. "A nickel-carbon-fibre composite for large adaptive mirrors: Fabrication methods and properties", Opt. Express 16, 1321-1330 (2008).

[121] Van de Voorde, "Results of Physical Tests on Polymer Materials at Cryogenic Temperatures" IEEE Transactions on Nuclear Science (1973)

[122] Walker D.D., Yu, G., Li, H., Messelink, W.,Evans, R. , and Beauchamp, A., "Edges in CNC polishing: from mirror segments towards semiconductors, Paper 1: edges on processing the global surface", Opt. Express 20(18), 19787–19798 (2012).

[123] Dragovan M. "DART system for far-IR/submillimeter membrane telescopes", in: MacEwen, H.A. (Ed.), Highly Innovative Space Telescope Concepts. Proc. SPIE, vol. 4849. SPIE – The International Society for Optical Engineering, Bellingham, WA, pp. 1–7, 2003.

[124] David Leisawitz "NASA_s far-IR/submillimeter roadmap missions: SAFIR and SPECS" Advances in Space Research 34 (2004) 631–636